Physics of optically driven nanojunctions

Philippe Andreas RÖLLI

Acknowledgements

Je souhaite par ces quelques lignes remercier le grand nombre de personnes qui ont permis, d'une manière ou d'une autre, la réalisation de ce travail. Il m'apparaissait nécessaire que ces mots de gratitude soient exprimés de la manière la plus naturelle et la plus sensible possible, ce pour quoi le français s'est imposé à moi.

Dès lors, les premiers mots iront à ma famille qui m'a témoigné un soutien et une bienveillance sans faille et cela en dépit de la longueur et des incertitudes de mes recherches. Grands-parents, parents et frères, ce travail vous est bien-sûr dédié.

C'est ensuite envers mes amis de cercles divers et variés que mes pensées se tournent. Tous ces moments partagés sur les skis, dans les théâtres ou dans les salles de concerts ont été des bulles précieuses. Ils ont aussi été l'occasion d'improbables vulgarisations de mes recherches, de descriptions caustiques de la vie de laboratoire ou de réflexions diverses sur le rôle de la science. Merci d'avoir prêter l'oreille à ces récits et d'avoir peut-être, à l'occasion, feint un intérêt certain pour ces problématiques en somme très personnelles.

Mes recherches ont demandé la création de plateformes entièrement nouvelles, des échantillons jusqu'aux divers setups expérimentaux utilisés aujourd'hui. Cela n'aurait pas été possible sans l'important soutien de mon directeur de thèse. Au vu du caractère radicalement exploratoire de mon sujet, je me dois de témoigner une grande reconnaissance pour la confiance et la liberté qu'il m'a offert durant ces quelques années. À travers le travail sur cette thèse, j'ai aussi pu bénéficier des expertises de nombreux laboratoires, que ce soit sur le campus (LCMD, NAM, BIOS, FIMAP, LSEN, LNET) ou à travers des collaborations (MPI for Intelligent Systems, MPI for Light, King's college, Cambridge) qui ont permis les divers développements du projet.

Ces synergies et les développements de ces dernières années portent néanmoins la marque d'une personne en particulier, mon co-directeur de thèse. Je me réjouis de voir que son approche précise et claire de la science ainsi que son inlassable curiosité aient donné naissance à un nouveau laboratoire sur le campus. Il va s'en dire que ma thèse n'aurait pas été possible sans son mentorat et sans le travail assidu et méticuleux des collaborateurs de son groupe.

Ces quelques années sur le campus me font aussi mesurer à leur juste valeur différents services nous aidant au quotidien. Je pense en particulier au CIME, à la plateforme de croissance de cristaux, à l'atelier de l'Institut de Physique, mais aussi au support sans faille des collaborateurs administratifs de l'école doctorale, de la faculté et de notre laboratoire. Leur assistance a permis de répondre à de nombreuses questions épineuses tout au long de ma thèse.

Les derniers mots seront pour mes nombreux collègues, passés et présents, du LPQM. D'abord, pour les deux post-doctorants du team d'optomécanique qui, par leur travail dans les lab-

Acknowledgements

oratoires et leurs qualités humaines ont été une grande chance pour l'entier du groupe et ont incarné pour moi une belle et estimable idée de la science. Puis, pour tous ceux qui ont participé à l'élaboration du cours de physique générale, mes collègues du bureau PH D3 305 et ceux du laboratoire PH A avec qui j'ai partagé mes journées, des longues soirées et de nombreuses fins de semaine. Vos présences ont certainement rendu tout cela concevable. À tous, je souhaite le meilleur dans leurs recherches, leur vie professionnelle et privée.

Lausanne, September 4, 2020   P. R.

Abstract

Recent years have seen spectacular developments in the domain of nano-optics. Alongside the well-known techniques of super-resolution microscopy progress in nanofabrication has enabled important improvements in the fields of optical imaging and spectroscopy. Nowadays enhancements of specific near-field interactions by nano-antennae/cavities allows the optical readout of single molecule properties in a number of different systems. The observation of normal modes of vibration for example carries essential information on the orientation, link to the interface and environment in which the molecule is embedded.

This thesis develops firstly a novel theoretical frame for these vibration-cavity interactions by following the optomechanical formalism, which has proven to be an accurate treatment of a wide variety of mechanical systems interacting with a laser field. By leveraging this framework, we investigate on the one hand several quantum limits. On the other hand, for the parameter space experimentally available and for well-designed cavities, novel regimes of interaction between the collective mode of vibration of an ensemble of molecules and an optical tone seem within reach both in the visible and the infrared.

In parallel, this thesis experimentally explores one specific realization of such a system. In collaboration with the group of Christophe Galland we constructed the optical setups necessary to interrogate our nanostructures. The class of structures constructed, known as self-assembled nanojunctions or nanoparticles on mirror, reaches confinement of electric fields via plasmonic modes close to its fundamental limit and enables the study of many different mechanical systems whose thickness consist in a single molecule. Along this research we have developed techniques to characterize mechanical, electronic and thermal observables of nanojunctions interacting with an optical field.

Our experimental study has enabled the discovery of a novel effect related to the electronic confinement of these quasi-0-dimensional structures. The characteristic photoluminescence of metallic nanostructures is found to consistently blink in nanojunctions akin to other quantum emitters. The mechanisms explaining in detail this blinking remain debatable but the numerous experimental data collected highlight the key role of the interface in the specificities of the blinking observed. This finding opens novel ways to characterize the important and to date ill-described question of the interfaces in nanojunctions. The observed modifications of the nanojunctions optical properties might constitute an interesting step towards the development of a novel class of functional materials ('gap-materials') with enhanced and tailored electro-optical properties.

The last part of this thesis considers one technological application for this class of material

Abstract

---

by conceptually developing a new kind of detector based on the upconversion of an infrared photon to the visible; exploiting thus in a unique way the optical properties of the molecular system. The study of the quantum noises of these detectors highlights two exciting and technologically relevant directions for such devices : at room temperature these systems operate with levels of noise below state of the art devices, at lower temperatures these systems open an unexplored path towards single photon detection in a spectral range where this technology remains unavailable to date.

key words : optomechanics, plasmonics, sideband thermometry, Hermite-Gaussian excitation, nanojunction, photoluminescence blinking of metals, Mid-IR to NIR up-conversion, single photon detector

Résumé

Ces dernières années ont vu des développements spectaculaires dans le domaine de la nano-optique. Outre les techniques de super-résolution bien-connues, les progrès de nanofabrication ont permis l'amélioration des techniques de spectroscopie et d'imagerie du champ proche par l'utilisation de nano-antennes/cavités qui permettent de nos jours l'observation de propriétés d'une simple molécule. Un grand nombre d'informations sur ces systèmes sont accessibles via une lecture optique de leurs modes de vibrations.

Cette thèse s'articule premièrement autour de l'élaboration d'un cadre formel des interactions vibration-cavité en suivant le formalisme de l'optomécanique déjà valide pour décrire la physique d'un large nombre de systèmes mécaniques interagissant avec un faisceau laser. Tirant parti de ce formalisme, certaines limites inexplorées peuvent être mises en exergue. De plus, les paramètres accessibles expérimentalement à cette catégorie de système suggèrent la possible observation de nouveaux régimes d'interactions entre le mode collectif de vibration d'un ensemble de molécules et la cavité par pilotage optique aussi bien dans le visible que dans l'infrarouge moyen.

En parallèle, cette thèse explore les défis et opportunités apportés par de tels systèmes à la lumière de l'expérience. Pour cela, nous avons développé aussi bien les plateformes expérimentales que les échantillons avec la collaboration du groupe du professeur Galland. Le type de structure fabriquée, connu sous le nom de nano-jonction, confinent de manière inégalé les champs électriques issus d'une excitation optique via des modes collectifs d'oscillations d'électrons appelés plasmons et permettent ainsi l'interrogation de systèmes mécaniques dont l'épaisseur se limite à une unique molécule. Au travers de cette thèse nous avons développé les systèmes permettant l'identification, la caractérisation et l'étude des observables mécaniques, électroniques et thermiques de ces nanostructures lors d'une excitation optique. L'étude de ces systèmes nous a par ailleurs permis l'identification d'un nouvel effet intrinsequement lié au confinement de ces structures quasi-0-dimensionelles. La photoluminescence caractéristique des nano-structures métalliques se trouve ici fluctuer de manière similaire à des émetteurs quantiques. Les mécanismes gouvernant ce scintillement restent encore discutables mais les importantes données expérimentales collectées soulignent l'importance de l'interface et le rôle de l'illumination optique dans le type de scintillement observé. Cette découverte témoigne de la richesse de la physique impliquée dans ces systèmes et de la nécessité de développer de nouveaux outils rendant compte des propriétés de l'interface afin d'atteindre au niveau de contrôle souhaité de ces nanojonctions. À l'instar des explorations sur les matériaux 2D, les modifications des propriétés optiques des nanojonctions que

Résumé

nous observons ouvrent peut-être la voie à une nouvelle classe de matériau fonctionnel, les 'gap-materials'.

La dernière partie de cette thèse envisage une telle application technologique de ces matériaux en conceptualisant un nouveau type de détecteur basé sur la conversion ascendante d'un photon infrarouge vers le visible ; exploitant de manière unique les propriétés optiques de cette nouvelle classe de matériau. L'étude des bruits quantiques de ces détecteurs permet de mettre en avant deux régimes où ces structures ouvrent des possibilités nouvelles : à température ambiante ces systèmes fonctionnent avec des seuils de bruit inégalés, à basse température ces systèmes deviennent une alternative plausible à la détection directe de photon unique sur une plage spectrale où cette technologie n'a jusqu'alors pas été envisagé.

mot clés : optomécanique, plasmonique, thermométrie par bandes latérales, excitation Hermite-Gaussien, nano-jonction, scintillement de la photoluminescence de métaux, conversion ascendante du MIR vers le visible, détecteur à photon unique

Contents

Contents

1 Constitutive elements of the nano-junction

1.1 On molecular vibrations

The study of molecular vibrations has a long history and is commonly used in uncountable scientific areas. Their description at its fundamental level, usage in spectroscopy as well as the typical enhancement descriptions of their interaction with light can be found in numerous textbooks [1–3]. It should be noted than from the early days of quantum mechanics molecules and their vibrational modes have been a subject of conceptual developments [4–9]. Among other particularities these early investigations relied on the low occupancy at room temperature of the vibrational modes enabling investigations of several aspects like their anharmonicity [10, 11]. or measurements of the motional sideband asymmetry generated by the modulation of the incoming optical tone by the vibration.

We first describe elemental electronic properties of a molecule whose variations enable the understanding of both absorption and Raman scattering spectroscopy. Fig. 1.1 illustrates an example of such absorption and Raman spectra for a numerically simulated molecule. Then we address several aspects specific to the study of systems where a small number of molecules are interacting with a laser tone. Such systems have recently achieved outstanding experimental results such as the visualization of single molecules with optical illumination or more accurate understanding of the physics at the interface between the molecule and the substrate [12–14].

All these aspects will be exemplified around the biphenyl-4-thiol (BPT) molecule which is used in our laboratory. It might however be interesting to start with a few elementary numbers to remind the reader about several characteristics of these mechanical modes in order to enable a comparison with other mechanical systems and to motivate the discussions that follows. The 63 vibrational modes of a BPT molecule cover a spectral range of almost 100 THz starting at 0.5 THz (18-3200 cm^{-1}). The effective mass of these modes consists in a few atoms (1-9 amu) resulting in a zero-point motion between 4 and 40 picometers. Finally, as mentioned earlier, the high frequency of these modes results in low thermal occupation ranging from 0.09 to 75.4 average phonon(s) at room temperature. These first numbers and the following quantitative

(a)

(b)
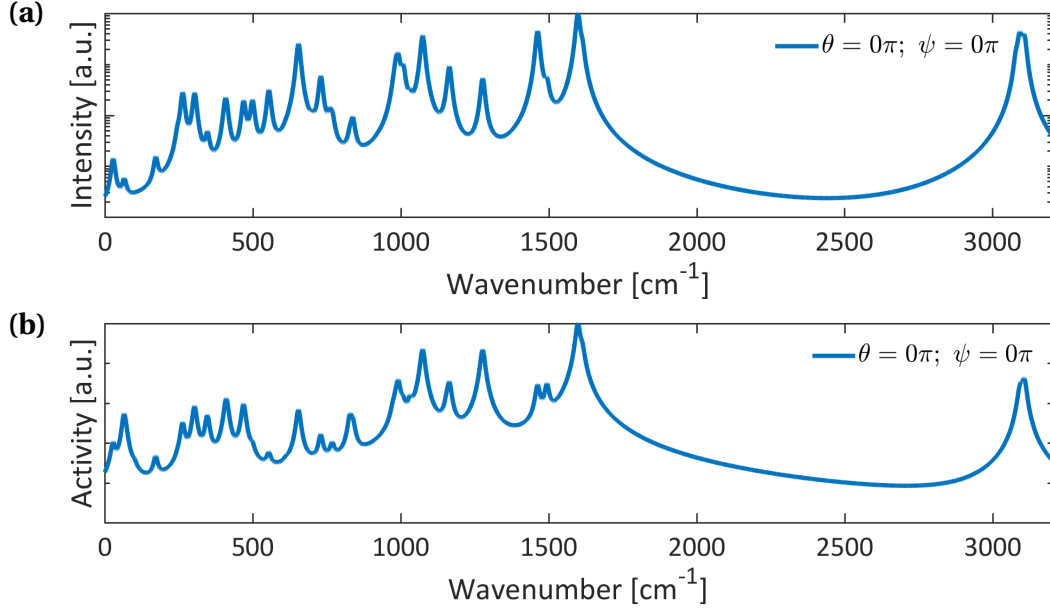
Figure 1.1 – Numerical calculation of the IR absorption **(a)** and Raman spectra **(b)** on a logarithmic scale for a BPT molecule linked to a gold atom. The modes profiles are represented by Lorentzians with a fixed ad hoc linewidth of 15 cm^{-1}. The configuration $\theta = 0$ and $\psi = 0$ accounts for a molecule with its main axis parallel to the EM field involved in the interaction.

investigations of the variations of the electronic properties of a molecule are obtained through density functional theory (DFT) calculations. A short user guide of its implementation through a dedicated software is available in the Appendix B. The DFT calculations and analysis have been performed with the help of Zsuzsanna Koczor-Benda (King's college, London).

1.1.1 Mode absorption via induced dipole variation

One first way to obtain information on some modes of vibrations of a molecular ensemble consists in calculating the absorption of an incoming light beam when crossing a medium containing the molecules of interest. In DFT calculations, the infrared absorption intensity related to a fundamental vibrational transition I_v^{IR} [1, 15] is obtained via the calculation of derivatives of electric moment components μ_v^i with respect to the normal coordinates representing the vibrational mode of interest Q_v. For historical reasons they are usually expressed in [km·mol^{-1}]. For a non-degenerate and harmonic vibrational mode the absorption intensity calculated by DFT software corresponds to absorption intensities averaged over all orientations and given by :

$$\langle I_v^{\text{IR}} \rangle = \frac{N_A}{12\varepsilon_0 c^2} \sum_{i=1}^{3} \left(\frac{\partial \mu_v^i}{\partial Q_v} \right)^2 ,$$

(1.1)

with N_A the Avogadro number.

More interestingly, the GAUSSIAN software gives access to the derivatives of the electric dipole with respect to the i-th component of the displacement in Cartesian coordinates of the n-th atom. These derivatives can then be converted to derivatives with respect to the normal coordinates of a vibrational mode v. All calculated quantities are expressed in atomic units, i.e. the electric moment is given in Bohr-electron (2.54 Debye / $8.48 \cdot 10^{-30}$ C·m) and the displacement in Bohr (0.529 Å). The quantities $\frac{\partial \vec{\mu}_v}{\partial Q_v}$ can easily be converted to other systems of units :

$$\left(\frac{\partial \vec{\mu}_v}{\partial Q_v} \right)^2 [\text{D}^2 \cdot \text{Å}^{-2} \cdot \text{amu}^{-1}] = \left[\frac{2.54}{0.53} \right]^2 \cdot \left(\frac{\partial \vec{\mu}_v}{\partial Q_v} \right)^2 [\text{atomic units}], \qquad (1.2)$$

and finally linked to the absorption intensity I_v^{IR} for an incoming field of arbitrary polarization $\vec{e}_{\text{i}}$

$$I_v^{\text{IR}}[\text{km} \cdot \text{mol}^{-1}] = 126.8 \cdot \left(\vec{e}_{\text{i}} \cdot \frac{\partial \vec{\mu}_v}{\partial Q_v} \right)^2 [\text{D}^2 \cdot \text{Å}^{-2} \cdot \text{amu}^{-1}]. \qquad (1.3)$$

Cross-section : This expression can be linked to the well-known absorption cross-section $I_v^{\text{IR}} = N_A \int \sigma_{v',\text{abs}} \, \mathrm{d}v'$. If we assume a Lorentzian profile for the vibrational mode considered (with $\omega_v/(2\pi)$ the vibrational mode resonance frequency and Γ_{tot} its damping rate), the on-resonance value of its cross-section is $\int \sigma_{v',\text{abs}} \, \mathrm{d}v' = \frac{\pi}{2} \sigma_{\text{abs}} \left(v' = v \right) \delta v = \frac{\pi}{2} \sigma_{\text{abs}} \left(v' = v \right) \frac{\Gamma_{\text{tot}}}{2\pi c}$.

Thus, the absorption cross-section can be inferred from DFT calculations:

$$\sigma_{v,\text{abs}} \, [\text{cm}^2] = \frac{4c}{N_A \Gamma_{\text{tot}}} I_v^{\text{IR}} \, [\text{km} \cdot \text{mol}^{-1}] \cdot 10^7. \qquad (1.4)$$

Effective dipole moment : Accordingly we can also describe an effective dipole moment d_v to characterize the vibrational transition and link it explicitly to the electronic moment derivatives found in DFT calculations [16]

$$d_v = \sqrt{\frac{3\hbar\varepsilon_0 c \Gamma_{\text{tot}} \sigma_{v,\text{abs}}}{2\omega_v}} = \sqrt{\frac{6\hbar\varepsilon_0 c^2 10^3}{N_A}} \sqrt{\frac{I_v^{\text{IR}}[\text{km} \cdot \text{mol}^{-1}]}{\omega_v}} \qquad (1.5)$$

In Chapter 5 we will illustrate how the coupling between an incoming IR electromagnetic field and a vibration can be formally introduced and calculated. We shall also illustrate its strength with a few examples.

1.1.2 Mode scattering via polarizability variation

Another complementary approach to investigate molecular vibrations consists in analyzing the optical spectra resulting from the inelastic scattering (Raman scattering) of light by the different vibrational modes. The quantity describing the strength of this process is derived from the vibrational modes Raman tensor and can be calculated from the derivatives of the polarizability tensor with respect to the normal coordinates of the vibrational mode $\frac{\partial \alpha_v}{\partial Q_v}$.

To simplify the following expressions we introduce the Raman tensor $R_\nu = \frac{\partial \alpha_\nu}{\partial Q_\nu}$ and we refer to the scalar $(\vec{e}_i \cdot R_\nu \cdot \vec{e}_j)$ as R_ν^{ij}. The total Raman scattered power arises from the contributions of the two possible outgoing polarizations. Averaging over random orientations of the molecules one can obtain [17]

$$\langle \left| R_\nu^{ii} \right|^2 \rangle = \sqrt{\frac{45\bar{\alpha}_\nu^{\,2} + 4\bar{\gamma}_\nu^{\,2}}{45}} \tag{1.6}$$

$$\langle \left| R_\nu^{ji} \right|^2 \rangle = \sqrt{\frac{3\bar{\gamma}_\nu^{\,2}}{45}}, \tag{1.7}$$

with

$$\bar{\alpha}_\nu^2 = \frac{1}{9} \left[R_\nu^{xx} + R_\nu^{yy} + R_\nu^{zz} \right]^2 \tag{1.8}$$

$$\bar{\gamma}_\nu^2 = \frac{1}{2} \left[\left(R_\nu^{xx} - R_\nu^{yy} \right)^2 + \left(R_\nu^{yy} - R_\nu^{zz} \right)^2 + \left(R_\nu^{zz} - R_\nu^{xx} \right)^2 \right] + 3 \left[\left(R_\nu^{xy} \right)^2 + \left(R_\nu^{xz} \right)^2 + \left(R_\nu^{yz} \right)^2 \right]. \tag{1.9}$$

These quantities do not depend on the two orthogonal orientations of the field chosen as polarisation basis but only on the intrinsic properties of the molecule. In that situation Raman scattering can be described by a scalar named the magnitude of the Raman tensor

$$\mathcal{R}^2 = \langle \left| R_\nu^{ii} \right|^2 \rangle + \langle \left| R_\nu^{ji} \right|^2 \rangle = \frac{45\bar{\alpha}_\nu^2 + 7\bar{\gamma}_\nu^2}{45} \tag{1.10}$$

The DFT software results are directly related to this averaged quantity. In fact, the values calculated correspond to $45\mathcal{R}^2$ and are expressed in atomic units $\left[\text{Å}^4 \text{amu}^{-1} \right]$ when we would prefer an expression in SI units ($[\epsilon_0^2 \text{m}^4 \text{kg}^{-1}]$). The correspondence between the two systems is given by

$$\mathcal{R}^2[\text{SI}] = (4\pi\epsilon_0)^2 \left[\frac{10^{-40}}{1.66 \cdot 10^{-27}} \right] \mathcal{R}^2[\text{g.u.}] \tag{1.11}$$

In order to obtain a first estimate of the interesting case of surface-enhanced Raman scattering (SERS) we also introduce the depolarization ratio $\rho = \langle \left| R_\nu^{ji} \right|^2 \rangle / \langle \left| R_\nu^{ii} \right|^2 \rangle$ that evaluates the importance of the cross-polarized component of the Raman-scattered field (with respect to the incoming field) and that is bounded by $0 \le \rho \le 3/4$. In the SERS scenario the outgoing field is solely polarized along the direction of the local cavity field $\vec{e}_L$. For randomly oriented molecules the magnitude of the Raman tensor is thus rescaled by a factor that depends on the depolarization ratio:

$$\langle \left| R_\nu^{LL} \right|^2 \rangle = \mathcal{R}^2 \frac{1}{1+\rho}, \tag{1.12}$$

that would take the value $\frac{4}{7}\mathcal{R}^2$ in the worst depolarization case.

Again it is possible to go beyond this averaged calculation by extracting from the DFT calculations the derivatives of the polarizability with respect to the i-th component of the displace-

ment in cartesian coordinates of the n-th atom. Reexpressing these quantities with respect to the normal modes of vibrations as explained in the Appendix B it is possible to evaluate the complete Raman tensor R_v for each normal mode and its projection along incoming and outgoing fields with arbitrary polarizations R_v^{ij}. Chapter 2 will show how the coupling between an optical localized electromagnetic mode and a vibration is linked to the calculation of this tensorial quantity.

Figure 1.2 – Numerical calculation of the IR intensities of a BPT molecule linked to a gold atom (BPT-S-Au) **(a)** and of a BPT molecule linked to a hydrogen atom (BPT-S-H) **(b)**. The inset in **(a)** depicts the BPT molecule and the two rotational angles considered. The modes profiles are represented by Lorentzians with a fixed ad hoc linewidth of 15 cm^{-1}. The configuration $\theta = 0$ and $\psi = 0$ accounts for a molecule with its main axis parallel to the IR field.

1.1.3   A note on the linkage of the molecule

In this thesis the experimental studies will be performed on samples built with a single layer of BPT molecules by self assembly. The choice of the substrate enabling the creation of the self-assembled monolayer (SAM), the concentration of molecules in the solution and the incubation time have to be taken with great care in order to reach the expected SAM layer. In our case, the BPT molecule is linked to gold by the removal of an hydrogen-sulfur bond and its replacement with an Au-sulfur bond. In Figures 1.2 (1.3), we show the normal modes IR intensity (Raman activity) of the initial molecule and their values when linked to a gold atom. In both cases, specific modes will in an experiment enable the identification of the molecular layer and will thus enable DFT simulations to describe with better accuracy the electronic properties of the experimental layer.
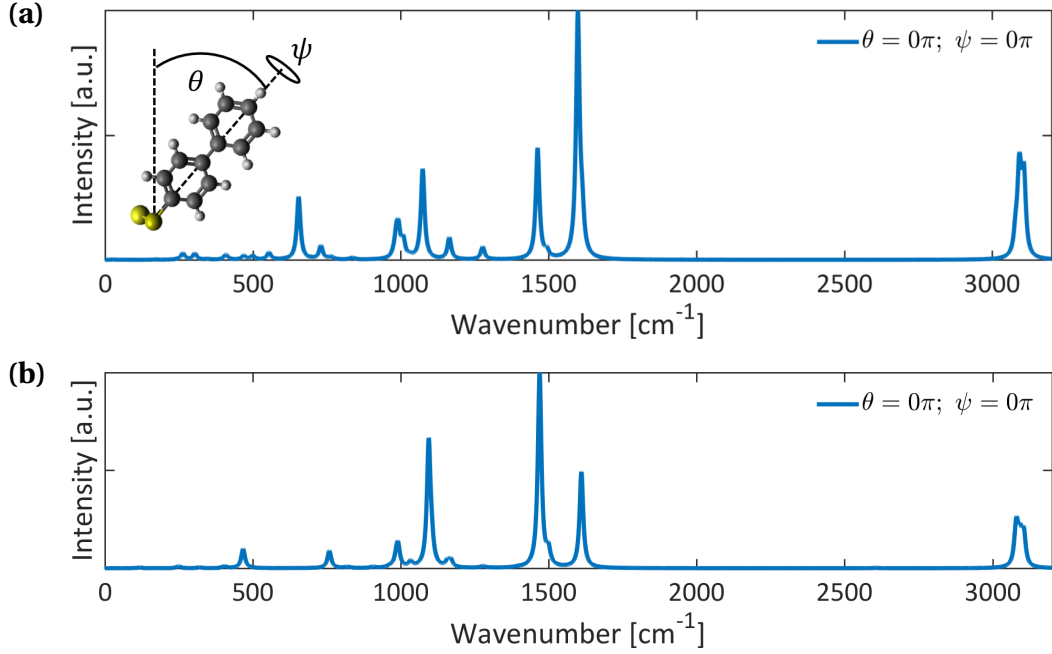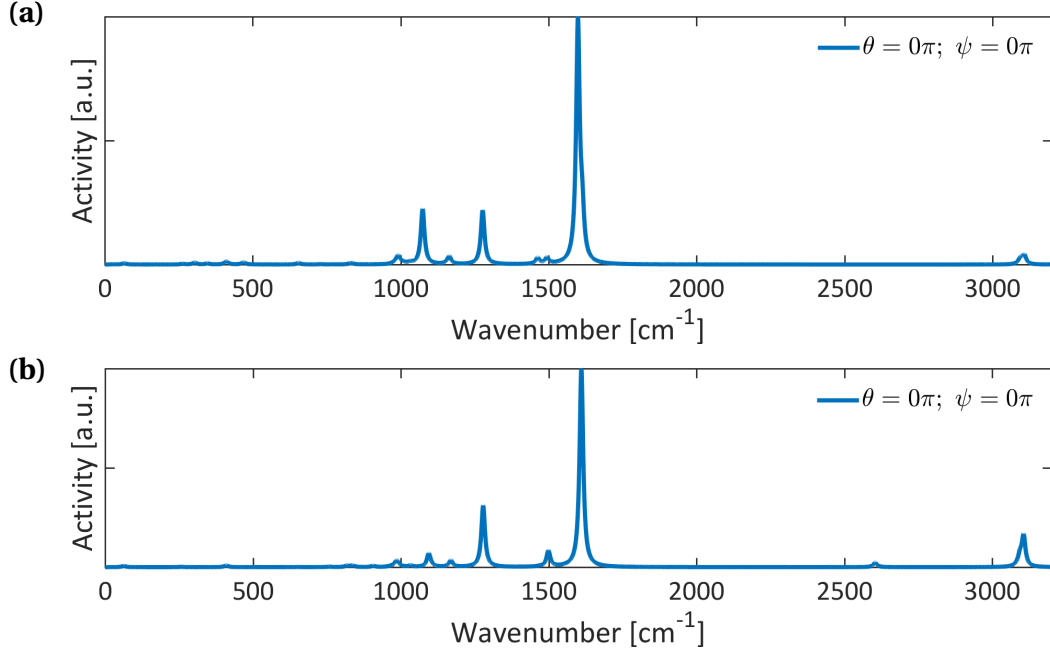
Figure 1.3 – Numerical calculation of the Raman activities of a BPT molecule linked to a gold atom (BPT-S-Au) **(a)** and of a BPT molecule linked to a hydrogen atom (BPT-S-H) **(b)**. The modes profiles are represented by Lorentzians with a fixed ad hoc linewidth of 15 cm^{-1}. The configuration $\theta = 0$ and $\psi = 0$ accounts for a molecule with its main axis parallel to the optical field involved in the interaction.

It is important to note that the electronic properties of one mode might significantly change when creating a self-assembled layer so that an accurate control of the linkage would be required to match accurately numerical simulation with experimental observations. Following previous studies [15, 18], we are currently investigating numerically and experimentally different molecular layers and different bonding types to improve the assembly of our structures and maybe identify the atomic link with optical measurements.

1.1.4   A note on the orientation of the molecule through optical measurements

Fig. 1.4 illustrates in two different spectral ranges another intriguing question explored in previous studies [19, 20]: the molecule orientation dependence of the resulting Raman activity (a similar dependence can be observed for IR measurements, Fig. 1.6). For these calculations we chose the coordinate frame so that the main axis of the BPT molecule is parallel to both the z-axis and the local field and so that θ describes a rotation of the molecule around the x-axis and ψ describes a rotation around the main axis of the molecule.

In addition to the usual Raman range explored experimentally, the high shift region represented in Fig. 1.4b and 1.5e offers an alternative range to evaluate the orientation of a molecule. The two numerical spectra represented here differ only by the ad-hoc linewidth used to rep-

(a)

(b)

Figure 1.4 – **(a-b)** Calculated Raman activities for two different ranges of vibrational frequencies and for a subset of possible molecule orientations. The modes profiles are represented by Lorentzians with a fixed ad hoc linewidth of 15 cm^{-1}. The configuration $\theta = 0.5\pi$, $\psi = 0\pi$ depicts a local electric field perpendicular to the main plane of the molecule.

(a) **(b)** **(e)**

(c) **(d)**
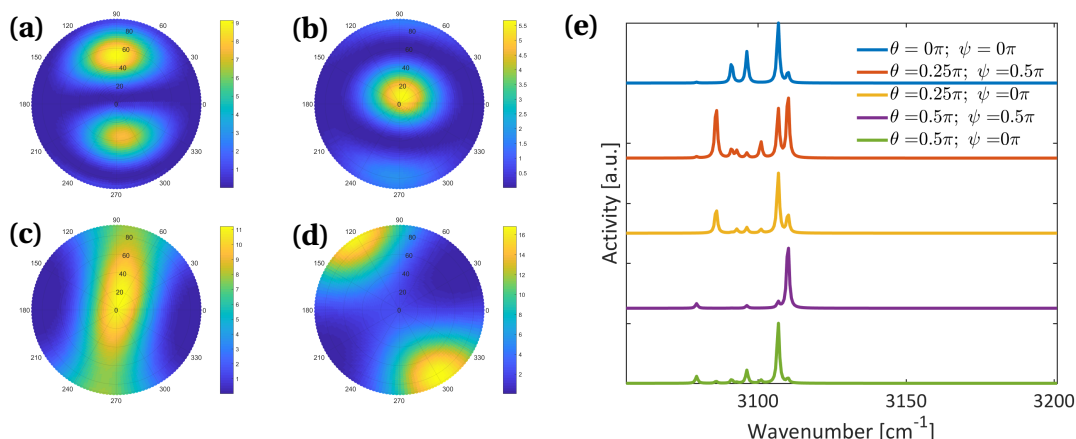
Figure 1.5 – **(a-d)** Polar representations of the Raman activity in the configuration space for the high wavenumber modes of BPT-S-Au (3086 cm^{-1} **(a)**, 3096 cm^{-1} **(b)**, 3107 cm^{-1} **(c)**, 3110 cm^{-1} **(d)**). **(e)** Calculated Raman activities in the same range as Fig 1.4(b) with fixed linewidths of 1 cm^{-1}. The configuration $\theta = 0.5\pi$, $\psi = 0\pi$ depicts a local electric field perpendicular to the main plane of the molecule.

resent the different modes. Its choice has to be adapted to the resolution limiting factor of a specific experiment (vibrational mode decay rate on a substrate, inhomogeneous Raman linewidth or optical setup resolution). The high frequency of these modes can for example be associated to tightly localized normal modes or involve different types of bonds. In the case of BPT, the higher frequency modes are involve C-H bonds while lower frequency modes are associated for example to C-C bonds. As can been seen in 1.5a-d, it translates into very distinct Raman activity patterns in the (θ, ψ) configuration space, that could be used efficiently to trace out the orientation of a molecule. In the case of an ensemble of molecules different possible

configurations can be weighted numerically in order to simulate the expected spectrum.
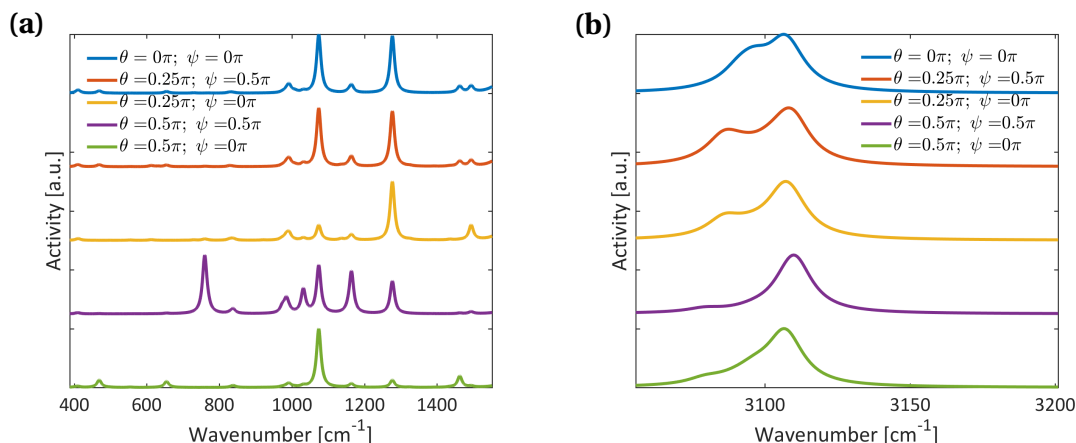
(a)

(b)
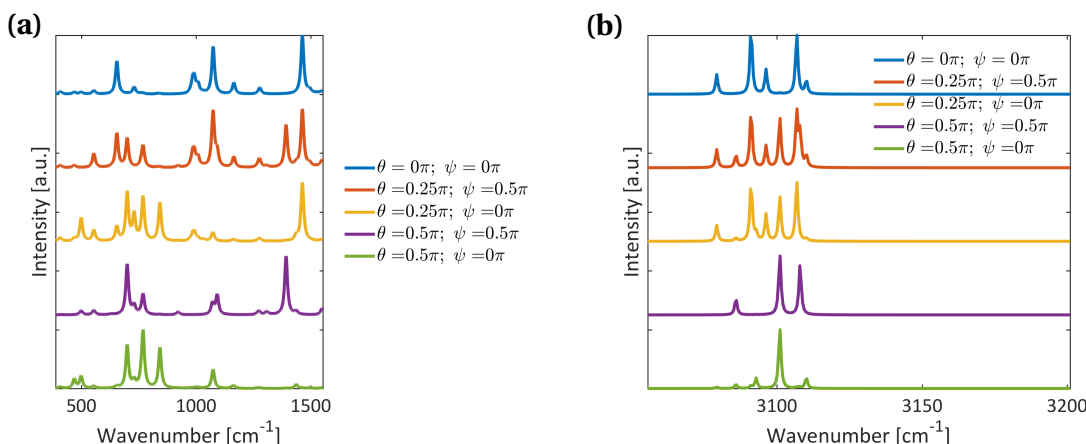
Figure 1.6 – **(a-b)** Calculated IR intensities for two different ranges of vibrational frequencies and for a subset of possible molecule orientations. The modes profiles are represented by Lorentzians with a fixed ad hoc linewidth of 15 cm^{-1}. The configuration $\theta = 0.5\pi$, $\psi = 0\pi$ depicts a local electric field perpendicular to the main plane of the molecule.

Both the linkage and orientation questions are not only exciting in terms of improved visualization of molecular layers with optical measurements but also in an engineering point of view in order to control and tailor the electronic properties of these single-molecule layers. It should finally be noted that the experimental data would need to be processed in order to recover the native Raman activity of the molecules[21] and correct for the frequency dependent part of the enhancement provided by typical plasmonic antennae.

1.2 On plasmonics

One could think that the sub-wavelength cavities are exactly described in the same way as textbooks optical cavities. However the level of losses of these cavities are motivating a different treatment than the one followed usually for high-Q cavities. It is thus interesting to remind a few basic aspects of plasmonics and explain which concepts departs from the common concepts introduced in the realm of high-Q cavities. Finally I will introduce two specific sub-wavelength structures of interest for what follows.

1.2.1 Sub-wavelength confinement of EM field

A simple model - The Drude model

We first describe the relation between the conduction electrons and the electromagnetic field through the Drude model. Our purpose here is to remind how the local permittivity function is found from a classical approximation of the interaction between the molecular orbitals and the electric field and then illustrate how the value of the permittivity found in metals leads to

the appearance of resonant behaviours which will be referred to as a plasmonic mode.

We describe the displacement of the electrons as a classical damped oscillator, the electric field being only a small external perturbation [3, 16]:

$$m\left(\frac{\mathrm{d}^2\vec{r}}{\mathrm{d}t^2} + \omega_0^2\vec{r} + \kappa\frac{\mathrm{d}\vec{r}}{\mathrm{d}t}\right) = -e\vec{E} \tag{1.13}$$

with ω_0 the energy between two electronic levels, κ the damping due to non-described interactions. So that the solution can be written as:

$$\vec{r}_0 = \frac{-e/m}{\omega_0^2 - \omega - i\kappa\omega}\vec{E}_0 \tag{1.14}$$

Next, we introduce again the definition of the dipole moment and compare it to the induced electric dipole in order to identify the expression for the polarizability:

$$\alpha(\omega) = \frac{e^2/m}{\omega_0^2 - \omega^2 - i\kappa\omega} \tag{1.15}$$

Both the permittivity of a dilute solution and the one of a metal can be described with this approach. In the first case, considering that the solute optical properties are dominated by a single electronic transition, we can link the expression of the macroscopic polarizability: $\vec{P} = n\alpha(\omega)\vec{E}$ (n being the number of molecules per unit volume) with the equivalent one using this time the definition of the permittivity: $\vec{P} = \epsilon_0(\epsilon(\omega) - 1)\vec{E}$. We find the relation:

$$\epsilon(\omega) = 1 + \frac{n\alpha(\omega)}{\epsilon_0} \tag{1.16}$$

For metals, we are allowed to reduce the expression of the polarizability by assuming that the electrons are not constraint by a restoring force into a harmonic motion, i.e. $\omega_0 = 0$ (free-electrons contribution). Adding to this term corrections for inter-band transitions (encompassed in ϵ_b) we find :

$$\epsilon(\omega) = \epsilon_b\left(1 - \frac{\omega_p^2}{\omega^2 + i\kappa\omega}\right) \quad \text{with } \omega_p = \sqrt{\frac{ne^2}{m\epsilon_0\epsilon_b}} \tag{1.17}$$

ω_p being the intrinsic oscillation frequency of the material electronic plasma. The permittivity of the material can be divided in its real and imaginary parts :

$$\begin{aligned}
\mathrm{Re}(\epsilon) &= \epsilon_b\left(1 - \frac{\omega_p^2}{\omega^2 + \kappa^2}\right) \\
\mathrm{Im}(\epsilon) &= \frac{\epsilon_b\omega_p^2\kappa}{\omega(\omega^2 + \kappa^2)}
\end{aligned} \tag{1.18}$$

In the simplest case of a metallic spherical nanoparticle of diameter d interacting in air with

an incoming electromagnetic field at wavelength λ the total internal electric field can easily be calculated analytically in the electrostatic approximation ($d \ll \lambda$) to obtain the expression [16]:

$$E_{\text{in}} = \frac{3}{\epsilon(\omega) + 2} E_0 \tag{1.19}$$

with E_0 the incoming electric field. We observe that when $\epsilon(\omega) \simeq -2$ the field inside the metal is only limited by the imaginary part of the material permittivity. This condition can be met in metals at optical frequencies. This resonant process constitutes the simplest example of a plasmonic resonance where part of the incoming electromagnetic wave energy is stored inside the metal in the form of a collective motion of electrons whose spatial extent is limited along one direction by the penetration depth inside the material and, for sufficiently small structures by theirs lateral dimensions.

It has to be noted that in this limit of small structures ($d \ll \lambda$) the resonance frequency is independent of the geometry of the nanoparticle and is dominated by the material permittivity alone. For larger systems the complexity of the problem increases and one uses numerical methods to evaluate with precision the different modes and their dependence on geometrical factors.

Energy in metallic system

The general expression for the electrostatic energy density for a lossy material is given by [22] :

$$u_E = \frac{1}{2}\epsilon_0 \frac{\mathrm{d}(\omega\epsilon(\omega))}{\mathrm{d}\omega} |E|^2 \tag{1.20}$$

The familiar expression of the energy density of a dielectric $u_E = \frac{1}{2}\epsilon_0\epsilon|E|^2$ is found again for a material with frequency independent permittivity, i.e. a material with negligible dispersion. In the case of metals (where absorption has also to be taken into account) the expression can be extended [23] to highlight the part of the energy density located inside the metal u_m :

$$u_m = \frac{1}{2}\epsilon_0 \left(\text{Re}(\epsilon) + \frac{2\omega\text{Im}(\epsilon)}{\kappa} \right) |E|^2 \tag{1.21}$$

It should be noted that the energy is not parted equally between the field inside and outside the metal [24] so that the knowledge of the field outside the nanostructure is in general not sufficient to evaluate some characteristics of the structure.

1.2.2 Cavity framework for a sub-wavelength metallic system

The simple model introduced in the previous section already presented the important role played by the imaginary part of the permittivity. This quantity describes the absorption of the material and is linked to the decay rate of a plasmonic mode on resonance. Fig. 1.7 illustrates

the frequency dependence of the plasmonic losses. These losses are here separated into radiative and intrinsic channels. It is important to notice that in the near-infrared range structures fabricated with gold show radiative losses comparable if not bigger than intrinsic losses close to the plasmonic mode resonance.
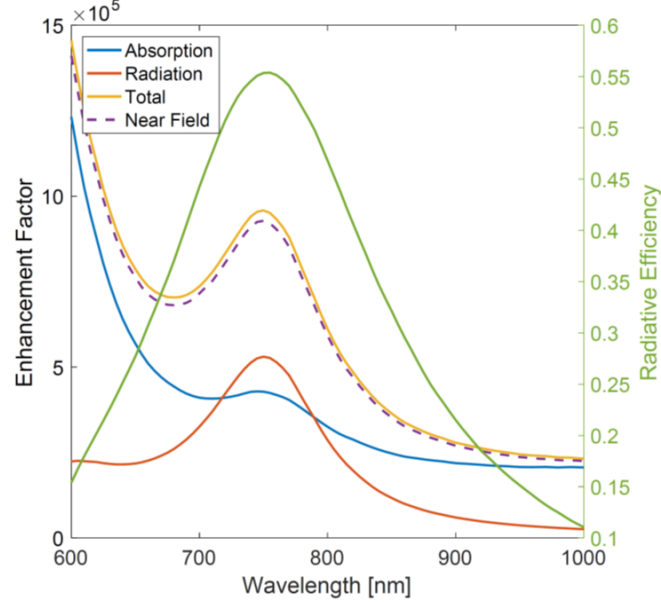
Figure 1.7 – Numerical calculations of optical parameters of a gap structure (formed by a gold film, a gap material and a perfectly spherical nanoparticle). A Drude-Lorentz model describes the electromagnetic response of gold fitted from experimental data [25] and the gap material is described by a dielectric with refractive index $n = 2.1$. Right axis : enhancement of the emission of a point-dipole located in the middle of the gap material (Purcell factor) from the calculation of the power emitted outside of two numerical shells enclosing the nanostructure and located in the near- (dashed purple line) and far-field (yellow line). Left axis : ratio of the power radiated in the far-field to the power dissipated in the metallic structure (green line). The absorption (blue line) and radiative losses (red line) are depicted in arbitrary units. The wavelength scan is obtained by a modification of the dipole oscillation frequency.

The importance of both of these decay channels in comparison with the familiar losses of high-Q optical cavities is intrinsic to the sub-wavelength nature of the cavity [26] as a substantial part of the energy inside such cavities is contained in the form of kinetic energy of electrons. One immediately sees that the oscillations of the electrons leads both to higher radiated and absorbed powers. For a given material, the intrinsic ratio between the stored energy and the energy loss per cycle is given by the quality factor and can be calculated at its resonance frequency $\omega/(2\pi)$ through the generalized expression for leaky materials [24]:

$$Q = \frac{\omega}{2\text{Im}(\epsilon)} \frac{\text{dRe}(\epsilon)}{\text{d}\omega} \tag{1.22}$$

11

It should be noted that the specific mode quality factor would not necessarily be limited to the intrinsic quality factor of the material considered to build the cavity but would depend on the specific distribution of the field inside the cavity.

This class of lossy resonators motivated thus the extension of the formalism used to describe the normal modes of high-Q cavities to cavities made of dissipative and dispersive materials.

QNM formalism

Many different groups specialized in the techniques required to handle the decomposition of the optical response of nanostructures through a quasi-normal mode formalism and the different basic concepts I present here are described in extenso in Ref.[27]. In this formalism one leaky mode is described by complex frequency $\tilde{\omega}_m = \Omega_m - i\Gamma_m/2$ where the imaginary part Γ_m represents the leakage rate of the mode. It should however be noted that the existence of steady state field distributions inside such leaky resonators requires an amplification mechanism. It can be shown that the imaginary part of the mode plays that role and compensate for the leakage inside the cavity. Outside the cavity this amplification results in an exponential divergence of the field which yields the normalization difficulties encountered with quasi-normal modes and the requirement to modify the definitions and calculations of related quantities (quality factor, Purcell factor, mode volume).

In this formalism the quality factor can be generalized to quasi-normal modes without additional assumptions on the energy balance encountered in such resonators :

$$Q_m = -\frac{\mathrm{Re}\,(\tilde{\omega}_m)}{2\mathrm{Re}\,(\tilde{\omega}_m)} \tag{1.23}$$

Mode volume

The definition of a proper mode volume for dispersive and dissipative cavities is a challenging computational task as the techniques used for high-Q cavities will in general fail. Formally by decomposing the response in quasi-normal modes one sees that the mode volume becomes a complex quantity defined by [27]:

$$\tilde{V}_m = \frac{1}{2\epsilon_0 \, n^2 \left(\tilde{\mathbf{E}}_m\,(\mathbf{r}_0) \cdot \mathbf{u}\right)^2} \tag{1.24}$$

with $\tilde{\mathbf{E}}_m$ the normalized complex electric field of the QNM and $\mathbf{u}$ the dipole direction. In this expression the mode volume is defined with the electric field intensity at the emitter position. Only the real part of the mode volume enters the Purcell factor expression. The role of the imaginary part can be appreciated from the ratio $\mathrm{Im}\,(V_m)\,/\mathrm{Re}\,(V_m) = -\tan\left(2\arg\left[\tilde{\mathbf{E}}_m\,(\mathbf{r}_0) \cdot \mathbf{u}\right]\right)$ which reveals that the phase of the QNM mode impacts the calculation of these quantities.

In order to evaluate the mode volumes of several relevant systems, we use the numerical tool

Comsol [1] based on finite element method to simulate optical properties of the nanostructure and collaborated on advanced designs with several collaborators (Huatian Hu in Wuhan University and Diego Martin-Cano in MPI Erlangen). Simulations use the electromagnetic waves module to perform frequency domain study of the fields. The metal nanoparticles are defined by their relative permittivity using the Drude model description while the outermost layer consists in a perfectly matched layer (PML). Then we use the method presented in Ref. [28] where a classical dipole oscillating at a frequency ω_d is inserted at a specific position of the cavity so that cavity-enhanced emission of the dipolar source can be compared to its free space value to extract the Purcell factor and relate it to the real part of the mode volume [27, 29] :

$$P = \frac{2\pi c^3}{\omega_d^3} \frac{Q}{\mathrm{Re}(V)} \tag{1.25}$$

This method is valid only for modes spatially or spectrally far apart with spectral profiles well-represented by Lorentzian distributions. In the more complex cases, the decomposition in QNM modes of the nanostructure response and the calculation of their individual characteristic would be required. Several works implemented such approaches to revisit cavity physics in sub-wavelength and dispersive optical systems [30–33].

1.2.3   Example I : Nanoparticle on mirror (NPOM)

The nanoparticle on mirror assembly has been the subject of a large variety of studies highlighting the very tight level of confinement of the electric field in such structures and their interest in enhancing light-matter interactions [34].

We summarize hear a few properties of such structures with the help of a simple analytical model enabling to identify the mode of interest in experimental works.

Mode families of a faceted NPOM

It is enlightening to consider the model suggested in Ref. [36] to introduce the different plasmonic modes appearing in NPOM structures. When brought close to the mirror layer the nanoparticle collective charge oscillations couple to their mirror image creating a family of longitudinal plasmonic modes labelled L_{mn} with m the azimuthal number describing the cylindrical symmetry and n the radial symmetry of the mode. In addition, as evidenced in Fig. 1.8, the nanoparticles are faceted and their morphology close to the gap is similar to a metal-insulator-metal (MIM) multilayer [36, 37]. The behaviour of these modes ressemble the one of Fabry-Pérot cavity modes. As the edges of the MIM act as partial reflectors for the field located inside the MIM, standing waves appear at discrete wavelengths creating a second family of modes inside the gap. These transversal modes are labelled S_{mn} and do not depend on the nanoparticle height while the modes sustained by the nanoparticle itself are height dependent. The distribution of the electric fields inside the gap for the three modes of interest

---

[1]http://www.comsol.com/
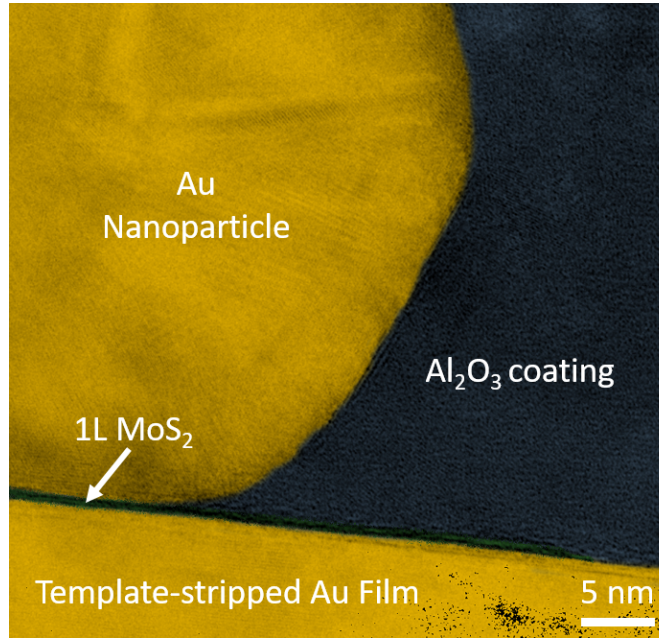
Figure 1.8 – False colors TEM image of a representative nanoparticle on mirror (NPOM) structure. The separation between the faceted gold nanoparticle and the template-stripped gold film is constituted by a single MoS_2 layer. This gap supports several modes that can be activated by optical illumination. Original picture from [35] modified with the courtesy of W. Chen.

in our experiments are illustrated in Fig. 1.9.
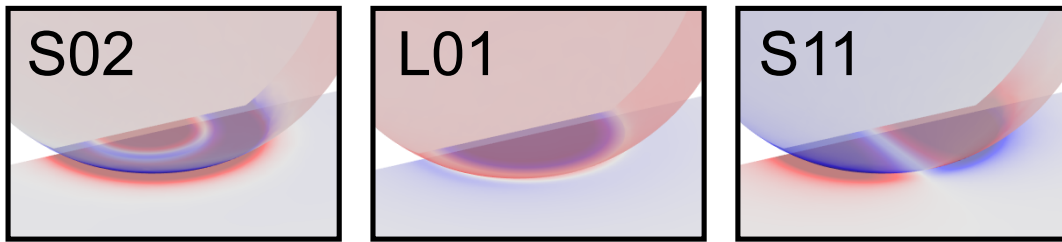
Figure 1.9 – Electric field distribution for the three main modes of a faceted nanoparticle on mirror. The structure has been simulated by our collaborator H. Hu in Wuhan University.

It is important to note that the difference in the fields spatial distributions results in different radiation patterns and incoupling ratios. Fig. 1.10 illustrates for example the radiation pattern of the L01 mode and the related collection efficiency depending on the objective used. Interestingly the modes L01 and S02 share the same axial symmetry so that these modes couple when spectrally overlapping. Depending on the specific parameters of the nanostructure the phase relationship between the two individual modes might be modified and impact the resulting hybridization of the modes.
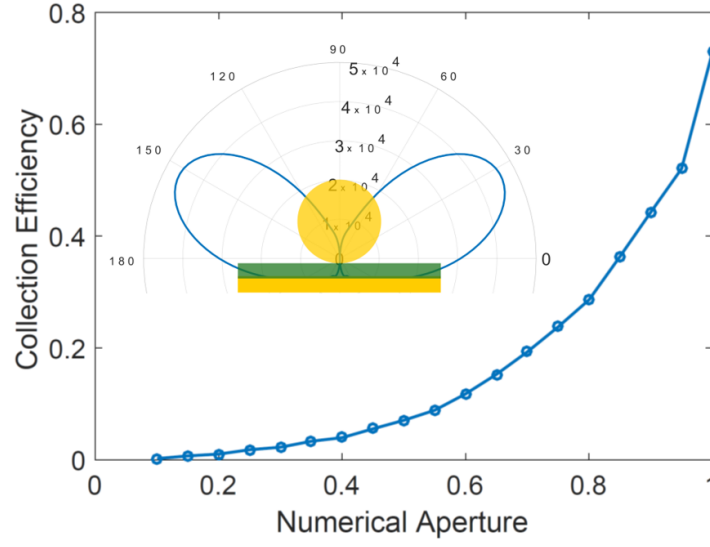
Figure 1.10 – Numerical calculation of the collection efficiency of a signal emitted by a local emitter located in the middle of a self-assembled nanojunction constituted with a perfect nanosphere by an ideal lens as a function of its numerical aperture. The inset illustrates the calculated radiation pattern of the antenna mode (L01) of a typical nanoparticle on mirror.

1.2.4 Example II : Dual plasmonic antenna
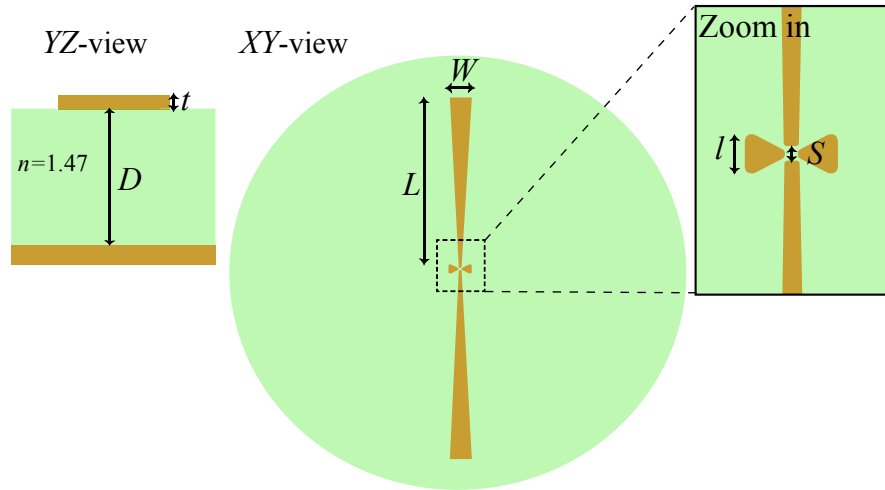
Figure 1.11 – Geometry of the dual antenna. The following parameters $W = 70$ nm, $L = 2.25\,\mu$m, $l = 90$ nm, $S = 25$ nm, are used to run the numerical simulations and evaluate the performance of our conversion scheme. The antenna edges were rounded with 4 and 1.3 nm radii of curvature for the optical and IR antenna, respectively. The dual antenna has been simulated by our collaborator D. Martin-Cano in MPI Erlangen

Our dual antenna consists of two gold bowtie structures. We set the gap between the tips

of both antennae (S = 25 nm) so that the current design could be developed using current nanofabrication techniques such as focused ion beam milling or advanced e-beam lithography. We select the other structural parameters (Fig. 1.11) in order to obtain appropriate resonances both in the mid-IR (length L and width W) and in the optical domain (short length l). In our design the 24 nm high nanostructure lays on top of a gold substrate. They are separated by an inactive dielectric layer (n = 1.47) of 8 μm. This substrate reflects the incoming field and creates an interference pattern that improves the absorption of the IR incoming field as shown in a previous study [38].

We use a 3D FEM software (COMSOL MULTIPHYSICS) to evaluate our dual antenna design. A Drude-Lorentz model describes the electromagnetic response of gold fitted from experimental data [39]). For the calculation in the optical range a dielectric layer (ITO) with refractive index n = 1.94 and thickness 52 nm was added below the antenna [40].
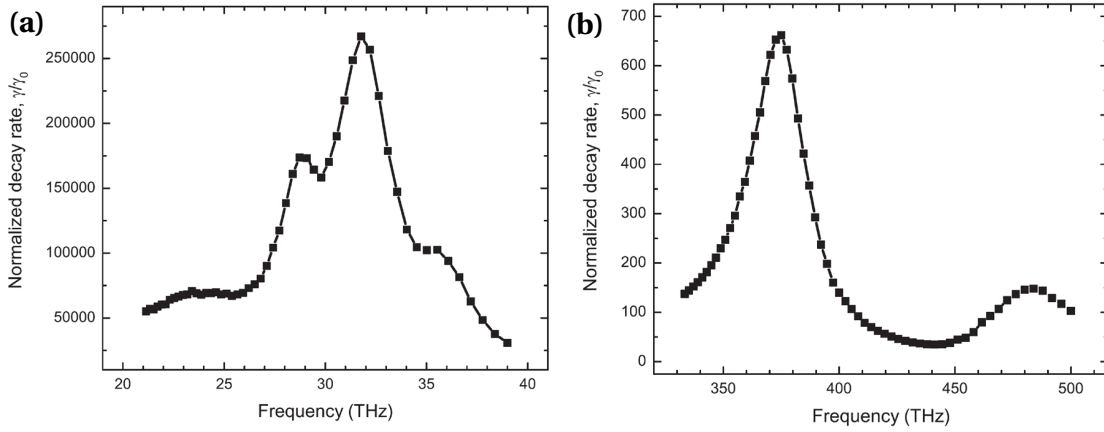
Figure 1.12 – Normalized decay rate of an emitter placed at the center of the dual antenna in the mid-IR **(a)** and in the visible range **(b)**.

A dipolar emitter is placed in the center of our structure to evaluate the local density of electromagnetic states inside the antenna. Figure 1.12 shows the modification of the radiated power as a function of the oscillation frequency of the dipole. Based on these plots, we modelled the response of the structure to an incoming optical field at 374 THz and to an incoming mid-IR field at 32 THz as being dominated by the contribution from a single resonance with Lorentzian profile. We thus used a multi-Lorentzian fit to extract the relevant linewidths and total decay rates (see Fig 1.13). Through the Purcell formula [41], we could estimate the corresponding effective mode volumes. Additional integrals were computed to determine the losses originating from absorption in the metal and determine the ratio between intrinsic and radiative losses at the resonance frequencies. All parameters are shown in Table 1.1.
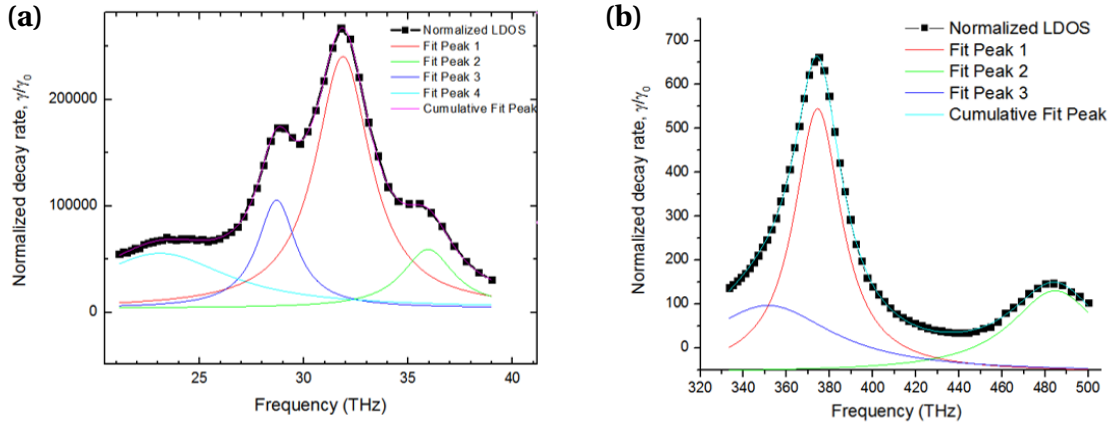
Figure 1.13 – Normal modes decomposition of the dual-antenna response in the mid-IR **(a)** and in the visible range **(b)**.

Parameter	mid-IR	VIS/NIR
$\kappa/2\pi$ [THz]	3.2	26.7
η	0.52	0.73
V [m^{-3}]	$2.6 \cdot 10^{-21}$	$1.0 \cdot 10^{-21}$

Table 1.1 – Antenna parameters as obtained from our FEM simulations
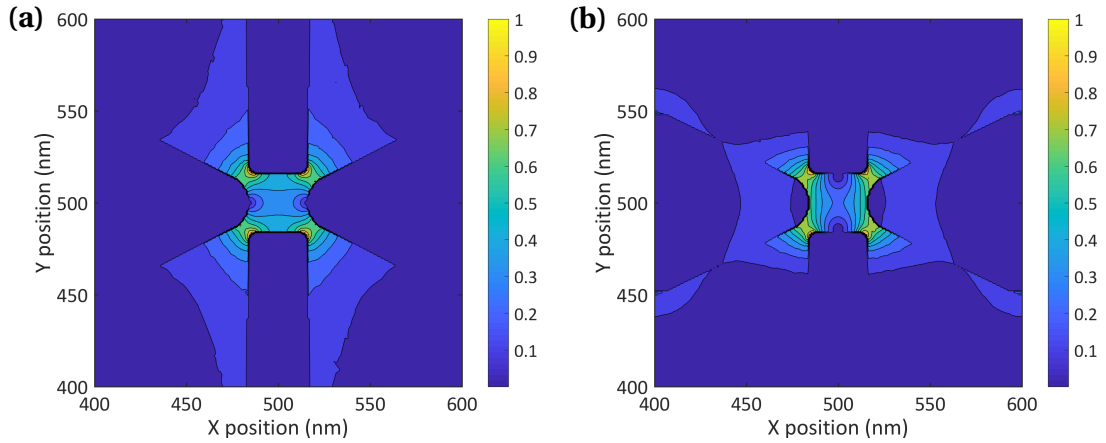
Figure 1.14 – Normalized distribution of the norm of the local electric field at the IR **(a)** and optical **(b)** resonances of the dual-antenna.

Spatial overlap - η_{mode}

It is remarkable to note how this architecture enable the combined sub-wavelength confinement of two electromagnetic fields whose wavelengths are separated by more than one order

17

of magnitude in free space (see Fig. 1.14). There are however several factors that prevent a perfect overlap of the distributions of the two vectorial fields. First, from the mode volume calculation it can be seen that the spatial extend of the two modes differ. Part of this scalar mismatch can be attributed to the portion of the fields outside of the central region for both fields and inside the metal for the optical field (cf. Fig. 1.14).

A detailed calculation requires however to take into account the polarization of both fields inside the antenna. From the fields orientations inside the gap region of the structure (Fig. 1.15a-b) it can be seen that the incoming optical and IR fields should be polarized along the main axis of their corresponding part of the antenna to achieve highest incoupling efficiency. This condition can be simply implemented with standard optics elements. Despite this cross-polarized configuration of the incoming beams both fields are mixing inside the dual-antenna structure so that both fields are collinear in the regions where the fields are greatly confined (cf. Fig 1.15c).
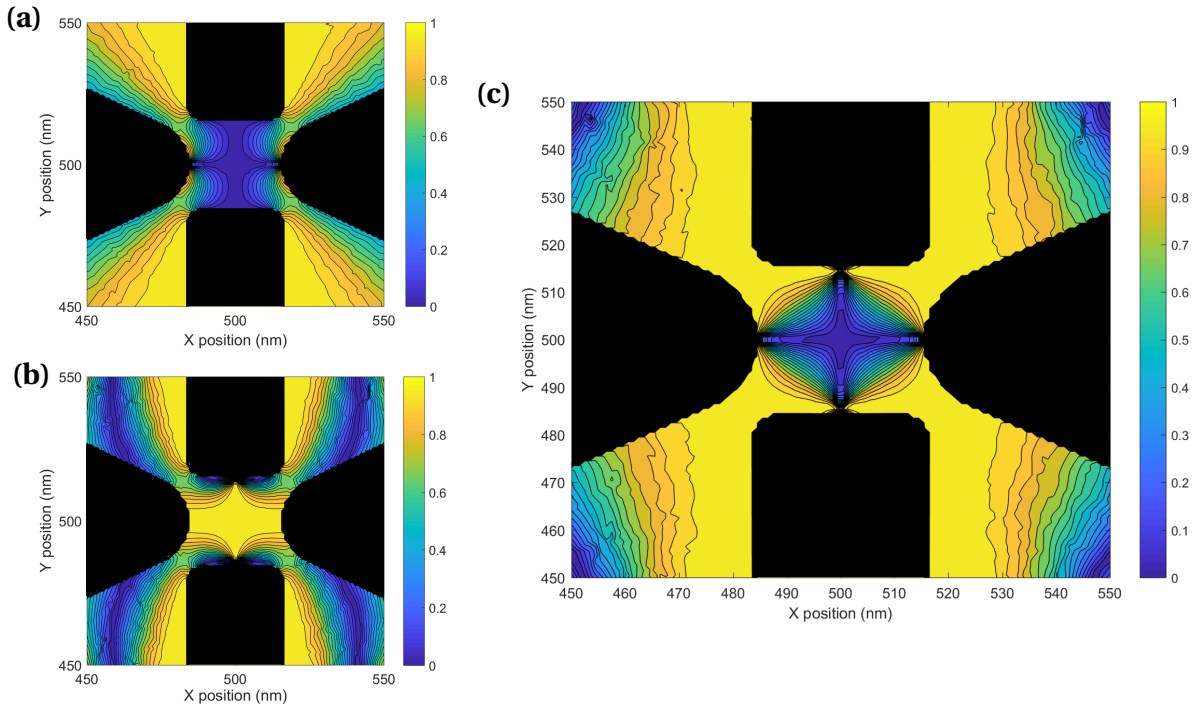
Figure 1.15 – Fraction of the electric field along the x axis in the IR range **(a)** and in the optical range **(b)**. **(c)** Local overlap between the polarizations of the IR and optical fields inside the antenna $\left(\left| \vec{E}_{\mathrm{opt}} \cdot \vec{E}_{\mathrm{IR}} \right| / \left\| \vec{E}_{\mathrm{opt}} \right\| \left\| \vec{E}_{\mathrm{IR}} \right\| \right)$. The metallic regions are excluded from the calculation and are depicted in black.

The spatial overlap between the two electromagnetic modes is thus computed numerically from the vectorial field distributions of both modes outside the metallic parts and according

to :

$$\frac{\left(\int \left|\mathrm{Re}\left(\vec{E}_{\mathrm{IR}}\right)\cdot\mathrm{Re}\left(\vec{E}_{\mathrm{opt}}\right)\right|\mathrm{d}A\right)^2}{\left(\int \left|\mathrm{Re}\left(\vec{E}_{\mathrm{IR}}\right)\cdot\mathrm{Re}\left(\vec{E}_{\mathrm{IR}}\right)\right|\mathrm{d}A\right)\left(\int \left|\mathrm{Re}\left(\vec{E}_{\mathrm{opt}}\right)\cdot\mathrm{Re}\left(\vec{E}_{\mathrm{opt}}\right)\right|\mathrm{d}A\right)} \tag{1.26}$$

Over the full structure we calculate an intensity overlap of 0.58 while the vectorial calculation described by the previous formula results in a mode overlap of 0.44 between the two electromagnetic fields inside such an antenna. Beyond possible simplifications in the numerical treatment of this nanostructure, the quality of the overlap allows to envision schemes where both fields could interact via an additional layer that would act as a mixer.

2 An optomechanical description of the nanojunction driven by light

In 1973 Fleischmann *et al.* first reported the dramatic enhancement of the Raman scattering cross-section of molecules on rough metal surfaces [42], an effect confirmed in 1977 by Van Duyne *et al.* [43]. Two decades later, this technique known as surface-enhanced Raman scattering (SERS) enabled the detection of single molecules [44, 45]. Enhancement factors in the range of 10^{10} - 10^{14} have been reported to occur at "hot-spots" [46], regions of high electromagnetic fields associated with localized plasmonic resonances. Using the plasmon at the tip of a scanning tunnelling microscope [47] has led to a powerful analytical tool for sensitive Raman imaging: TERS (tip-enhanced Raman scattering). SERS and TERS both rely on the phenomenon of plasmon-enhanced Raman scattering, which is today widely employed in the fields of material and surface science [47], nanotechnology [48], chemistry [44] and even in-vivo biomedical applications [49].

The generally accepted model for SERS invokes the combined enhancement by the plasmonic hot-spot of the incoming electromagnetic field and the Raman scattered field [46, 50]. It predicts an enhancement of the Raman cross-section proportional to the fourth power of the field enhancement. Although this "E^4 law" has been verified experimentally, the observation of even larger enhancements and of an anomalous anti-Stokes/Stokes intensity ratio [51, 52] have suggested that a "vibrational pumping" mechanism was involved in cases where large pump intensity contributions were overcoming thermal ones [53]. Moreover, in recent experiments the maximal enhancement was achieved when the laser was blue-detuned from the plasmon resonance by the vibrational frequency (exciting the anti-Stokes vibrational sideband) [12, 54]. Under these conditions large nonlinear effects were also evidenced in Refs. [12, 55]. These observations are calling for a new theoretical understanding and for further investigations [56].

Here we show for the first time that SERS scenarios can be mapped onto the canonical model of cavity optomechanics [57] (Fig. 2.1a), in which a dynamic and coherent interaction takes place between two parametrically coupled and non-resonant harmonic oscillators, namely the molecular vibration and the plasmonic cavity. The optomechanical coupling rate can be computed from the Raman activity and the plasmonic field distribution, from which we derive

the Raman cross-section and recover conventional results.

The novel enhancement mechanism revealed by our approach is dynamical backaction amplification [58] of the vibrational mode due to the non-vanishing plasmon lifetime. This effect was first evidenced by the amplification of mechanical breathing modes in silica toroid microresonators [59] under blue-detuned excitation, leading to a range of new phenomena as reviewed in Ref. [60]. We find that SERS systems (i) can equally feature the suitable dissipation and frequency hierarchies (despite short plasmon decay times, i.e. low quality factors), and (ii) exhibit exceptionally large vacuum optomechanical coupling rates [61], so that under suitable conditions dynamical backaction amplification of the vibrational mode can occur via Raman scattering and lead to rich new physics, such as nonlinear dynamics and out-of-equilibrium vibrational occupancies.

2.1 Optomechanical model of the plasmon-vibration interaction

The plasmon mode is formally equivalent to an optical cavity and is modelled by a harmonic oscillator of frequency ω_p with bosonic creation $\hat{a}^\dagger$ and annihilation $\hat{a}$ operators and the Hamiltonian $\hat{H}_p = \hbar\omega_p\hat{a}^\dagger\hat{a}$ (Fig. 2.1a). Each normal vibrational mode of a molecule is described by an effective mass m_ν, a frequency Ω_ν and a normal coordinate x_ν with the corresponding position operator $\hat{x}_\nu = x_{\text{zpm},\nu}(\hat{b}_\nu^\dagger + \hat{b}_\nu)$, where $x_{\text{zpm},\nu} = \sqrt{\frac{\hbar}{2m_\nu\Omega_\nu}}$ is the zero-point motion and $\hat{b}_\nu^\dagger$, $\hat{b}_\nu$ are bosonic creation and annihilation operators. The few lowest energy levels of the molecular vibration are approximated by a harmonic oscillator, $\hat{H}_\nu = \hbar\Omega_\nu\hat{b}_\nu^\dagger\hat{b}_\nu$ (Fig. 2.1c; possible effects of anharmonicity are discussed later). The vibrational mode thermal occupancy at temperature T is given by $\bar{n}_\nu = \langle\hat{b}_\nu^\dagger\hat{b}_\nu\rangle = (\exp(\hbar\Omega_\nu/k_BT) - 1)^{-1}$ (k_B is the Boltzmann constant), which for high frequency Raman-active modes (1000 cm^{-1}, corresponding to $\Omega_\nu/2\pi = 30$ THz) is negligible at room temperature, even under moderate heating of the plasmonic particles.

2.1.1 Plasmon-vibration vacuum optomechanical coupling rate

The change in resonance frequency of a cavity when a dielectric is inserted in an air gap is described by [62]

$$\Delta\omega_p = -\frac{\omega_p}{2}\frac{\int_V \vec{P}\cdot\vec{E}_p\,dV}{U_{\text{cav}}} \tag{2.1}$$

where $U_{\text{cav}} = \frac{1}{2}\int\epsilon_0\frac{\mathrm{d}(\omega\epsilon(\omega))}{\mathrm{d}\omega}|\vec{E}_p|^2dV$ is the energy stored inside the plasmonic cavity [22], $\vec{E}_p$ the plasmonic cavity field and $\vec{P}$ the induced dipole per unit volume. As long as the plasmonic cavity dimension is sufficiently small in comparison to the incoming wavelength, the quasistatic approximation remains valid and the magnetic energy can be neglected. We can express the contribution of the electric field to the total energy stored in the metal by $U_{\text{cav}} = \mu U_d$ where $U_d = \frac{1}{2}\int\epsilon_0|\vec{E}_p|^2dV$ and the factor μ depends on the dielectric function of the metal and the plasmon resonance frequency [24].
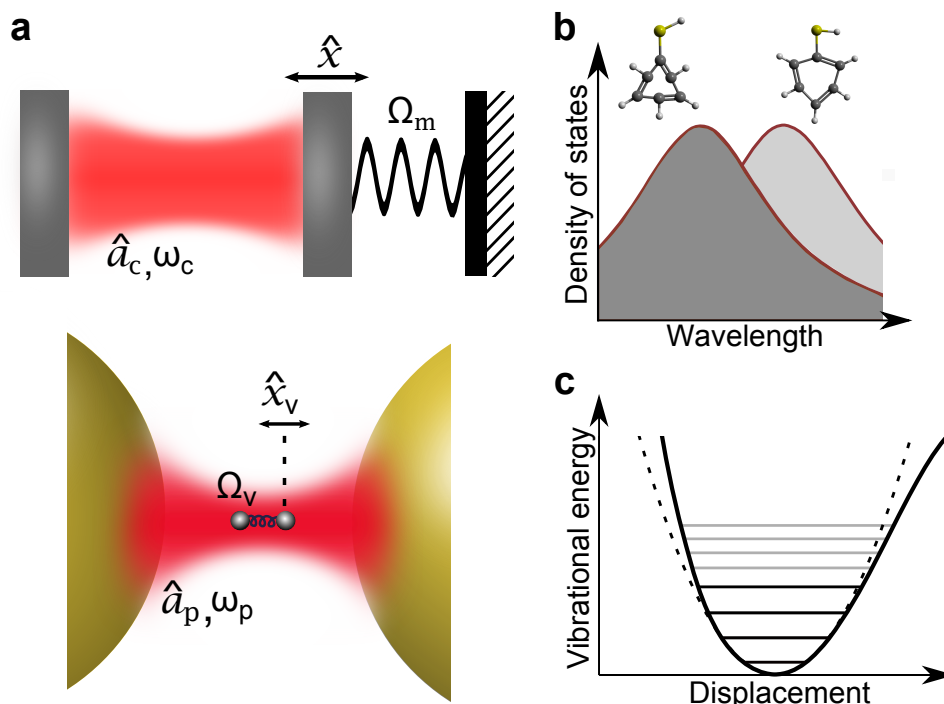
Figure 2.1 – **Cavity-optomechanical model of the interaction between plasmon and molecular vibration.** (**a**) Schematic mapping between an optical cavity with a mechanically compliant mirror (upper panel) and a plasmonic hot-spot and a molecule with internal vibrational mode (lower panel), sketched as two masses connected by a spring. Symbols for operators and frequencies of the case of interest are introduced in the text, with $\hat{a}_p$ denoted as $\hat{a}$ for simplicity. (**b**) During vibrational motion the change in polarizability of the molecule (thiophenol in this figure) leads to a shift of the plasmon resonance frequency, Eq. (2.10), at the origin of the parametric optomechanical coupling. (**c**) Schematic molecular potential as a function of the vibrational coordinate. The harmonic oscillator description is valid for small vibration amplitudes (low excitation numbers, dark lines) but anharmonicity must be taken into account under high amplification (higher levels, gray lines).

We assume that a single molecule is located at the position of maximum electric field. Introducing the molecular dipole moment $\vec{p}$

$$\Delta\omega_p \approx -\frac{\omega_p}{2}\frac{\vec{p}\cdot\vec{E}_{\max}}{\mu U_d} \tag{2.2}$$

The induced dipole is related to the electric field by $\vec{p} = \alpha\cdot\vec{E}_{\max}$; the dependence of the linear polarizability α on the molecular displacement x_v is developed to first order

$$\vec{p} = \alpha(x_v)\cdot\vec{E}_{\max} \approx \left(\alpha(0) + \frac{\partial\alpha}{\partial x_v}x_v\right)\cdot\vec{E}_{\max} \tag{2.3}$$

where the gradient of polarizability $\frac{\partial\alpha}{\partial x_v}$ has units $\left[\epsilon_0 m^2\right]$. Note that in the expression for the polarizability of the molecule contains the contributions from the internal electonic transitions so that it is frequency dependent.

We can now quantify the sensitivity of the plasmonic frequency to the molecular vibrations to first order in x_v

$$G_v = \frac{\partial\left(\Delta\omega_p\right)}{\partial x_v} = -\frac{\omega_p}{2}\frac{\frac{\partial\alpha}{\partial x_v}|\vec{E}_{\max}|^2}{\mu U_d} = -\frac{\omega_p}{\epsilon_0 V_m}\frac{\partial\alpha}{\partial x_v} \tag{2.4}$$

expressed as a function of the effective mode volume of the cavity $V_m \doteq \frac{\mu U_d}{\frac{1}{2}\epsilon_0 |E_{\max}|^2}$. When the plasmon resonance frequency gets closer to the bulk plasma frequency, the energy stored in the metal grows and the mode volume defined here increases [24].

We have thus shown that the plasmon frequency is coupled to the molecular vibration and that this coupling can be quantified by the optomechanical vacuum coupling rate (also called single photon coupling rate)

$$g_{v,0} = G_v x_{\mathrm{zpm},v} = \omega_p\frac{\partial\alpha}{\partial x_v}\frac{1}{V_m\epsilon_0}\sqrt{\frac{\hbar}{2m_v\Omega_v}} \tag{2.5}$$

with V_m the mode volume of the plasmonic cavity [63] and ϵ_0 the permittivity of vacuum. The coupling rate here defined describes the plasmon frequency shift due to the zero-point motion of the molecular vibration. Applying the concepts used in optomechanics, we are thus able to find a quantitative way of describing the interaction between the molecular vibrations and the plasmonic resonance.

2.1.2 Calculation of g_0

Following the conventions used in Raman spectroscopy we use instead of the normal coordinates x_v the reduced coordinates $Q_v = \sqrt{m_{\mathrm{eff},v}}x_v$ with units $\left[\mathrm{kg}^{-1/2}\mathrm{m}\right]$, referred to as *the mass-weighted Cartesian displacement coordinates* [17]. In this notation the kinetic energy is given by $E_K = \frac{1}{2}\sum_{v=1}^{3N}\dot{Q}_v^2$. Expressing the vacuum coupling rate (2.5) in the reduced coordinates

Q_v leads to

$$g_{v,0} = \omega_p \left(\frac{\partial \alpha}{\partial Q_v}\right) \left(\frac{1}{V_m \epsilon_0}\right) \sqrt{\frac{\hbar}{2\Omega_v}} \tag{2.6}$$

In optomechanical systems the effective mass is defined such that it verifies the equipartition theorem ($\frac{1}{2} m_{\text{eff},v} \Omega_v^2 x_v^2 = U_v$), with U_v the energy stored in this mode.

The vacuum optomechanical coupling rate (2.5) can be reexpressed using the DFT calculations of Section 1.1

$$g_0 = \frac{4\pi\epsilon_0 \cdot 10^{-20}}{\sqrt{1.66 \cdot 10^{-27}}} \omega_p \left[\frac{1}{V_m \epsilon_0}\right] \sqrt{\frac{\hbar}{2\Omega_v}} \sqrt{R_v[\text{g.u.}]} \tag{2.7}$$

Experimental studies usually express the resonance of the plasmon in [nm] and the wavenumber $\tilde{v}$ of the vibrational mode in [cm^{-1}], being related to the angular frequency via

$$\Omega_v / 2\pi \text{ [Hz]} = c\tilde{v}[\text{cm}^{-1}] \cdot 10^2 \tag{2.8}$$

For numerical approximations below we will consider that the resonance of the plasmon is around 900 nm and we will express it in angular frequency $\omega_p/2\pi$ [Hz] $= \frac{c}{\lambda_p[\text{nm}]} \cdot 10^9$.

The vacuum coupling rate can finally be expressed as a function of experimentally used parameters

$$\frac{g_0}{2\pi} \text{ [Hz]} = \left(\frac{1}{V_m}\right) 2 \cdot 10^{\frac{3}{2}} \sqrt{\frac{c\hbar\pi}{1.66}} \frac{\sqrt{R_v[\text{g.u.}]}}{\lambda_p[\text{nm}]\sqrt{\tilde{v}[\text{cm}^{-1}]}} \tag{2.9}$$

Note on the coupling rate : The derivation described here corresponds to the first order coupling term. In some specific situations and following an equivalent derivation, the higher order contributions could be calculated in order for example to account for the field gradients inside the nanojunction [64]. These higher order contributions remain to be analytically and numerically evaluated. Similarly, following the generalized QNM formalism, the variation of the complex modal eigenfrequency [65] could be divided in a real part, related to the previous derivation of the dispersive optomechanical coupling, and an additional part describing possibly different dissipative optomechanical couplings [66].

2.1.3 Examples of coupling rate values

Here we compute the vacuum optomechanical coupling rate between several molecules and the localized surface plasmon of a dimer nanoparticle. Molecular parameters were obtained from the literature (see Table 2.1 for references). We used experimental parameters [54] to give a realistic approximation of the mode volume. According to the geometrical estimate used in [67], we can approximate the mode volume arising from the field contribution only as $V_m^d \sim r^{1/2} d^{3/2} h$ with r the radius of the cylinder, h its height and d the size of the gap. We note that for the experimental case studied the plasmonic resonance frequency is sufficiently

below the bulk plasma frequency of gold so that the contributions from the field and charges can be considered equals [24]. We recover in this case the expected equivalence between the two energy contributions valid generally for non-dispersive materials and the effective mode volume is then given by $V_m = \mu V_m^d$ with $\mu \simeq 2$. We present in Table 2.1 the molecular parameters of interest and the related optomechanical coupling for different vibrational modes.

molecule	$\Omega_\nu/2\pi$ [THz] ([cm^{-1}])	R_ν [Å^{4}amu^{-1}]	estimated $g_{\nu,0}/2\pi$ [Hz]
R6G[68]	39 (1301)	5.9	$7.9 \cdot 10^9$
R6G	40.5 (1351)	351.7	$6.0 \cdot 10^{10}$
Thiophenol[69]	29.9 (998)	31.6	$2.1 \cdot 10^{10}$
Thiophenol	32.1 (1072)	1.7	$4.7 \cdot 10^9$
GBT[69]	30 (1000)	29.5	$2.0 \cdot 10^{10}$
GBT	32.2 (1075)	388.5	$7.0 \cdot 10^{10}$
G-band of graphene or CNT	~48 (~ 1600)	~ 10^3–10^4	~ 10^{10}–10^{11}

Table 2.1 – Vacuum optomechanical coupling rates ($g_{\nu,0}/2\pi$) calculated with parameters from the literature. We used a plasmonic mode volume $V_m \sim 1.5 \cdot 10^{-6} \mu\text{m}^3$ and resonance of the plasmon $\lambda_p = 900$ nm (corresponding to the experimental case [54]). Values for graphene and carbon nanotubes (CNT) are estimated using Raman activity from the literature [70] (we obtain similar values for the radial breathing mode of CNTs).

Since the frequency hierarchy $\omega_p \gg \Omega_\nu$ is satisfied, and assuming the molecule has no optically allowed electronic transitions resonant with the plasmon, the coupling between vibrational and plasmonic modes is purely *parametric*: the vibrational displacement causes a dispersive shift of the plasmon resonance frequency (Fig. 2.1b) which can be expressed, to first order, as

$$\omega_p(x_\nu) = \omega_p - G_\nu \cdot x_\nu \tag{2.10}$$

This is analogous to the case of optomechanical systems [71], as opposed to resonant coupling scenarios [72, 73].

2.1.4 Derivation of the classical equations of motion

The Hamiltonian for the complete system $\hat{H} = \hat{H}_p + \hat{H}_\nu + \hat{H}_{\text{int}}$ is thus formally identical to the one obtained in cavity optomechanics, with an interaction term [60]

$$\hat{H}_{\text{int}} = -\hbar g_{\nu,0} \hat{a}^\dagger \hat{a}(\hat{b}_\nu^\dagger + \hat{b}_\nu) \tag{2.11}$$

that describes the coherent coupling between a mechanical oscillator (here the molecular vibration) and an electromagnetic cavity mode (here the localized plasmon). The vibration acts on the plasmon via the dispersive plasmon frequency shift of eq. (2.10) that can change the plasmon occupancy $n_P(t) = \langle \hat{a}^\dagger(t)\hat{a}(t)\rangle$. In turn, the plasmon acts back on the vibration

via the *time-dependent* generalized force

$$F_P(t) = \hbar G_v n_P(t).$$ (2.12)

The delay in the plasmonic cavity field response to changes in the resonance frequency leads to a component of the force that is out of phase with respect to the vibrational motion, and hence proportional to its velocity , leading to a damping or amplification of the molecular vibration. When the cavity decay rate is smaller or equal to twice the vibrational frequency (i.e. resolved vibrational sidebands, $\Omega_m \gtrsim \kappa/2$) the phase shift can attain values of $\pm \pi/2$ for a driving laser detuned to the phonon sideband ($|\Delta| \sim \Omega_v$) [74]. This leads to a purely viscous force and efficient dynamical backaction amplification.

Interestingly, for realistic values of the plasmon quality factor ($Q \sim 10$) [3] in the near-infrared frequency range ($\omega_p/2\pi \sim 330$ THz for $\lambda = 900$ nm) and a typical linewidth (~ 2 cm^{-1} [75]) and frequency (1000 cm^{-1}) of the Raman-active vibrational modes, one obtains a plasmonic dissipation rate $\kappa/2\pi = 33$ THz, a vibrational dissipation rate $\Gamma_v/2\pi = 0.06$ THz and a vibrational frequency $\Omega_v/2\pi = 30$ THz. Consequently, despite the short plasmon lifetime $2\pi/\kappa = 30$ fs, the system can attain the resolved sideband limit, as $\frac{\Omega_m}{\kappa/2} \approx 2$. Hence, there can be sufficient retardation compared to the vibrational period $2\pi/\Omega_v = 33$ fs for efficient dynamical backaction amplification.

The resulting dynamical backaction can be understood and described as a delayed feedback loop (Fig. 2.2b) [76]. In the frequency domain, the plasmonic and vibrational time responses correspond to spectral filtering. The transduction from plasmon to vibration occurs through the force F_P, with an amplification factor proportional to the intracavity plasmonic field $\sqrt{\bar{n}_P}$ (induced by the pump laser) and to the Raman polarizability $\frac{d\alpha}{dx_v}$ (contained in G_v). The average intracavity occupation of the plaasmonic mode can be expressed in terms of the incoming photon flux or incoming power by

$$\bar{n}_P = |\langle \hat{a}^{\text{in}} \rangle|^2 \frac{\kappa_{\text{ex}}}{\Delta^2 + (\kappa/2)^2} = \frac{P^{\text{in}}}{\hbar\omega_p} \frac{\kappa_{\text{ex}}}{\Delta^2 + (\kappa/2)^2}.$$ (2.13)

In a quantum mechanical treatment, the linearization of the Hamiltonian around the mean photon number in the cavity [60, 77] takes the form $\hat{H}_{\text{int}} = -\hbar g_{v,0} \sqrt{\bar{n}_P}(\hat{a}^\dagger \hat{b}_v^\dagger + \hat{a}\hat{b}_v)$ for a laser that is tuned to the upper (blue) vibrational sideband in the resolved sideband regime ($\Omega_v > \kappa/2$). Amplification in this case occurs due to the first term, that generates photon-phonon pairs [78].

We introduce the vacuum optomechanical coupling rate presented in Section 2.1.2 :

$$g_{v,0} = \omega_p \left(\frac{\partial \alpha}{\partial Q_v} \right) \left(\frac{1}{V_m \epsilon_0} \right) \sqrt{\frac{\hbar}{2\Omega_v}}$$ (2.14)

The Raman activity, described in its most general terms by the Raman tensor R_v, satisfies in a

simplified one dimensional model $R_v = \left(\frac{\partial \alpha}{\partial Q_v}\right)^2$. When considering the small mode volume in plasmonic dimers ("hot-spots"), even for small individual molecules, and without considering possible enhancement from electronic resonances, we found optomechanical coupling rates $g_{v,0}/2\pi$ of $\mathcal{O}(10-100)$ GHz (Table 2.1), which are 4 to 5 orders of magnitudes larger than those observed in state-of-the-art microfabricated optomechanical structures [79].

We present in the following a simple treatment of the optomechanical system to give an intuitive picture of some first important phenomena. A complete derivation including all the assumptions made can be found in reviews on cavity optomechanics [60], [80].

We start from the expression describing the interaction between a radiation mode and a vibrational mode v introduced earlier

$$\hat{H}_0 = \hbar\omega_p \hat{a}^\dagger \hat{a} + \hbar\Omega_v \hat{b}^\dagger \hat{b} - \hbar G_v x_{\mathrm{zpm},v} \hat{a}^\dagger \hat{a}\left(\hat{b}^\dagger + \hat{b}\right) \tag{2.15}$$

(We recall the expression of the zero-point motion: $x_{\mathrm{zpm},v} = \sqrt{\frac{\hbar}{2m_v\Omega_v}}$).

A first derivation of this optomechanical Hamiltonian was given by Law [81]. The interaction term is corresponding to a nonlinear process that involves a product of three operators. The driving laser at frequency ω_L is modelled by a coherent field: $\hat{H}_L = i\hbar\alpha\sqrt{\kappa_{ex}}\left(e^{-i\omega_L t}\hat{a}^\dagger - e^{i\omega_L t}\hat{a}\right)$. It is convenient to switch to a reference frame rotating at the laser frequency, in which the total Hamiltonian writes

$$\hat{H} = e^{i\omega_L\hat{a}^\dagger\hat{a}t}\left(\hat{H}_0 + \hat{H}_L\right)e^{-i\omega_L\hat{a}^\dagger\hat{a}t} - \hbar\omega_L\hat{a}^\dagger\hat{a} \tag{2.16}$$

Making use of the Baker-Campbell-Hausdorff formula, this change of reference frame allows to eliminate the explicit time dependence of the Hamiltonian. Dissipations can be introduced by writing the quantum Langevin equations. Within the input-output formalism [82], defining $\Delta = \omega_L - \omega_p$ as the detuning between the laser and the plasmon, we obtain the equations

$$\begin{aligned}
\frac{d\hat{a}}{dt} &= -\frac{i}{\hbar}\left[\hat{a},\hat{H}\right] - \frac{\kappa_0 + \kappa_{ex}}{2}\hat{a} + \sqrt{\kappa_0}\delta\hat{a}_0^{in} + \sqrt{\kappa_{ex}}\delta\hat{a}_{ex}^{in} \\
&= \left(i\Delta - \frac{\kappa}{2}\right)\hat{a} + iG_v x_{\mathrm{zpm},v}\hat{a}\left(\hat{b}^\dagger + \hat{b}\right) + \sqrt{\kappa_0}\delta\hat{a}_0^{in} + \sqrt{\kappa_{ex}}\left(\alpha + \delta\hat{a}_{ex}^{in}\right)
\end{aligned} \tag{2.17}$$

$$\begin{aligned}
\frac{d\hat{b}}{dt} &= -\frac{i}{\hbar}\left[\hat{b},\hat{H}\right] - \frac{\Gamma_v}{2}\hat{b} + \sqrt{\Gamma_v}\delta\hat{b}_{in} \\
&= \left(-i\Omega_v - \frac{\Gamma_v}{2}\right)\hat{b} + iG_v x_{\mathrm{zpm},v}\hat{a}^\dagger\hat{a} + \sqrt{\Gamma_v}\delta\hat{b}_{in}
\end{aligned} \tag{2.18}$$

where we introduced the input noise terms expressed in the rotating frame: the vacuum noise $\delta\hat{a}_0^{in}$ and driving laser's noise $\delta\hat{a}_{ex}^{in}$ entering the plasmonic cavity, and the thermal noise $\delta\hat{b}_{in}$ on the vibrational mode. Assuming a shot-noise limited laser and neglecting the thermal excitation at the plasmon frequency, the correlators associated with these fluctuations are
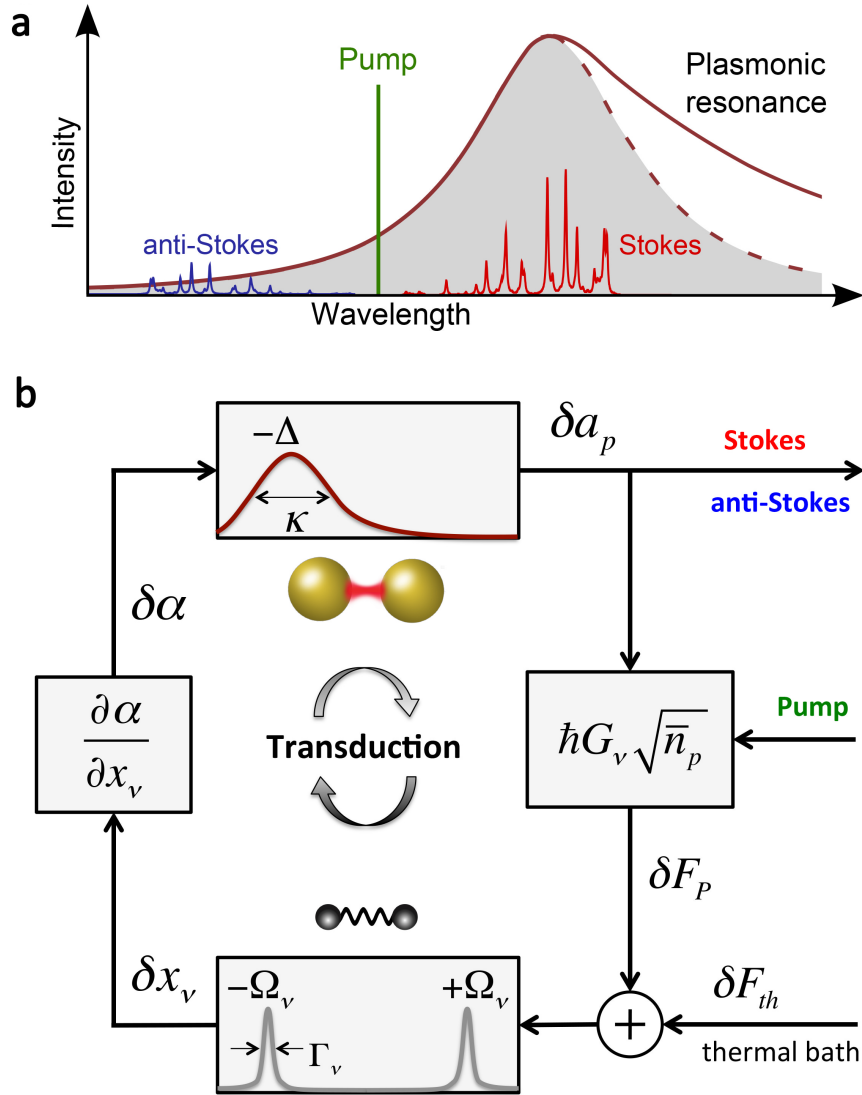
Figure 2.2 – **Feedback diagram of dynamical backaction in the SERS process.** (**a**) Schematic Raman spectrum. When the pump (represented in green) is blue-detuned by approximately the vibrational frequency, $\Delta \sim \Omega_v$, the Stokes process (red) is selectively enhanced over the anti-Stokes process (blue) by the plasmonic resonance (brown line) described by a Lorentzian with linewidth κ in the model (shaded area). (**b**) Equivalent feedback diagram of the system. Variables (fluctuations from average) are indicated along the arrows and boxes represent transfer functions. The equations of motion have been linearized and frequencies are relative to the pump laser . The pump power controls the amplification factor (via the average plasmon occupancy $\bar{n}_P$) in the transduction from the plasmonic field δa_p to the force δF_P. The latter acts, together with the thermal force δF_{th}, on the molecular displacement δx_v. The molecular oscillator acts as a filter of linewidth Γ_v at frequencies $\pm\Omega_v$. The displacement is transduced via the Raman activity ($\partial\alpha/\partial x_v$) in a change in polarizability $\delta\alpha$, which modulates the plasmonic field introduced in (a), closing the feedback loop.

given by:

$$\left\langle \delta \hat{a}_{\text{in}}^{\dagger}(t) \delta \hat{a}_{\text{in}}(t') \right\rangle \;=\; 0 \tag{2.19}$$

$$\left\langle \delta \hat{a}_{\text{in}}(t) \delta \hat{a}_{\text{in}}^{\dagger}(t') \right\rangle \;=\; \delta(t - t') \tag{2.20}$$

$$\left\langle \delta \hat{b}_{\text{in}}^{\dagger}(t) \delta \hat{b}_{\text{in}}(t') \right\rangle \;=\; \bar{n}_v \delta(t - t') \tag{2.21}$$

$$\left\langle \delta \hat{b}_{\text{in}}(t) \delta \hat{b}_{\text{in}}^{\dagger}(t') \right\rangle \;=\; (\bar{n}_v + 1) \delta(t - t') \tag{2.22}$$

where $\bar{n}_v$ is the thermal occupancy of the bath at the vibrational frequency Ω_v (valid for sufficiently high vibrational quality factor).

The equations of motion for the corresponding creation operators are obtained from the relations $\dfrac{\mathrm{d}}{\mathrm{d}t}\left(\hat{a}^{\dagger}\right) = \left(\dfrac{\mathrm{d}\hat{a}}{\mathrm{d}t}\right)^{\dagger}$, $\dfrac{\mathrm{d}}{\mathrm{d}t}\left(\hat{b}^{\dagger}\right) = \left(\dfrac{\mathrm{d}\hat{b}}{\mathrm{d}t}\right)^{\dagger}$. These equations describe the complete evolution of the plasmonic excitations coupled to the molecular vibrations. It is instructive to give first their classical version.

We express the vibrational degree-of-freedom in the position and momentum operators defined by

$$\hat{x}_v = x_{\text{zpm},v}\left(\hat{b}^{\dagger} + \hat{b}\right) \tag{2.23}$$

$$\hat{p}_v = i x_{\text{zpm},v} m_v \Omega_v \left(\hat{b}^{\dagger} - \hat{b}\right) \tag{2.24}$$

In this representation the Langevin equations for the vibrational mode become

$$\frac{\mathrm{d}\hat{x}_v}{\mathrm{d}t} \;=\; \frac{\hat{p}_v}{m_v} - \frac{\Gamma_v}{2}\hat{x}_v + \sqrt{\Gamma_v}\delta\hat{x}_{\text{in}} \tag{2.25}$$

$$\frac{\mathrm{d}\hat{p}_v}{\mathrm{d}t} \;=\; -m_v\Omega_v^2\hat{x}_v + \hbar G_v\hat{a}^{\dagger}\hat{a} - \frac{\Gamma_v}{2}\hat{p}_v + \sqrt{\Gamma_v}\delta\hat{p}_{\text{in}} \tag{2.26}$$

where $\delta\hat{x}_{\text{in}}$ and $\delta\hat{p}_{\text{in}}$ are the quantum noise operators.

After taking expectation values the noise terms average to zero and one obtains

$$\dot{a} - i(\Delta + G_v x_v)a + \frac{1}{2}\kappa a \;=\; \sqrt{\kappa_{\text{ex}}}s \tag{2.27}$$

$$\ddot{x}_v + \Gamma_v\dot{x}_v + \Omega_v^2 x_v \;=\; \frac{F_P(t)}{m_v} \tag{2.28}$$

where $a = \langle \hat{a} \rangle$ and $x_v = \langle \hat{x}_v \rangle$. The force on the r.h.s. of eq. (2.28) is of purely electromagnetic origin, given by $F_P = \hbar G_v |a(t)|^2$ with $|a|^2 = \left\langle \hat{a}^{\dagger}\hat{a} \right\rangle$.

2.1.5 Linearization of the cavity field

To solve the equations of motion, we follow a linearization procedure [80]. Setting the time derivatives to zero in the system of equations described above, we find the stationary solutions

$$\bar{a} = \frac{\sqrt{\kappa_{\text{ex}}}\alpha}{-i\left(\Delta + G_v \bar{x}_v\right) + \frac{\kappa}{2}} \qquad \bar{x}_v = \frac{\hbar G_v}{m_v \Omega_v^2}|a|^2 \tag{2.29}$$

We assume that the amplitude of the vibrations is described by $x_v(t) = x_{v,0}\cos(\Omega_v t)$ and is small in comparison to the typical length scale L of the plasmonic cavity. A large vibrational motion - arising above the parametric instability threshold - would break our linear treatment and the contributions of the non-linear terms would have to be considered [83]. We introduce $\epsilon = \frac{x_{v,0}}{L} \ll 1$ and use this small dimensionless parameter to develop the cavity field variable in a power series $a = \sum_{n=0}^{\infty} \epsilon^n a_n$. The power expansion of the equation (2.27) yields

$$\sum_{n=0}^{\infty} \epsilon^n \frac{da_n}{dt} = \sum_{n=0}^{\infty}\left[\left(i\Delta - \frac{\kappa}{2}\right)\epsilon^n a_n + iG_v L\epsilon^{n+1} a_n \cos(\Omega_v t)\right] + \sqrt{\kappa_{\text{ex}}}\alpha \tag{2.30}$$

0th order equation

$$\frac{da_0}{dt} = \left(i\Delta - \frac{\kappa}{2}\right)a_0 + \sqrt{\kappa_{\text{ex}}}\alpha \tag{2.31}$$

The homogeneous solution can be neglected if the measurement time is much longer than the other timescales in the system (as is always the case in SERS). We can thus consider only the particular solution, equal to the steady-state solution without optomechanical coupling

$$a_0 = \frac{\sqrt{\kappa_{\text{ex}}}\alpha}{-i\Delta + \frac{\kappa}{2}} \tag{2.32}$$

1st order equation

$$\frac{da_1}{dt} = \left(i\Delta - \frac{\kappa}{2}\right)a_1 + iG_v L a_0 \cos(\Omega_v t) \tag{2.33}$$

We can neglect the homogeneous solution following the same reasoning as before. We look for a particular solution of the form $a_1(t) = a_{\text{AS}}e^{i\Omega_v t} + a_{\text{S}}e^{-i\Omega_v t}$ and obtain the amplitudes of the anti-Stokes and the Stokes fields, respectively

$$a_{\text{AS}} = \frac{G_v L}{2}\frac{a_0}{\Omega_v - \Delta - i\frac{\kappa}{2}} \qquad a_{\text{S}} = -\frac{G_v L}{2}\frac{a_0}{\Omega_v + \Delta + i\frac{\kappa}{2}} \tag{2.34}$$

2.1.6 A classical look at the optomechanical damping rate

We develop the expression of the force to first order in ϵ

$$F_P(t) = \hbar G_v |a(t)|^2 \simeq \hbar G_v |a_0 + \epsilon a_1(t)|^2 = \hbar G_v |a_0|^2 + 2\epsilon\hbar G_v \Re\left(a_0 a_1^*(t)\right) \tag{2.35}$$

In the last expression, the first term corresponds to a constant force applied to the vibrational mode $\bar{F}_P = \hbar G_v |a_0|^2$. The second term is time-dependent and can be expressed as a sum of in- and out-of-phase components

$$\delta F_P(t) = \cos(\Omega_v t)\,\delta F_I + \sin(\Omega_v t)\,\delta F_Q \tag{2.36}$$

with

$$\delta F_I = \hbar G_v^2 x_v |a_0|^2 \left[\frac{(\Omega_v - \Delta)}{(\Omega_v - \Delta)^2 + \left(\frac{\kappa}{2}\right)^2} - \frac{(\Omega_v + \Delta)}{(\Omega_v + \Delta)^2 + \left(\frac{\kappa}{2}\right)^2} \right] \tag{2.37}$$

$$\delta F_Q = \hbar G_v^2 x_v |a_0|^2 \left[\frac{\frac{\kappa}{2}}{(\Omega_v + \Delta)^2 + \left(\frac{\kappa}{2}\right)^2} - \frac{\frac{\kappa}{2}}{(\Omega_v - \Delta)^2 + \left(\frac{\kappa}{2}\right)^2} \right] \tag{2.38}$$

We can now insert the expression for the electromagnetic force into the equation of motion (2.28)

$$m_v \ddot{x}_v = m_v \Omega_v \Gamma_v x_{v,0} \sin(\Omega_v t) - m_v \Omega_v^2 x_{v,0} \cos(\Omega_v t)$$
$$+ \bar{F}_P + \cos(\Omega_v t)\,\delta F_I + \sin(\Omega_v t)\,\delta F_Q \tag{2.39}$$

$$m_v \ddot{x}_v = -m_v \Gamma_v' \dot{x}_v - m_v \Omega_v'^2 x_v + \bar{F}_P \tag{2.40}$$

The equation is thus describing a mechanical oscillator displaced by a constant force $\bar{F}_P$, with a shifted natural frequency Ω_v' and damped at an effective rate Γ_v'

$$\Gamma_v' = \Gamma_v + \frac{\delta F_Q}{m_v \Omega_v x_{v,0}} := \Gamma_v + \Gamma_{\text{opt}} \tag{2.41}$$

$$\Omega_v' = \sqrt{\Omega_v^2 - \frac{\delta F_I}{m_v x_{v,0}}} \tag{2.42}$$

Depending on the laser detuning from the (shifted) plasmonic resonance, three different situations can arise:

- $\Delta = 0$: For resonant excitation there is no radiation-induced change of the damping rate

- $\Delta < 0$: For a red-detuned laser, the damping rate is increased, corresponding to "cooling" [84]

- $\Delta > 0$: For a blue-detuned laser, the damping rate is decreased, corresponding to amplification [59]

Deep in the sideband-resolved regime ($\kappa \ll \Omega_v$) [85] the maximal increase (decrease) of the damping rate is obtained when $\Delta = -\Omega_v$ ($\Delta = \Omega_v$) and the expression for the maximum

backaction damping rate due to optomechanical interactions can be approximated by

$$\Gamma_{\text{opt}} = \Gamma_v' - \Gamma_v = \frac{4\bar{n}_p g_{v,0}^2}{\kappa} \tag{2.43}$$

where $g_{v,0} = G_v \sqrt{\frac{\hbar}{2m_v \Omega_v}}$ is the vacuum optomechanical coupling rate. When the damping is increased trough the coupling with the plasmonic field (red detuning), the vibrational mode is losing power into the plasmonic cavity and thus is being optically "cooled". On the contrary, when the damping rate is decreased (blue detuning), power is transferred from the plasmonic field to the vibrational mode, whose motion is thereby amplified: this is dynamical backaction amplification.

More generally, we can express the full optomechnical damping rate for any detuning (Γ_{opt}) as

$$\Gamma_{\text{opt}} = \Gamma_v' - \Gamma_v = A^- - A^+ \tag{2.44}$$

where we introduced the antenna-assisted transition rate to the lower (A^-) and higher (A^+) excited vibrational level [60] that can with help of the previous equations be expressed as :

$$A^- = \left(g_{v,0}\right)^2 \bar{n}_p \frac{\kappa}{(\Omega_v - \Delta)^2 + (\kappa/2)^2}. \tag{2.45}$$

$$A^+ = \left(g_{v,0}\right)^2 \bar{n}_p \frac{\kappa}{(\Omega_v + \Delta)^2 + (\kappa/2)^2}. \tag{2.46}$$

2.1.7 Collective optomechanical plasmon-vibrational coupling

In this section, we consider N identical phonon modes – with annihilation operators $\hat{b}_{i=1,...,N}$ – coupled to the same plasmonic cavity. Corresponding experimental situations include (i) a layer of molecules filling the gap of a metal dimer [54], where each $\hat{b}_i$ represents the same Raman mode for each molecule; (ii) the optical phonon of a piece of bulk or 2D material interacting with a plasmonic cavity, where each $\hat{b}_i$ represent the same vibrational mode of each unit cell (for example the G-band of graphene in [86]). For simplicity we consider identical vibrational frequencies $\Omega_v^{(i)} = \Omega$, intrinsic damping rates $\Gamma_v^{(i)} = \Gamma$ and coupling rates to the cavity $G_v^{(i)} = G$. To illustrate the effect we consider the case described in [87], starting from the Langevin equations in the rotating frame of the molecular vibration and of the Stokes field. The cavity field evolution can be adiabatically eliminated and replaced by its steady state solution. This leads to a linear system of N differential equations describing the evolution of the N phonon modes coupled via the cavity driven by a laser tuned on the anti-Stokes (blue) vibrational sideband:

$$\dot{\hat{b}}_i = -\left(\Gamma + \Gamma_{\text{opt}}\right)\hat{b}_i + \sum_{j \neq i} \Gamma_{\text{opt}}\hat{b}_j \tag{2.47}$$

The N solutions of these equations reveal two different behaviours. On the one hand, we find $N-1$ linearly independent and degenerate eigenmodes $\hat{D}_k$ ($k \in [1, N-1]$) with the same eigenvalue $\{-\Gamma\}$ that can be written in the general form:

$$\frac{1}{K_k} \sum_j \lambda_{k,j} \hat{b}_j \quad \text{with} \quad K_k = \sqrt{\sum_j |\lambda_{k,j}|^2} \tag{2.48}$$

such that $\sum_j \lambda_{k,j} = 0 \quad \forall k \in [1, N-1]$. The shift of the plasmonic resonance caused by each of the collective modes $\hat{D}_k$ is proportional to its collective optomechanical coupling rate $G_k = \sum_j \lambda_j G = 0$. This shows that these modes are dark, i.e. decoupled from the plasmonic cavity and thus not affected by dynamical backaction.

On the other hand, the eigenmode $\hat{B} = \frac{1}{\sqrt{N}} \sum_i \hat{b}_i$ with eigenvalue $\{-\Gamma + N\Gamma_{\text{opt}}\}$ (the equivalent of the superradiant mode in cavity QED) is the only collective mode coupled to the cavity and its backaction damping rate is enhanced by a factor N, i.e. $\Gamma_{\text{opt}}^{(B)} \equiv N \cdot \Gamma_{\text{opt}}$. A more general treatment appropriate for the system treated in our study is developed in [88] and leads to the same conclusions. This scaling translates to a $\sqrt{N}$ scaling of $g_{v,0}$ (see equation 8 of the main text).

2.2 Description of the Raman cross-section using the optomechanical formalism

To highlight how this formalism relates to the classical picture of SERS it is interesting to follow a semi-classical derivation without including backaction effects. Writing the Stokes scattered power as $P_S/\hbar\omega_L = \eta\kappa|\epsilon a_S|^2$ and expressing a_S following eq. (2.34) yields

$$P_S/\hbar\omega_L = \left| \frac{1}{2} x_v G_v \left(\frac{\sqrt{\eta\kappa}}{-i\Delta + \kappa/2} \right) \left(\frac{s\sqrt{\eta\kappa}}{(\Omega_v - \Delta) - i\kappa/2} \right) \right|^2 \tag{2.49}$$

Here, we assume that the vibrational amplitude is related to the thermal energy, i.e. $\frac{1}{2} m_v \Omega_v^2 \langle x_v^2 \rangle = \frac{1}{2} k_B T$. To describe the quantum mechanical nature of the transition process, we replace $|x_v|^2$ by the corresponding transition matrix element, describing the probability to undergo the transition $|n\rangle \rightarrow |n \pm 1\rangle$ for Stokes and anti-Stokes scattering, respectively. Each transition element is weighted by the Boltzmann factor, characterizing the energy level occupation of the thermal state:

$$|x_v|^2 \underset{S}{\rightarrow} \sum_{n_v} |\langle n_v + 1|\hat{x}_v|n_v\rangle|^2 \, p(n_v) = \frac{x_{\text{zpm},v}^2}{\bar{n}_v + 1} \sum_{n_v=0}^{\infty} (n_v + 1) \left(\frac{\bar{n}_v}{\bar{n}_v + 1} \right)^{n_v} = x_{\text{zpm},v}^2 (\bar{n}_v + 1) \tag{2.50}$$

$$|x_v|^2 \underset{AS}{\rightarrow} \sum_{n_v} |\langle n_v - 1|\hat{x}_v|n_v\rangle|^2 \, p(n_v) = \frac{x_{\text{zpm},v}^2}{\bar{n}_v + 1} \sum_{n_v=1}^{\infty} n_v \left(\frac{\bar{n}_v}{\bar{n}_v + 1} \right)^{n_v} = x_{\text{zpm},v}^2 \bar{n}_v \tag{2.51}$$

where we used $p(n_v) = \frac{1}{\bar{n}_v+1}\left(\frac{\bar{n}_v}{\bar{n}_v+1}\right)^{n_v}$ to describe the probability to find a vibrational thermal state in its n-th occupational level. The Stokes (anti-Stokes) cross-section is defined as $\sigma_{S(AS)} = P_{S(AS)}/I$ with $I = P_{in}/A_{eff}$. P_{in} is the incident power coupled to the plasmonic cavity and A_{eff} the illuminating spot area. Since this spot is large compared to the size of the plasmonic system the radiative coupling rate satisfies $\kappa_{ex} \propto A_{eff}^{-1}$ so that $\kappa_{ex}A_{eff}$ is approximately constant. As the incoming photon flux number is $|\alpha|^2 = P_{in}/\hbar\omega_L$, $\sigma_{S(AS)}$ are found to be

$$\sigma_S^{em} = \frac{\eta A_{eff}}{4}\left(\frac{G_v x_{zpm,v}}{\kappa}\right)^2\left(\frac{1}{\Delta^2/\kappa^2+1/4}\right)\left(\frac{1}{(\Delta-\Omega_v)^2/\kappa^2+1/4}\right)(\bar{n}_v+1) \qquad (2.52)$$

$$\sigma_{aS}^{em} = \frac{\eta A_{eff}}{4}\left(\frac{G_v x_{zpm,v}}{\kappa}\right)^2\left(\frac{1}{\Delta^2/\kappa^2+1/4}\right)\left(\frac{1}{(\Delta+\Omega_v)^2/\kappa^2+1/4}\right)\bar{n}_v \qquad (2.53)$$

To see how this formalism (without backaction) recovers the conventional theory, we note that the field inside the plasmonic cavity E_{loc} satisfies the energy relation $P_{in}\kappa^{-1} \sim \frac{1}{2}\epsilon_0|E_{loc}|^2 V_m$. On the other hand the incoming intensity is given by $P_{in}A_{eff}^{-1} = \frac{1}{2}\epsilon_0 c|E_{in}|^2$, thereby leading to an approximate field enhancement factor of $\frac{|E_{loc}|^2}{|E_{in}|^2} \simeq \frac{cA_{eff}}{\kappa V_m}$, and because $g_{v,0} \propto 1/V_m$ we find that $\left(g_{v,0}/\kappa\right)^2 \propto \left|\frac{E_{loc}}{E_{in}}\right|^4$. This expression recovers the accepted electromagnetic enhancement ("E^4 law" [44, 89]) while explicitly showing the contribution of the plasmonic density-of-states at the laser and Stokes (resp. anti-Stokes) frequencies. Because the optomechanical coupling rate is derived from the Raman tensor, our model can be extended to account for all previously studied effects such as (i) the dependence of cross-section on the molecule's spatial orientation, (ii) the selection rules corresponding to different light polarizations, and (iii) the increase in cross-section close to electronic resonances, possibly altered by chemical effects and charge transfers.

The mapping of the optomechanical theory onto the SERS scenario uncovers novel enhancement mechanisms related to backaction between the molecular vibration and the plasmon resonance. This effect leads to a modification of the damping rate of the vibrational mode and in principle also to a shift in the vibrational frequency.

Due to the low thermal occupancy of the vibrational modes, the relevant scattering cross-section from Stokes and anti-Stokes fields must take into account the proper quantum mechanical input noises (2.19)-(2.22) where $\bar{n}_v \approx 0$. As in treatments of optomechanical cooling [77][90], this can be done using the co-variance approach and computing the output spectral density in [photons/(Hz·s)] [29, 91]

$$S^{out}(\omega) \propto \frac{\kappa_{ex}}{2\pi}\left(\frac{\omega^3}{\omega_p^3}\right)\int_{-\infty}^{\infty}d\tau e^{i\omega\tau}\langle\delta\hat{a}^\dagger(\tau)\delta\hat{a}(0)\rangle, \qquad (2.54)$$

where the prefactor in brackets takes into account the frequency dependence of the radiative coupling rate to the far-field of a dipolar emitter [29]. This prefactor is introduced to describe accurately the system in the absence of a cavity where the usual expressions for Stokes and

anti-Stokes scattering and such a frequency dependence are expected [3]. However a general treatment of the cavity case taking into account the frequency dependence of the photonic density of state in free space would be required to legitimate this approach. Alternatively one can approach this problem in a different way by using a more general formalism [31, 33] or by introducing a second high-Q cavity [32, 92] that works as an intermediary between the plasmonic cavity and free space.

Following the complete derivation of the outgoing spectral density presented in Ref. [91] we derive the following expression for the Stokes and anti-Stokes sideband noise spectral density

$$S^{\text{out}}(\omega_S) = \frac{2}{\pi} \frac{\omega_S^3}{\omega_p^3} \frac{\kappa_{\text{ex}}}{\kappa} \frac{A^+}{\Gamma_\nu + \Gamma_{\text{opt}}} \left(\bar{n}_f + 1 \right) \tag{2.55}$$

$$S^{\text{out}}(\omega_{\text{aS}}) = \frac{2}{\pi} \frac{\omega_{\text{aS}}^3}{\omega_p^3} \frac{\kappa_{\text{ex}}}{\kappa} \frac{A^-}{\Gamma_\nu + \Gamma_{\text{opt}}} \bar{n}_f \tag{2.56}$$

with $\bar{n}_f$ the final phonon number in the vibrational mode given by the expression [91]

$$\bar{n}_f = \frac{\Gamma_\nu}{\Gamma_\nu + \Gamma_{\text{opt}}} \bar{n}_{\text{th}} + \frac{A^+}{\Gamma_\nu + \Gamma_{\text{opt}}}. \tag{2.57}$$

where $\bar{n}_{\text{th}} = 1/\left(\exp\left[\hbar\omega_\nu / k_B T_{\text{bath}} \right] - 1 \right)$ for a bath temperature T_{bath} is the mean thermal occupation of the vibrational mode. When pumping the plasmon with blue-detuned light ($\Delta > 0$), the backaction damping rate is negative ($\Gamma_{\text{opt}} < 0$) leading to amplification [59] of the vibrational mode and to an out-of-equilibrium vibrational occupancy.

As the scattering cross section are proportional to the outgoing noise spectral densities integrated over the width of emission of a vibrational sideband ($\tilde{S}^{\text{out}} = \int_{\Gamma_{\nu'}} S^{\text{out}} \, d\omega$) we obtain :

$$\sigma_S^{\text{ba}} \propto \omega_S^3 A^+ \left(\bar{n}_f + 1 \right) \tag{2.58}$$

$$\sigma_{\text{aS}}^{\text{ba}} \propto \omega_{\text{aS}}^3 A^- \bar{n}_f \tag{2.59}$$

and they become power dependent, leading to a superlinear increase of the Raman signal at room temperature for achievable pump intensities. Furthermore, the anti-Stokes/Stokes ratio R becomes "anomalous" under backaction effects, exhibiting values that deviate from the equilibrium Boltzmann factor:

$$R = \frac{\sigma_{\text{aS}}^{\text{ba}}}{\sigma_S^{\text{ba}}} \propto \frac{\omega_{\text{aS}}^3}{\omega_S^3} \frac{A^-}{A^+} \frac{\bar{n}_f}{\bar{n}_f + 1}, \tag{2.60}$$

In principle, a comprehensive characterization of this truly non-classical emission may be performed by appealing to photon-correlation techniques pioneered in quantum optics [93], and later applied to quantum optomechanics [90].

A parametric instability occurs when the amplification rate exceeds the damping rate ($\left| \Gamma_{\text{opt}} \right| >$

Γ_v), corresponding to coherent regenerative oscillations (phonon lasing) [59]. By increasing the quality factor of the plasmonic structure, the threshold is lowered and occurs for a laser detuning closer to the phonon sideband ($\Delta \sim \Omega_v$). Close to this threshold the system exhibits a highly nonlinear response, which could provide a mean for achieving super-resolution in TERS [12] (cf. next section).

Molecular vibrations exhibit anharmonic potentials at higher occupancy (Fig. 2.1c) and inter-mode couplings that cause internal vibrational redistribution (IVR) [94], both of which are not included explicitly in our model. IVR would prevent reaching the threshold for regenerative oscillations of a single mode by introducing additional damping channels, and at the same time could lead to the appearance of a broad Raman background originating from other vibrational or rotational modes indirectly excited [12]. Anharmonicity of the potential, on the other hand, could lead to frequency shifts and broadening of the Raman peak under high amplification (close to threshold). We note that although the reduced damping rate $\Gamma_v + \Gamma_{opt}$ should manifest as a reduced linewidth of the vibrational mode, this signature could be masked by both IVR and anharmonicity. Observation of the optical spring effect (a shift in the frequency of the vibration associated with the in-phase response of the force F_P) would also be difficult with molecules.

2.2.1 Impact of the nonlinear amplification mechanism on experimental observations

We end this chapter by presenting some of the effects that would be encountered for a system close to the parametric instability threshold or in other words when the dynamical backaction mechanism introduced by our coherent coupling is large and $\Gamma_{opt} \simeq \Gamma_v$. It should be noted that pure dephasing of molecular vibrations (> 10 ps, as estimated from the Raman linewidth) should not prevent the coherent coupling that we introduced as the plasmon lifetime in the cavity (< 0.1 ps) is much faster

In the dynamical backaction regime, the anti-Stokes/Stokes ratio calculated previously become anomalously large. The deviation from the equilibrium Boltzmann factor is demonstrated in Fig. 2.3. The signature of dynamical backaction amplification can be experimentally distinguished from thermal effects such as local heating by (i) the sharp sensitivity of the anomaly on the laser detuning from the plasmon; and (ii) its non-linear power dependence (see Fig. 2.4).

We explore this nonlinear power dependence close to the threshold in Fig. 2.4 and illustrate how our model could lead to super-resolution SERS/TERS imaging similar to what has been observed in recent experiments [12, 55] The sub-nanometer resolution achieved have spurred excitement and debates over the physical mechanism leading to the observed super-resolution. Since the plasmonic hot-spot lateral size at the tip apex cannot be smaller than ~ 10 nm strong nonlinear effects should be involved.
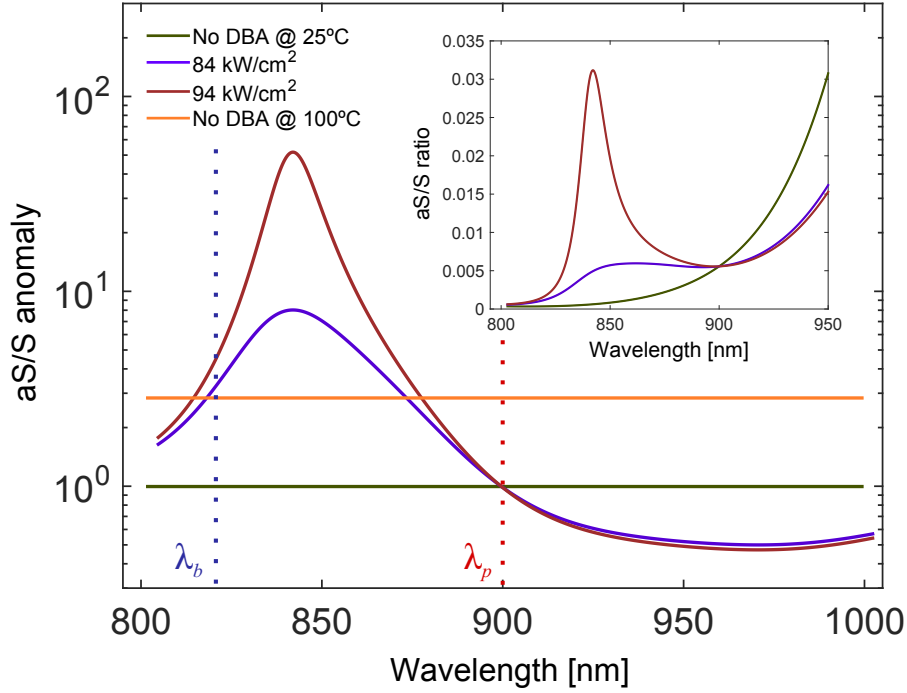
Figure 2.3 – **Anomalous anti-Stokes/Stokes ratio under dynamical backaction amplification.** The anti-Stokes/Stokes (aS/S) anomaly is defined as the aS/S ratio $R = \sigma_{aS}^{ba}/\sigma_{S}^{ba}$, Eq. (2.60), divided by its value under negligible dynamical backaction (DBA) amplification, $\sigma_{aS}^{em}/\sigma_{S}^{em}$, for a vibrational mode in thermal equilibrium at room-temperature (No BA @ 25°C). λ_p is the plasmonic resonance wavelength while λ_b denotes the blue phonon sideband. For comparison we also plot the aS/S ratio when the molecules are heated by the laser to 100°C (orange line) assuming that absorption is wavelength independent. The inset shows the original aS/S ratio R before normalization, as expressed in Eq. (2.60), for the three pump intensities considered in the main figure. Even without backaction, the ratio depends on the laser detuning from the plasmon due to selective enhancement of either Stokes or anti-Stokes outgoing wavelengths.

Figure 2.4 – **Super-resolution in TERS** Computed Stokes scattering intensity as a function of lateral position assuming a point-source scatterer located at the origin and a Gaussian plasmonic field distribution of 10 nm full-width at half maximum. Close to the instability threshold (green curve) the pronounced nonlinearity of the response leads to a sharp increase in spatial resolution.

3 Optically probing self-assembled plasmonic nanojunctions
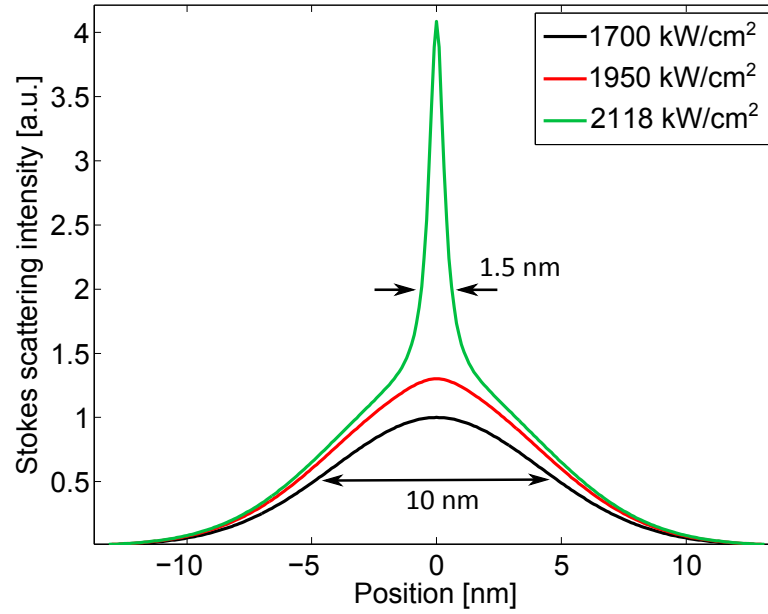
3.1 Detection of nanoparticle on a mirror system

3.1.1 Sample fabrication

The plasmonic nanojunctions were fabricated within the group of Christophe Galland following a 3-step process: (1) fabrication of patterned metal films or micro-plates growth, (2) deposition of a molecular monolayer (spacer) on the metal film, (3) drop-casting of metal nanoparticles on the spacer-film. We focus in the thesis on the samples fabricated according to the following procedure but it has to be noted that we tested satisfactorily extended versions of this process in order for example to add to the monolayer an ALD layer or to replace it by 2D materials. We also replaced the polyhedral gold nanoparticles with gold nanocubes and encapsulated some nanojunctions with ALD layers (cf. Fig 3.1a).

Metal film fabrication : 2 types of metal films were prepared: For the template stripped Au film (TS) we fabricate first a patterned template by standard photolithography. Then a 200 nm thick gold film is evaporated on the template using electron beam evaporation at a rate of 0.5 nm/s. Next, the Au surface is glued with pieces of ~1 mm^2 glass using an optical adhesive (NOA61), cured by UV light. The template is then peeled off, revealing an ultrasmooth Au surface[95] whith subnanometer RMS roughness (Fig 3.1b). The lithographic mask produces a grid of markers (visible both in bright and dark-field microscopy) on the TS film which enable an unambiguous localization of the nanostructures (Fig 3.1c).

Au micro-pates (MP) are synthesized by the method described in Ref. [96]. Briefly, 6 mL ethylene glycol (Sigma-Aldrich) is put into a 100 mL flask in a 150 °C oil bath. Then a 1 mL 0.2 M gold(III) chloride hydrate (HAuCl$_4$, Sigma-Aldrich) water solution is injected into the flask. Next, a 3 mL ethylene glycol solution containing 0.7 g of dissolved polyvinylpyrrolidone (PVP, Mw = 40000, Sigma-Aldrich) is dropped into the flask. The reaction finishes after ~30 min. The AuMPs are then cleaned by acetone and ethanol solutions before storage in ethanol. Their average lateral size and thickness are 40 ~m and 100 nm.
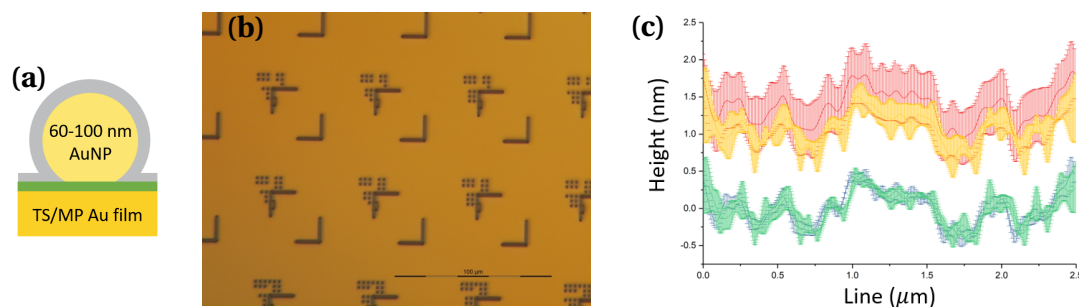
Figure 3.1 – **(a)** Sketch of a generic nanojunction. **(b)** AFM measurements of the flatness of one representative template-stripped gold film fabricated in the group of Christophe Galland. Red and yellow areas shows the mean height variation on a 2.5x2.5 μm surface along one line. The green (blue) curve shows the average subtracted height variation obtained from the data depicted in yellow (red). **(c)** Bright-field image of a patterned region of one fabricated TS film. Original picture reproduced with the courtesy of A. Ahmed.

Spacer fabrication : We obtain a self-assembled monolayer (SAM) of BPT molecules on the metal films (~1 nm average thickness) by immersion of the metal films in a BPT ethanol solution. For TS films, we use a 1 mM BPT ethanol solution for 2 hours of incubation at room temperature.

For MPs, the solution is firstly drop-casted on an Si wafer and dried by nitrogen gas. Then the sample is immersed in a high concentration (0.1 M) BPT solution at 70 °C for 24 hours. This ensures the replacement of the PVP ligands on the AuMP surface. After incubation, the samples are all rinsed with ethanol and water to remove the extra BPT molecules and dried by nitrogen gas.

Nanoparticle synthesis and drop-casting : We chose 2 type of commercially available nanoparticles to build up our plasmonic nanojunctions: (1) 'Polyhedral' gold nanoparticle (NP) (purchased from BBI solutions, citrated capped), (2) 'Spherical' gold nanoparticles (citrated capped) with smaller facet sizes (purchased from Expedeon, citrated capped).

An aqueous solution of AuNPs (BBI solutions) with original concentration resulting in an optical density of 0.88 at 520 nm is mixed with an aqueous solution of sodium citrate tribasic dihydrate and an ethanol solution of BPT (0.1 mM) in order to remove the citrate layer and replace it with a monolayer BPT coverage. After 2 hours of incubation, the products are centrifuged at 12000 rpm and stored in water.

AuNP are next deposited on various spacer-film systems by drop-casting. The droplet remains in contact with the film for a time interval ranging between 30 and 300 s depending on the colloid concentration and the surface hydrophobicity. The residuals are finally removed by a delicate rinsing and drying of the sample with water and nitrogen gas.
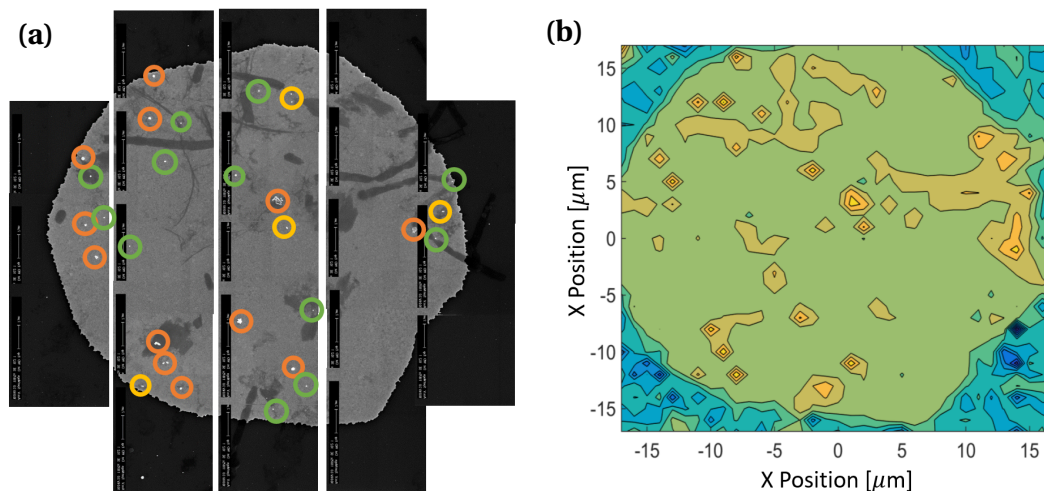
Figure 3.2 – **(a)** SEM collection of maps representing one specific region of a sample that was exposed to a highly concentrated NP solution. The green circles show single NPOM structures while yellow and orange circles show respectively dimers and aggregate structures. **(b)** Corresponding photoluminescence color map obtained under 532 nm excitation.

3.1.2 Identification of single nanostructures

One widely use option to detect and characterize the optical properties of these self-assembled nanostructures relies on the scattering properties of the nanostructure. The structures are side-illuminated with a reference incoherent light source and the scattered light is collected by another objective avoiding the large specular light reflected on the Au film. In addition to a characterization setup where the nanoparticles can be identified with such a dark-field setup we constructed a fully motorized setup enabling dual-tone illumination of our structures (cf. D). The first tone can be tuned from 700-800 nm and is used to collect both motional (Raman) sidebands created by the modulation of the incoming tone by the vibrational modes constituting the spacer of the nanojunction. The second tone at 532 nm is used to characterize the plasmonic modes and monitor their evolution during the measurements. The mechanism behind the light emitted by a metallic nanostructure (known as photoluminescence) when excited by different laser tones has been investigated intensively in the last years and its understanding is still a matter of debate [97–100]. We should come back to some fundamental aspects of this emission in the following chapter

From an experimental point of view both these illuminations can be controlled in a similar fashion and along the same path as the rejection of the specular light created by both tones on the Au film can efficiently be performed in the spectral domain.

Fig. 3.2 illustrates the diversity of structures that can appear during self-assembled fabrication. For this figure, multiple electron microscopy acquisitions were assembled after an optical

30x30 μm scan in order to evaluate the PL measurements. First, it can be seen that the luminescence of the gold film itself can be identified as evidenced earlier [101]. In addition, many single structures can be recognized directly from the PL integrated intensity [102, 103]. With the help of their spectral profile, the single structures can be further filtered from other types of assemblies and the different modes parameters extracted from the photoluminescence signals resulting from a 532 nm excitation.

3.1.3 Photoluminescence of gold nanostructures

The intensity and spectral distribution of the luminescence of a specific structure depends not simply on its scattering properties (as for a dark field scheme) but on several other factors that can be divided in a first approach in three different classes : the optical absorption of the nanostructure, the joint density of state of the material and the local photonic density of state of the nanostructure. We should not intend to give a complete picture of the photluminescence process but will follow the phenomenological approach used in Ref. [104] to shortly describe a few aspects relevant for our observations. The interested reader can find more exhaustive approaches in other studies [100, 103].

Here we consider the luminescence to be the radiative recombination of optically created electron-hole pairs, after their interaction with thermal baths. The plasmonic resonances may affect both the absorption and the emission part of the process. Because of the interactions with a bath (thermally excited elctrons and holes or lattice phonons) the emission covers a large spectral range limited by $\hbar\omega_L \pm k_B T$. In addition we will consider here a single plasmonic mode that will assist the emission part of the PL process. Its resonance frequency is considered to be far below the electronic transitions of gold so that the electronic density of states can be considered as constant.

Then we can isolate two different behaviour depending on the detuning between the laser frequency and the plasmonic cavity. If the laser excitation is well above the resonance of the plasmonic resonance, the emission in the plasmonic mode range is not modified by the thermal population of the bath and the intensity of the PL signal at ω is simply given by the plasmon-assisted channel

$$I_{\mathrm{PL}}(\omega) = I_{\mathrm{spr}}(\omega) \propto \mathrm{LDOS}_{\mathrm{spr}}(\omega) \tag{3.1}$$

where the last term is the local density of states of the plasmonic mode. In this case, the parameters of the plasmonic mode can be extracted directly from the spectral distribution of the generated PL signal.

In the other case, for a laser frequency located within the plasmonic resonance, both Stokes and anti-Stokes plasmon-assisted channels exist and are differently modified by the bath population. When operating in a frequency range sufficiently distant from the excitation frequency a simple Boltzmann statistics can describe the bath population $\bar{n}_{\mathrm{B}}(\delta\omega) = \exp\left(\frac{\hbar\delta\omega}{k_B T}\right)$
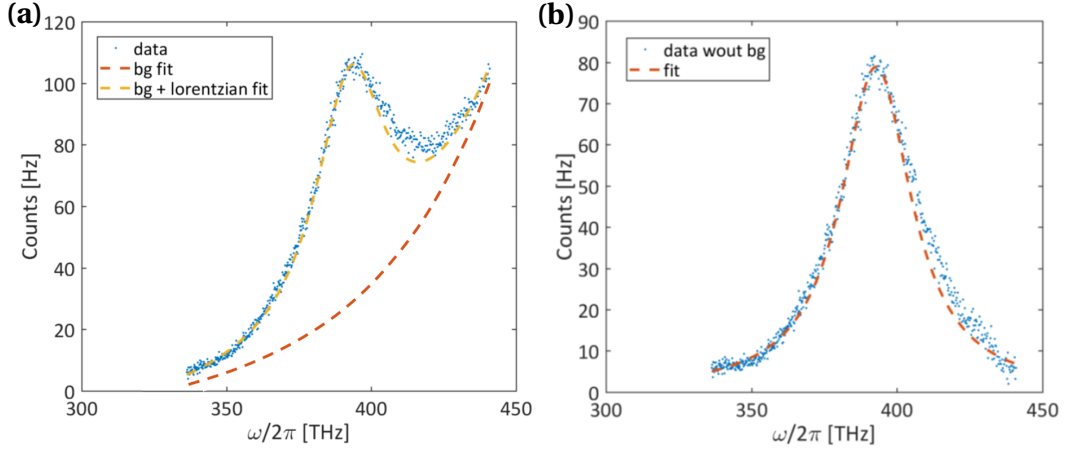
Figure 3.3 – **(a)** Stokes PL counts generated by a single nanojunction under 532 nm (564 THz) excitation (blue dots). A numerical approximation of the background (red dashed line) and the total luminescence attributed to the background and one plasmonic mode (yellow dashed line) are also depicted. **(b)** Corresponding background subtracted PL of a singe nanojunction mode (blue dots) fitted by a single Lorentzian distribution (red dashed line) with the following parameters : $\omega_p = 394$ THz ($\lambda_p = 761$ nm) and $Q = 13$.

with $\delta\omega = \omega - \omega_L$ so that both PL sidebands intensities are described by :

$$I_{\text{PL}}^{\text{S}}(\omega) \quad \propto \quad I_{\text{spr}}(\omega)\,(\bar{n}_{\text{B}}(\delta\omega) + 1) \tag{3.2}$$

$$I_{\text{PL}}^{\text{aS}}(\omega) \quad \propto \quad I_{\text{spr}}(\omega)\,\bar{n}_{\text{B}}(\delta\omega) \tag{3.3}$$

The collection of these signals enable thus the knowledge of the plasmonic profile and the extraction of an effective temperature associated to the bath seen by the electron-hole pairs before recombination inside the metallic structure. It should be noted that the Boltzmann statistics used here is a good approximation of both Fermi-Dirac and Bose-Einstein statistics for large $\delta\omega$. The physical statistics behind this process is still a matter of debate in the community as the nature of the relevant bath (gold lattice, electronic bath) remains unclear. A careful study of the anti-Stokes PL close to the laser frequency could help to advance on this question.

Following the description of the Stokes luminescence, the spectra of selected nanojunctions can be well-approximated by a sum of single Lorentzians on top of a background constituted by the film luminescence. In Chapter 4 we illustrate such a multi-mode fitting of the different antenna modes of a nanojunction via their modification of the local density of states of the Au film, i.e. $\text{PL}_{\text{NP}}/\text{PL}_{\text{SUB}}$.

In Fig. 3.3 we highlight an alternative treatment where a single mode spectral range is considered. In this case the background (constituted indistinctively of higher frequency modes
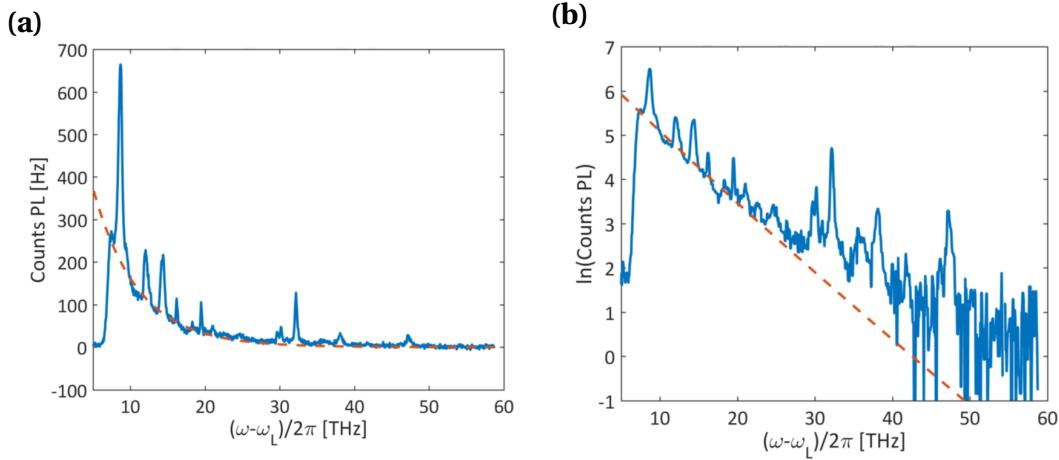
Figure 3.4 – **(a)** Anti-Stokes Raman and PL counts generated by a single nanojunction under 750 nm excitation (blue line) as a function of the frequency shift of the signal with respect to the laser tone. **(b)** Natural logarithm value of the counts depicted in **(a)**. The Raman lines are identified and extracted before fitting the background. The fitting window used here goes from 7.5 to 20 THz shift. The resulting fit is represented by a red dashed line on both subfigures.

and of the film luminescences) can be numerically approximated so that the single mode luminescence can be isolated. The parameters of the nanojunction plasmonic mode can then be extracted from a single Lorentzian fit.

Similarly the anti-Stokes residual luminescence appearing in the Raman measurements can also be described in first approximation by an exponential distribution described earlier in this section (cf. Fig. 3.4). The extraction of an electronic temperature from the exponential coefficient and the observed discrepancy between the exponential fit and the signals observed at large Raman shifts will be discussed at the end of this chapter.

On the excitation part, the impact of the plasmonic assisted channel can be recognized by using different excitation wavelengths on a single structure. Alike previous studies [101, 105] we use two lasers driving the interband transition to evaluate their relative efficiencies. From the film photoluminescence (Fig. 3.5a) it can be seen that the 488 nm excitation leads to higher PL yield than a 532 nm excitation over the full spectral range. It should be noted that the lower wavelength tail of the luminescence spectra varies substantially from one spot to another on the film evidencing defects of the film itself. These variations do not however impact substantially the region where the plasmonic modes we are interested in are located.

On the contrary the raw data of the luminescence obtained over a nanoparticle (Fig. 3.5b) are highlighting similar emission profiles for both illuminations (evidencing the role of the antenna mode on the emission side) and a higher enhancement factor for the 532 illumination resulting from a better coupling of the excitation beam to the longitudinal plasmonic mode of
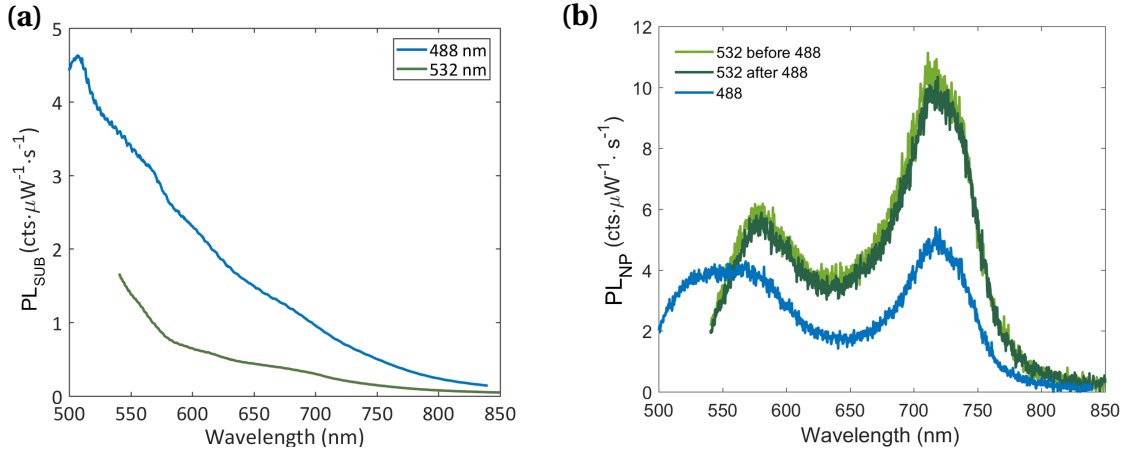
Figure 3.5 – Comparison of the photoluminescence arising from 488 nm (blue line) and 532 nm (green lines) illuminations of a bare template-stripped film of gold **(a)** and of a single nanojunction **(b)**.

the nanoparticle.

3.2 Polarization based study of the nanojunction

The study of the laser excitation on the light emission processes of the nanojunction can be further studied through careful preparation of higher order modes of the laser tone. Patterned field of lights, for example, have been used in the past to improve the localization and characterization of nanoscale emitters [106–108].

Nowadays commercial liquid crystal devices are facilitating the generation of such polarized states. We used a radial-polarization device from ArcOptix [1] to prepare both incoming beams of our experimental setup and study the dependence of the photoluminescence and Raman signals on the polarization state of the exciting field.

For both optical paths some polarization components are modified by other optical components after the creation of the spatially polarized beam. For that reason, we simulated the fields distributions of both radial and azimuthal incoming beams inside the focal plane taking into account the effect of the imbalance between the two higher order components of the beam, via the introduction of an imbalance ratio (cf. Sec. C.2).

3.2.1 Excitation of the PL process

Fig. 3.7 shows the results of two scans of the focal spot using the nanoparticle to probe the focal field. The use of two differently polarized beams enable to identify the components

---

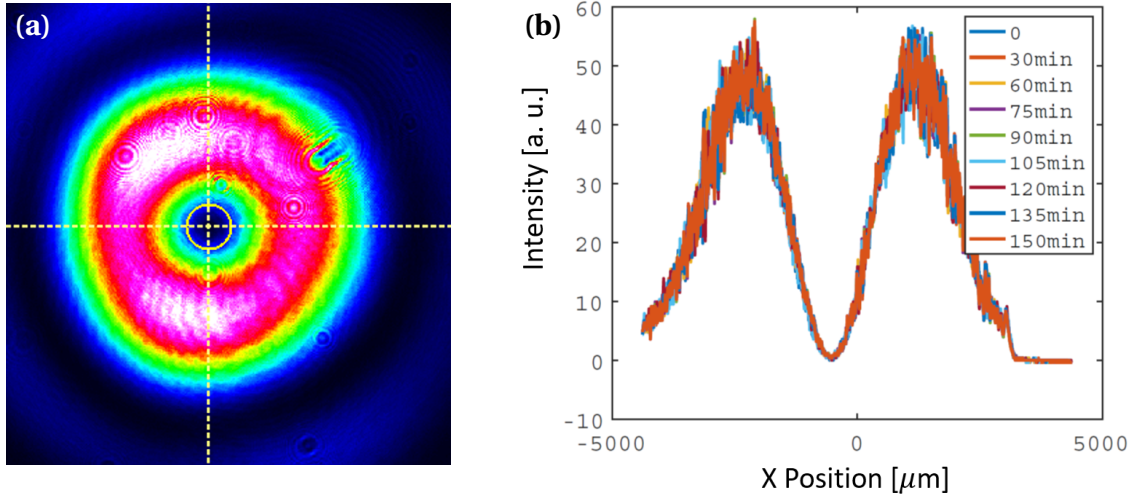[1] http://www.arcoptix.com/radial_polarization_converter.htm

Figure 3.6 – **(a)** Intensity distribution of the electric field of a collimated radially polarized propagating beam at a wavelength of 750 nm. **(b)** Projection on the x-axis of the intensity distribution at different moments in time. The 2D image and its projection on one axis have been obtained with a CCD camera beam profiler (Thorlabs).

that are coupled to the nanoparticle by comparing the PL integrated intensity maps with the numerically calculated field distributions of specific components. The simulation are rescaled and rotated to match the incoming polarization of the experimental beam. The distributions evidence the coupling of the in-plane components of the field with similar resulting intensities and spectral profiles of the nanojunction mode(not shown here). These results reinforce the observation made in the previous section and based on the PL yield, demonstrating that the 532 nm excited PL is assisted by the transversal plasmonic resonance of the nanoparticle.

3.2.2 Excitation of the Raman process

Other studies already employed radially polarized beam to couple to one specific mode of the cavity [109] or to allegedly increase the signal collected on the Raman sidebands [110].

Fig. 3.8 shows again the results of two scans of the focal spot using the nanoparticle to probe the focal field. This time the comparison is performed on the signals integrated over one Raman line. The single lobe profile obtained with the radially polarized excitation evidences the coupling of the out-of-plane component of the field and suggest thus a coupling to the antenna mode (L01) of the nanojunction. Remarkably the azimuthally polarized beam shows a different pattern while maintaining an equivalent level of intensity (within a factor 3). The two lobes distribution in addition to the comparable level of resulting Raman intensities at their respective maxima identifies a coupling to the in-plane component of the incoming azimuthal field. The fact that the antenna mode cannot couple efficiently to such an optical field indicates
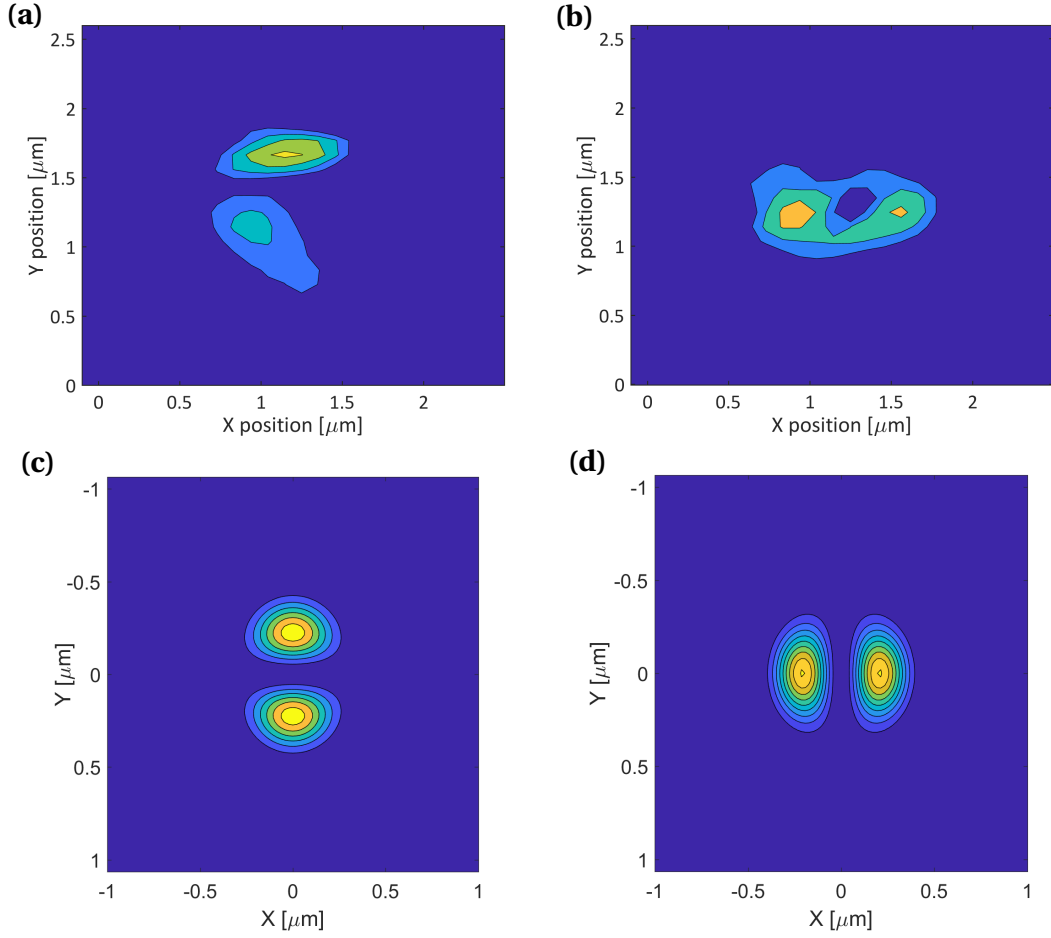
Figure 3.7 – Normalized level of integrated PL counts collected from a TS-BPT-NP structure for an incoming radially **(a)** and azimuthally **(b)** polarized beam as a function of the nanojunction position inside the focal plane. Simulations of the distributions of the radial component ($|E_\rho|^2$) of a radially polarized beam **(c)** and for an azimuthally polarized beam **(d)** into focus. The parameters of the illumination are as follows : air-immersed objective (NA=0.95, 50x), unity filling factor, wavelength of 532 nm and polarization imbalance ratio of 100.

a coupling to a gap mode (S11) that couples well to an in-plane field component [37] and evidences the modal selectivity of such a polarization scheme. The fact that one axis seems to be favorized in the experimental data indicates most probably the additional contribution of a polarizing element in the optical path (excitation or collection) not taken into account in the simulations. The shift between the two experimentally observed central position of the field distributions is due to a drift of the stage in between the two measurements.

Finally, Fig. 3.9 shows the contrast between the two Raman spectra obtained with a radially and azimuthally polarized excitation at the sample position where the signal arising from a radial illumination is maximal. As expected from the field distribution if the two beams in the focal plane their contrast is important but the Raman modes relative intensities are similar. As
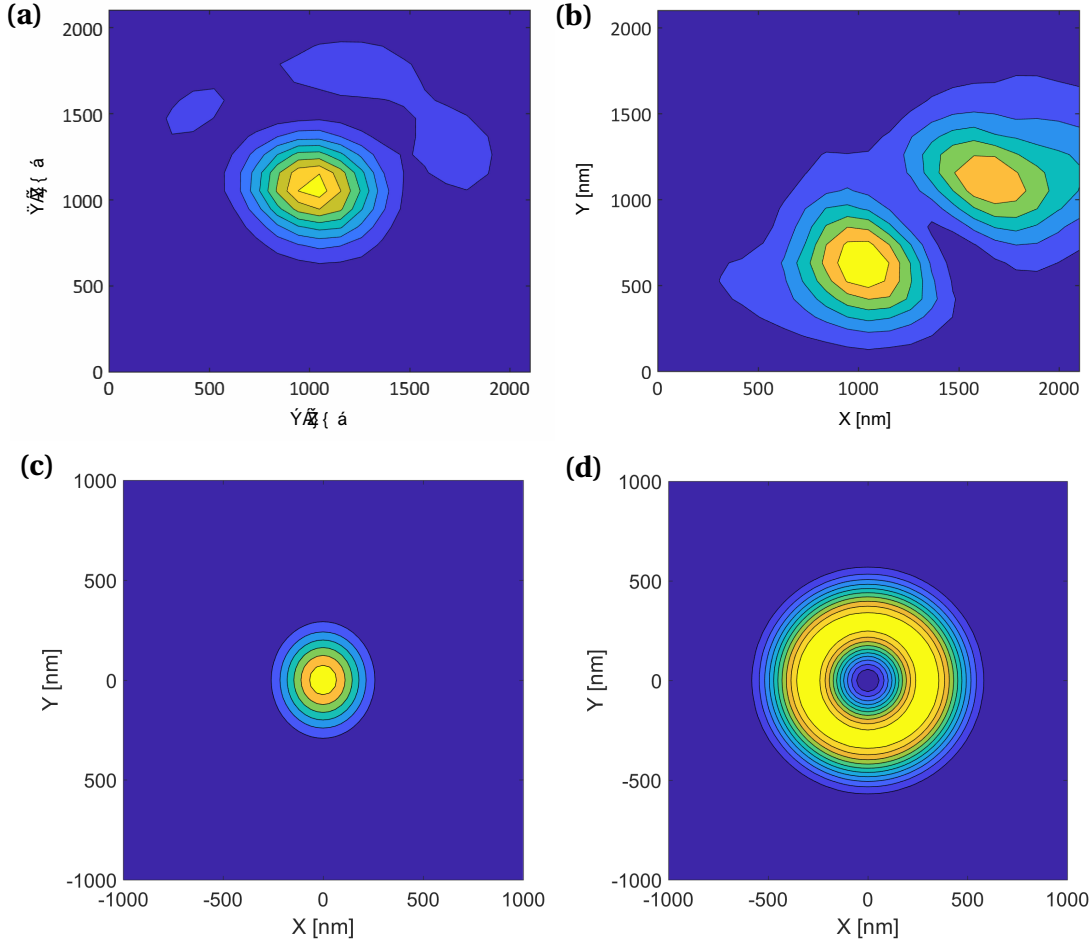
Figure 3.8 – Normalized level of counts integrated over one collected Raman band of a TS-BPT-NP structure for an incoming radially **(a)** and azimuthally **(b)** polarized beam as a function of the nanojunction position inside the focal plane. **(c)** Simulation of the distribution of the $|E_z|^2$ component for a radially polarized beam into focus. **(d)** Simulation of the distribution of the $|E_\rho|^2$ component for an azimuthally polarized beam into focus. The parameters of the illumination are as follows : air-immersed objective (NA=0.95, 50x), unity filling factor, wavelength of 750 nm and polarization imbalance ratio of 1.5 (cf. Sec. C.2). The intensity is normalized both in the simulation and experiment.

a side remark we use this tool in addition to dark-field and photoluminescence techniques to verify that our nanostructures are indeed active single nanoparticle on mirror.

3.3 Sideband thermometry of the vibrational mode

As described in Chapter 2 it would be interesting to increase the power reaching the nanocavity and coupled to the mode of interest in order to observe the dynamics of both electronic and vibrational degrees of freedom of the nanojunction. One preliminary word should be devoted
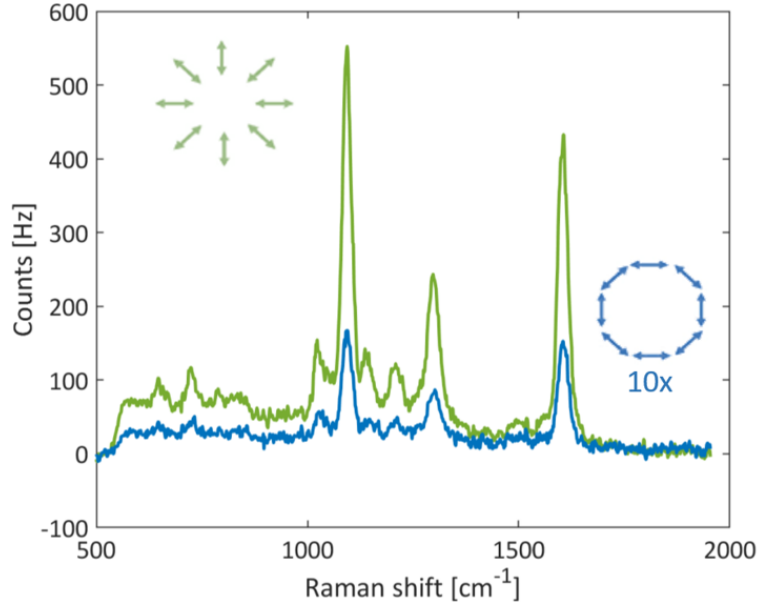
Figure 3.9 – Raman spectra of the NPOM structure illuminated by two patterned beams (radial-green, azimuthal-blue) for a nanostructure positioned so that the Raman signal under radially polarized excitation is maximal. The signal collected from the incoming azimuthal beam is amplified 10x for better comparison.

to the ability of such structures to handle higher level of powers.

Fig. 3.10(a) evidences how successive laser illuminations of a specific nanojunction is impacting its mode profiles, their resonance position and quality factors. Several aspects related to morphological changes of the metallic structure have been evidenced in previous studies [111, 112], and our current data tend to show modifications of the facet size. Not only the plasmonic structure is subject to modifications but depending on the specific nanojunction assembled the spacer might also degrade. A careful study of these optically induced modifications for different nanojunctions and their dependence not only on the laser detuning and power is currently performed within the group.

In the following we will thus focus on a power regime and on nanojunctions that showed good stability to study the dynamics of the system under optical excitation over a dynamic range of 20 dB; limited by morphological changes on the upper end of the range and by the visibility of the anti-Stokes sideband on the lower end.

3.3.1 Power sweeps with radial and azimuthal polarization

In order to probe the population of a specific vibrational mode and test the model developed in Chapter 2, we recorded simultaneously the Stokes and anti-Stokes sidebands of many
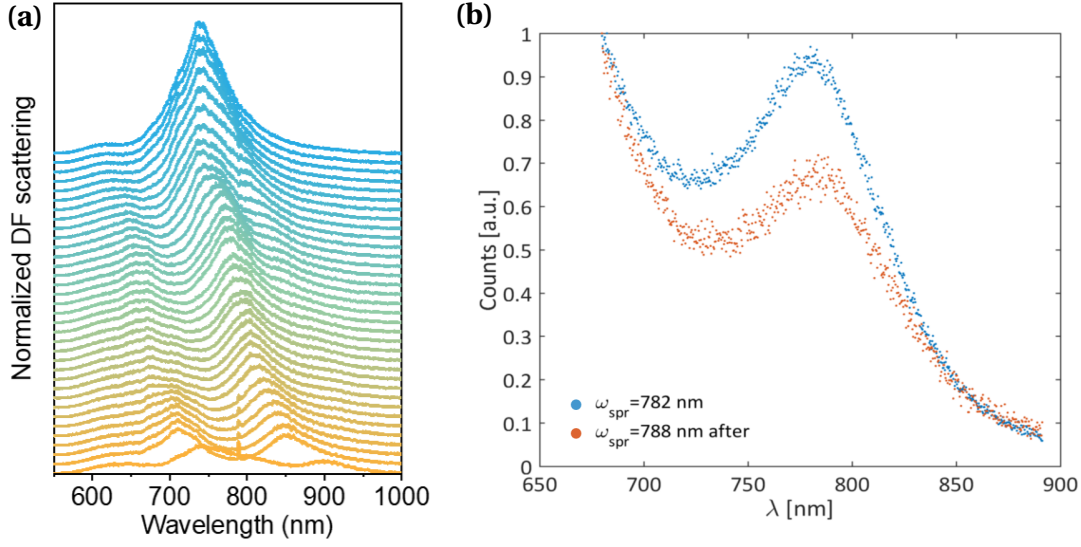
Figure 3.10 – Examples of power handling of two different nanojunctions **(a)** Laser induced damage of the plasmonic resonance with time. The original dark-field response of the nanostructure is in blue at the top. In between each dark-field acquisition the nanostructure is exposed to a laser illumination close to its resonance. A vertical shift is applied to each successive spectrum for better readability. These dark-field measurements have been performed in the laboratory of C. Galland by W. Chen. **(b)** PL spectra showing the change in resonance frequency and quality factor of one plasmonic mode of a nanojunction before (blue dots) and after (red dots) a complete set of measurements similar to the ones detailed in later in this section.

different self-assembled nanojunctions. From their ratio we could extract the modification of their effective temperature ΔT_v starting from the following expression :

$$R \propto \frac{\omega_{\mathrm{aS}}^3}{\omega_{\mathrm{S}}^3} \frac{A^-}{A^+} \frac{\bar{n}_f}{\bar{n}_f + 1} \frac{D(\omega_{\mathrm{aS}})}{D(\omega_{\mathrm{S}})}, \tag{3.4}$$

with $D(\omega)$ the optical response of the setup at the frequency $\omega/(2\pi)$.

And, from the background of the anti-Stokes sideband, we could obtain ΔT_e :

$$I_{\mathrm{PL}}^{\mathrm{aS}}(\omega) \propto I_{\mathrm{spr}}(\omega)\, \bar{n}_B\,(\delta\omega)\, D(\omega). \tag{3.5}$$

It should be noted that we extract temperature variations to remove the dependence of our signals on the setup response and on the plasmonic resonances.

Here we present the results of power sweeps on three representative cases. As the optomechanical interaction depends on the detuning we tested both blue- and red-detuned configurations and interrogated different modes via their preferential coupling to either a radially or an azimuthally polarized excitation.

Variation of vibrational temperatures were observed for many systems. Also, systems excited above a threshold power showed irregular emergence of additional Raman lines and anomalous vibrational temperatures similar to observations reported in other studies [20, 113] (cf. Appendix E). For the permanent Raman lines monitored here, the mechanism behind the limited increase of temperature could well be explained by the corresponding increase of the effective electronic temperature ΔT_e obtained via the photoluminescence signal. In opposition to other studies where the optomechanical coupling was instrumental to present several observations [20, 114], our measurements indicate a more important contribution from heating than from any other mechanism in the observed modal occupational level inside our nanojunctions. Additional numerical calculations could be performed and a completed model could be developed to include heating induced by laser absorption in our model and derive the additional optical power dependence of these temperatures.

A blue detuned case with radial and azimuthal polarizations

Figure 3.11 – Raw spectrum collected from the excitation of a TSAu-BPT-AuNP nanojunction (80 nm particle size) with a linearly polarized 532 nm incident beam at a power of 100μW on the sample and for 3 s acquisition.

Figure 3.12 – Variations of electronic (red dots) and vibrational (blue dots) temperatures as a function of incoming power at the sample of a radially **(a)** and azimuthally **(b)** polarized laser beam at 750 nm. Each dot represents the result of an accumulated acquisition for which the exposure time has been adjusted in order to optimize the signal statistics.
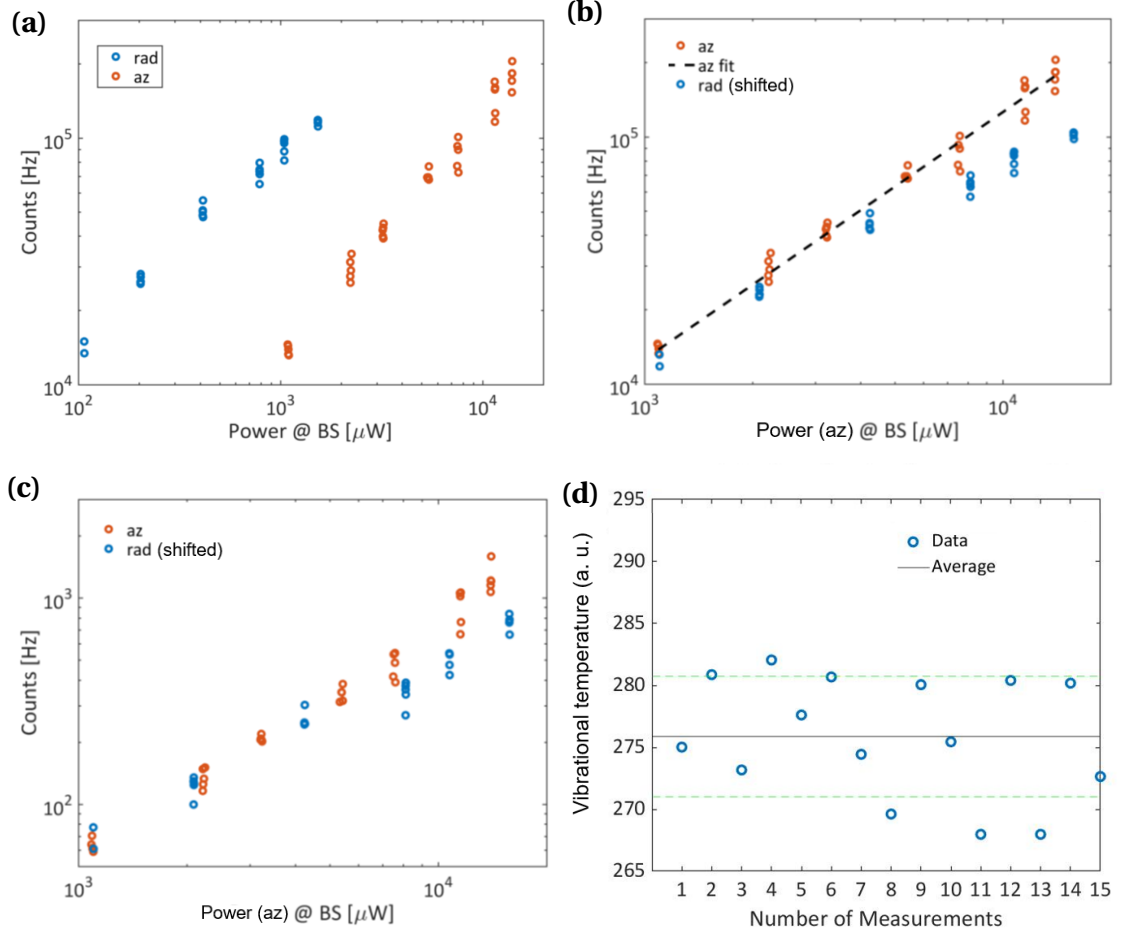
Figure 3.13 – **(a)** Counts integrated over the Stokes sideband of the BPT vibrational mode $\nu = 1070\ \mathrm{cm}^{-1}$ for the same TSAu-BPT-AuNP nanojunction in function of the laser power as monitored by a powermeter before entering the microscope (cf. Appendix D). **(b)** The two sets of data presented in **(a)** are superimposed (horizontal shift of the radially polarized data) to allow a better comparison of the power dependence of both signals. The fit of the azimuthal data shows an exponential coefficient of 0.98. **(c)** Counts integrated over the anti-Stokes sideband and acquired simultaneously. The two sets of data are superimposed (horizontal shift of the radially polarized data) to allow a better comparison of the power dependence of both signals. **(d)** Stability of the motional sideband thermometry measurements (blue dots) for a sequence of acquisitions and an incoming power of $100\mu W$ with radial polarization. Similar stability can be observed under azimuthal illumination (not shown). This automated sequence optimizes the Stokes signal with respect to a radially polarized beam by readjusting the sample position in between each accumulated acquisition. The average value (black line) is uncalibrated and the standard deviation is around 5 K (interval delimited by green dashed lines). The laser tone at 750 nm is radially (blue dots) or azimuthally (red dots) polarized. Each dot represents the result of an accumulated acquisition for which the exposure time has been adjusted in order to optimize the signal statistics.
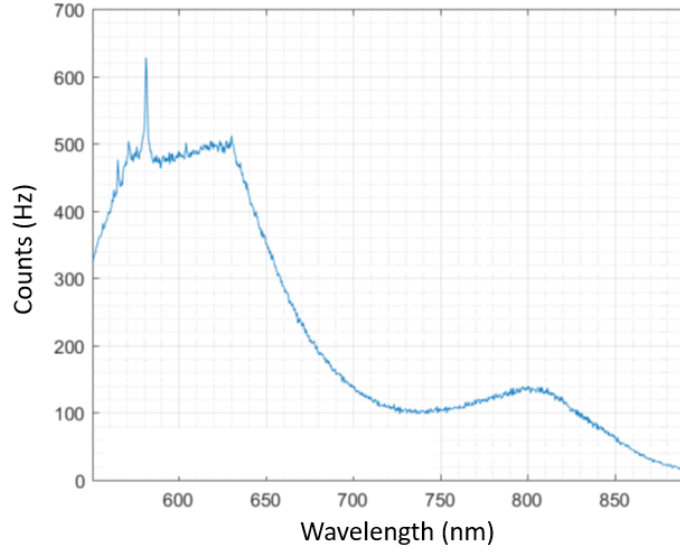
A second blue detuned case
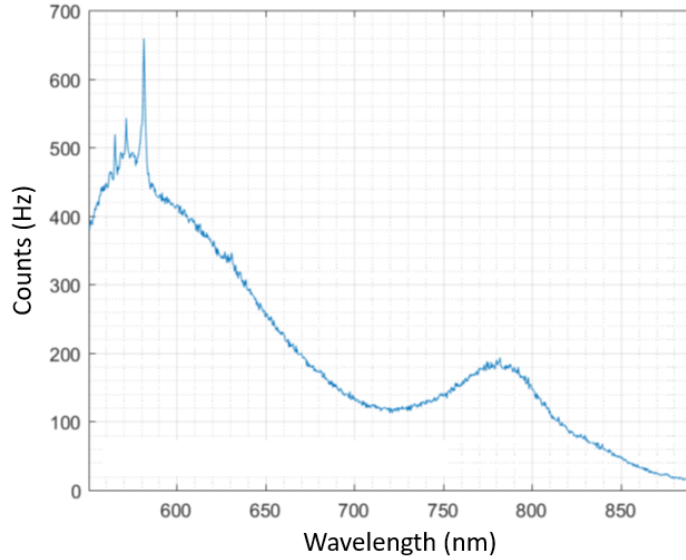
Figure 3.14 – Raw spectrum collected from the excitation of a TSAu-BPT-AuNP nanojunction (80 nm particle size) with a linearly polarized 532 nm incident beam at a power of 100μW on the sample and for 3 s acquisition.
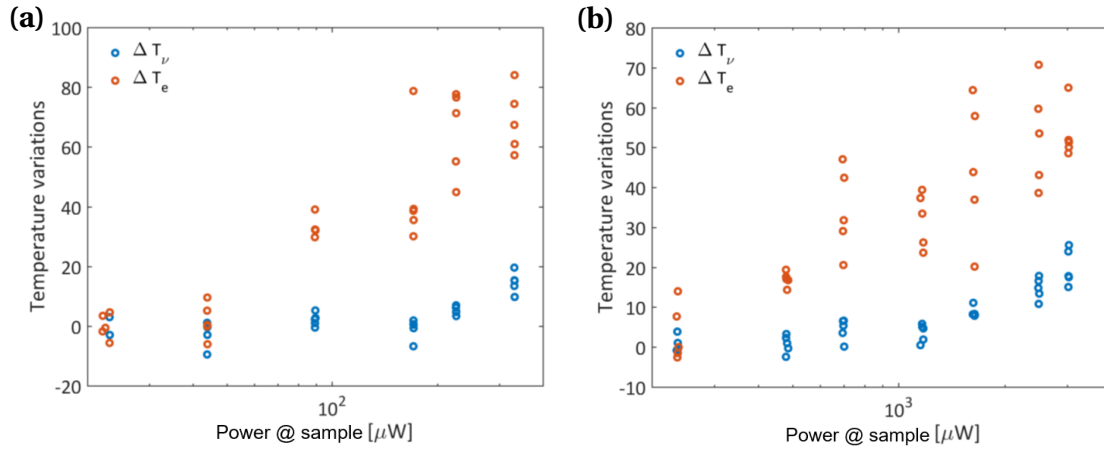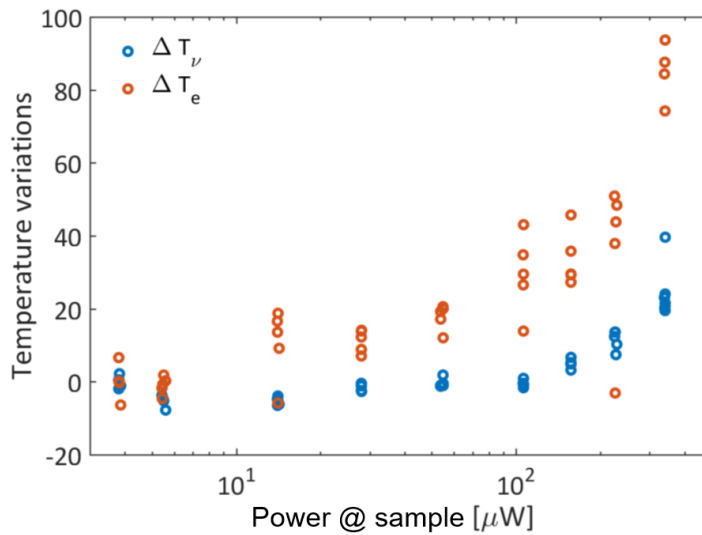

Figure 3.15 – Variations of electronic (red dots) and vibrational (blue dots) temperatures as a function of incoming power at the sample of a radially polarized laser beam at 750 nm, blue-detuned from the antenna mode plasmonic resonance. Each dot represents the result of an accumulated acquisition for which the exposure time has been adjusted in order to optimize the signal statistics.

A red detuned case
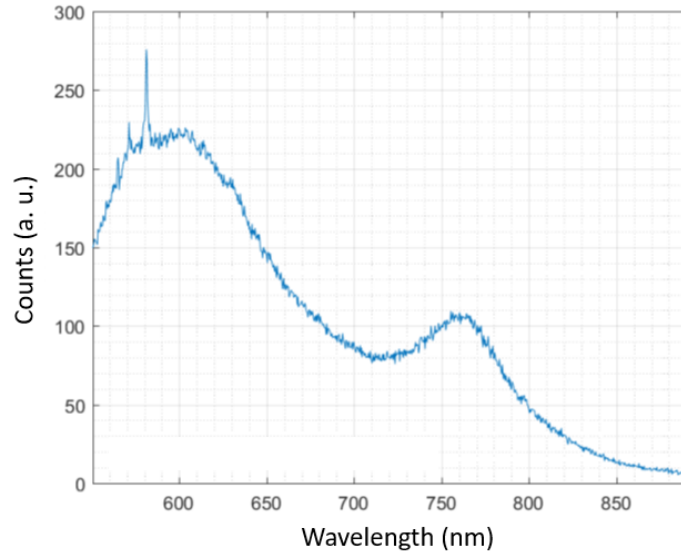
Figure 3.16 – Raw spectra collected from the excitation of a TSAu-BPT-AuNP nanojunction (80 nm particle size) with a linearly polarized 532 nm incident beam at a power of 100μW on the sample and for 3 s acquisition.
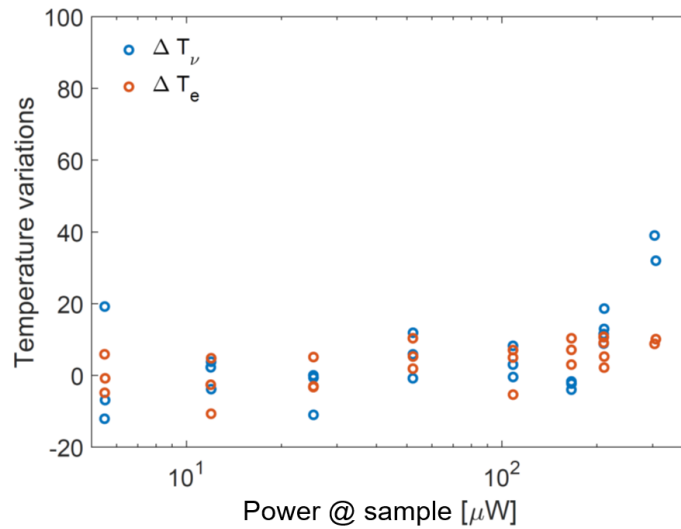
Figure 3.17 – Variations of electronic (red dots) and vibrational (blue dots) temperatures as a function of incoming power at the sample of a radially polarized laser beam at 790 nm, red-detuned from the antenna mode plasmonic resonance. Each dot represents the result of four acquisitions for which the exposure time has been adjusted in order to optimize the signal statistics.

3.3.2   Perspectives on self-calibrated temperature measurements and Outlook

All the temperature measurements (vibrational and electronic) shown are variations measurements. The retrieval of an absolute temperature for such systems usually require some complex calibration process in order to be accurate (calibration of the optical response of the setup over a wide spectral range, knowledge of the LDOS of the full nanostructure on the same spectral range). One other option that we are currently investigating consist in the simple addition of a PID stabilized hot-plate to the sample holder in order to calibrate at the same time both the electronic and vibrational temperature in the nanojunction and interrogate their sensitivity on the environmental temperature.

In order to explore higher power regimes and possibly witness the regime of amplification described in Chapter 2 designs that mitigate the residual heat created by the laser should be investigated. For example careful choice of substrates [115], ALD coverage [116, 117][6,10] or the use of inverted designs (where the positions of metal and air/dielectric are interchanged) [118] have proven to significantly reduce heating effects in gap antennae structures. Alternatively, an additional optomechanical scheme is developed in Chapter 5 in which the signal of interest does not compete in the same way with heating mechanisms.

4 Study of the intrinsic light emission of nanojunctions

As evidenced in the last chapter, unleashing the full potential of plasmonic nanojunctions as a universal platform to engineer light-matter interaction at the nanoscale still faces a gap in our capability to understand and control atomic scale dynamics driven at the metal-dielectric interface by the tightly confined optical fields. In particular, the dynamics of photo-excited ("hot") charge carriers inside the metal remains a topic of intense research, with potential applications in photo-catalysis and nanoscale light sources. While bulk metals show negligible luminescence under optical or electrical excitation, their intrinsic emission quantum yield can be enhanced by orders of magnitudes thanks to the giant Purcell factor of plasmonic nanocavities [102, 105, 119–121]. This plasmon-enhanced photoluminescence (PL) has a growing number of applications in imaging and nano-science [122–125], yet its underlying principles are still under debate [103, 105]. It is generally accepted that both interband and intraband transitions contribute to the radiative recombination of photo-excited carriers, with their relative contributions determined by the band structure of the metal [126], the electron-hole pair energy, and the degree of spatial confinement [127, 128]. In contrast to the mesoscopic scale (10- 100 nm) involved in the plasmonic response, at which the band structure of the metal is bulk-like, studies of metal clusters and nanoparticles of sizes below a few nanometers have shown that quantum confinement leads to bright emission from discrete energy states, as well as from metal-ligand hybrid states [123, 129–131]. To date, these two domains have been largely considered as separate realms.

In this chapter, it is demonstrated that such a picture is not valid. The intrinsic light emission from gold and silver plasmonic nanojunctions generally consists of two components: (i) a stable hot-carrier-induced emission following the plasmonic resonances and governed by the bulk metal band structure, and (ii) an hitherto overlooked contribution from quantum confined emitters randomly forming and disappearing near the metal surface under the influence of the highly confined optical field. This latter blinking emission, which is the focus of our study, is made observable thanks to the Purcell effect provided by the mesoscopic plasmon modes, but features distinct spectral content, with sharper linewidth (higher Q-factor) and quantum yield that can be orders of magnitude larger than the hot-carrier emission. The blink-

ing emission occurs without noticeable change in the near-field nor in the plasmonic response, excluding all mechanisms proposed to date to explain fluctuating surface-enhanced Raman scattering and background emission in similar systems. The various nanojunction composition (metal and spacer) we studied evidenced that chemical reactions and morphology modifications at the interface between the metal and the spacer play a key role in the specific type of blinking observed whereas the blinking itself appears to be a universal mechanism characteristic of nanoscale junctions.

The discovery has fundamental relevance for the understanding of light-matter interaction in nanoscale cavities. The photo-induced luminescence blinking we explore in this chapter might be use in future studies as a tool for monitoring atomic scale motion and field induced material restructuring under tight plasmonic confinement. Moreover, our findings reveal a novel phenomenology where blinking is due to atomic restructuring instead of charge dynamics, as had been observed to date in molecular fluorophores and low-dimensional semiconductors. These observations highlight possible ways to engineer the quantum yield and spectrum of plasmonic nano-emitters, and also raises interrogations about the of bulk electronic band structure to model chemical interactions at the surface of plasmonic metals.

4.1 Blinking of the photoluminescence emission

Fig. 4.1 shows a first example of the temporal fluctuations of the photoluminescence signal. The signal emitted by a nanojunction consisting of a chemically synthesised single-crystal gold flake, a self-assembled biphenyl-thiol (BPT) monolayer, and a commercially available colloidal gold nanoparticle (nominal size 80 nm) both under 488 nm and 532 nm illumination clearly demonstrates the blinking nature of the intrinsic luminescence of nanojunctions.

All structures showing measurable PL emission also featured this new type of PL blinking, that can be very distinct from the stable baseline response. Fig. 4.2a shows an illustrative time series of the PL from a single nanojunction under 532 nm excitation, with several selected spectra and the average spectrum shown in Fig. 4.2b. This excitation wavelength matches the main interband (d to sp band) transitions in gold and is also resonant with the transverse plasmon mode of the nanojunction, further enhancing the absorption cross-section and resulting in the strongest observed PL signal. Yet, blinking PL was also observed, with lower intensity, under 633 and 785 nm excitation wavelengths.

The baseline (non-blinking) emission, stable over time, is assigned to the Purcell-enhanced radiative recombination of hot carriers, with contributions from both inter- and intra-band processes, as discussed in previous literature [102, 105, 119, 120]. After accounting for the small relative area of the nanojunction compared to the spot size, the actual gold emission enhancement factor compared to the bare substrate is on the order $10^4 - 10^5$, consistent with a field enhancement in excess of 100-fold in at the metal surface layer near the gap.

But most surprisingly, we find that the PL is dominated by strongly fluctuating and spectrally
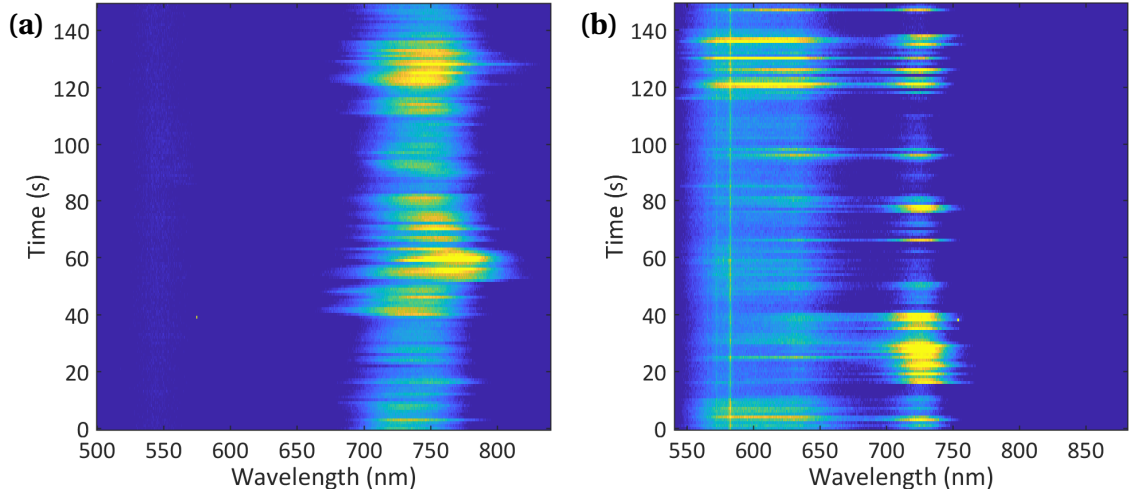
Figure 4.1 – Time series of photoluminescence (PL) in normalized counts units for a single nanojunction consisting of an 80 nm faceted gold nanoparticle separated from a single-crystal gold microplate by a BPT monolayer under continuous 488 nm **(a)** and 532 nm **(b)** laser illumination.

wandering lines, with linewidth narrower than that of the underlying baseline emission, as is best seen in Fig. 4.2b. It seems difficult to explain this blinking emission using the conventionally accepted plasmon-enhanced PL mechanisms discussed above. Indeed, and even in cases where the spectral profile of the blinking emission closely follows the baseline PL, we demonstrate in the next section that the field enhancement inside the gap and the plasmonic resonance are *not* fluctuating during the blinking process. All observations suggest a fundamentally new mechanism causing PL blinking.

4.2 Probing the local field with a Raman probe

To obtain and independent probe of the local field enhancement, while simultaneously monitoring PL blinking, we perform two-tone excitation with both a 532 nm laser, efficiently generating PL, and with another continuous wave laser tuned at 750 nm so that the Stokes vibrational Raman signal from the BPT molecules embedded in the gap is resonant with the near-infrared plasmonic mode (Fig. 4.3). The Raman signal is a sensitive probe of the field enhancement inside the gap [117, 132–135], and any strong change in local field enhancement that would explain PL blinking would also leave a trace on the Raman signal. Remarkably, the fluctuations of the Raman signal remain within the intrinsic measurement noise (including shot noise and technical noise), while much more pronounced fluctuations of the underlying PL emission are observed. This measurement (which was repeated on many nanojunctions with the same result) provides strong evidence that the near-field enhancement and the local density of photonic states remain stable during PL blinking. This is in stark contrast with previous observations of fluctuating Raman scattering [136–138]. Recent reports have invoked the formation of 'picocavities' [133, 134] to explain such events, which are proposed to be
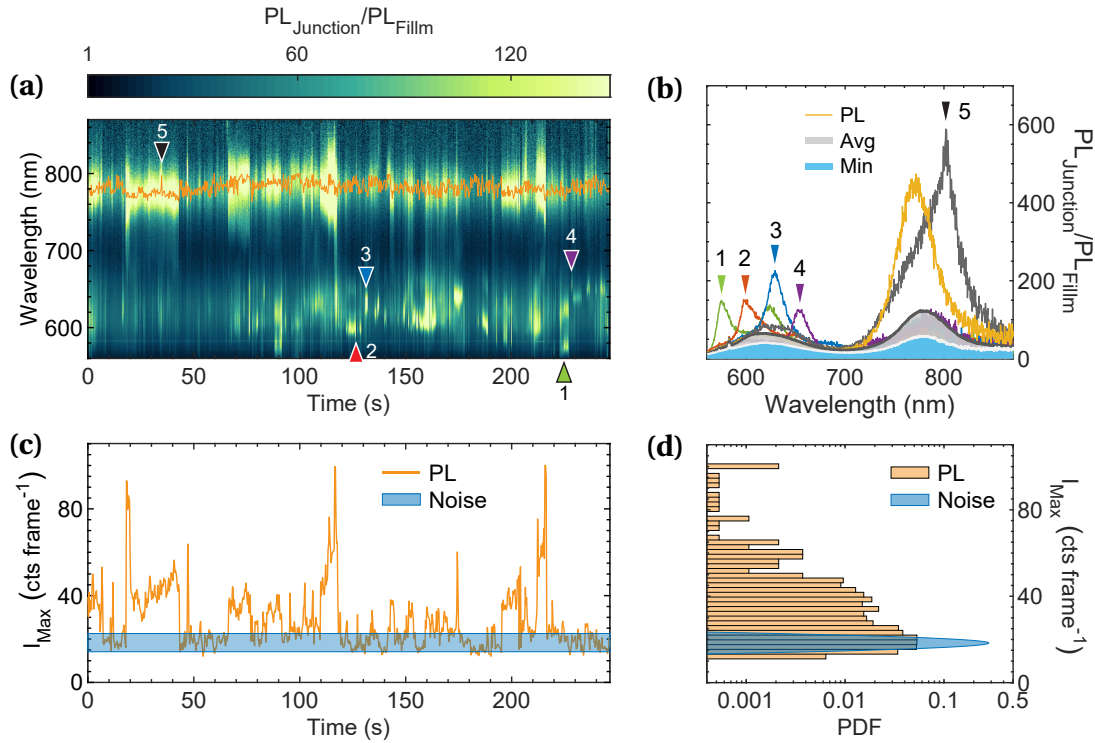
Figure 4.2 – **Blinking of photoluminescence (PL) in a single nanojunction**. **(a)** Time series of plasmonic emission under continuous 532 nm excitation. Laser power density ~ 7 × 10^3 W/cm², camera exposure time = 0.1 s, numerical aperture: 0.85. The measured counts are divided by the emission spectrum from the gold substrate acquired under the same conditions. **(b)** Individual spectra with special peaks (1 to 5, also labelled in **(a)** beyond the regime of plasmonic modes, together with the average spectrum in shaded grey. **(c)** Time trace of the maximum PL intensity marked by orange dots in **(a)**. **(d)** Corresponding probability density distribution (PDF). In **(c)** and **(d)** the shaded blue area is the PDF of the setup measurement noise D.1. Figure created by W. Chen.
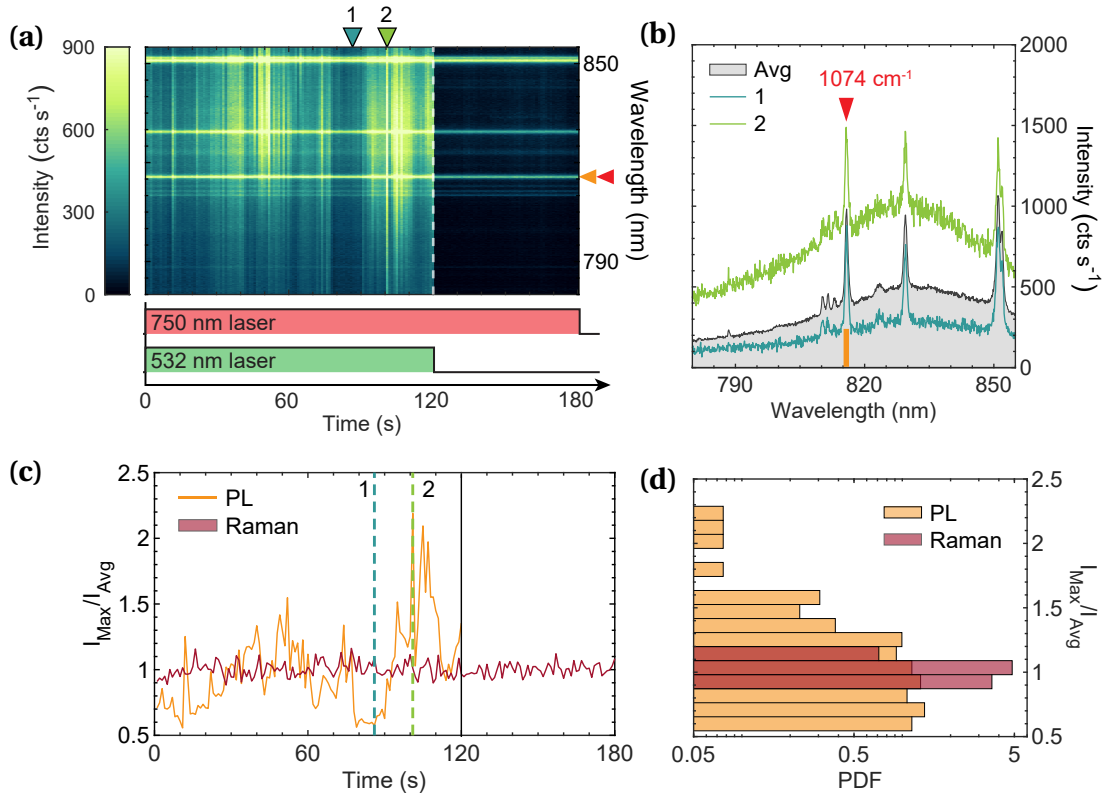
Figure 4.3 – Blinking PL with stable plasmon-enhanced Raman and dark-field (DF) scattering spectra. (a) Time series of emission spectra acquired under dual excitation with 532 nm and 750 nm laser beams (first 120 s) with respective power densities $\sim 2 \times 10^4$ W/cm^2 and $\sim 1 \times 10^3$ W/cm^2, and then with 750 nm excitation alone (after 120 s). Camera exposure time = 1 s, numerical aperture: 0.95. **(b)** Example of individual spectra and time-averaged spectrum (over the first 120 s). **(c)** Maximum intensity per frame, normalized by the time-averaged intensity, for both PL and Raman signals. **d** Probability density function of the normalised intensities. Figure created by W. Chen.

related to metal protuberances causing atomic scale confinement of light. Our measurements show that PL blinking does not share the same mechanism with such unusual Raman events. More generally, all models based on local field variations fail to explain our observations.

Note that under 750 nm excitation alone, the absence of interband transitions in gold dramatically reduces the PL excitation cross-section, and we typically observe negligible amount of PL – except for the rare brightest events, which may be related to the so-called 'flares' reported in [139]. Importantly, these 'flares' also occurs without change in Raman intensity, and as such it may share the same mechanism as PL blinking under shorter wavelength excitation. Interestingly the observed luminescence under 750 nm can be altered by the earlier exposition of the sample to a 532 nm illumination (cf. Fig 4.4). Alike a charging mechanism the resulting luminescence at 750 nm can feature blinking of the type observed under 532 nm illumination.
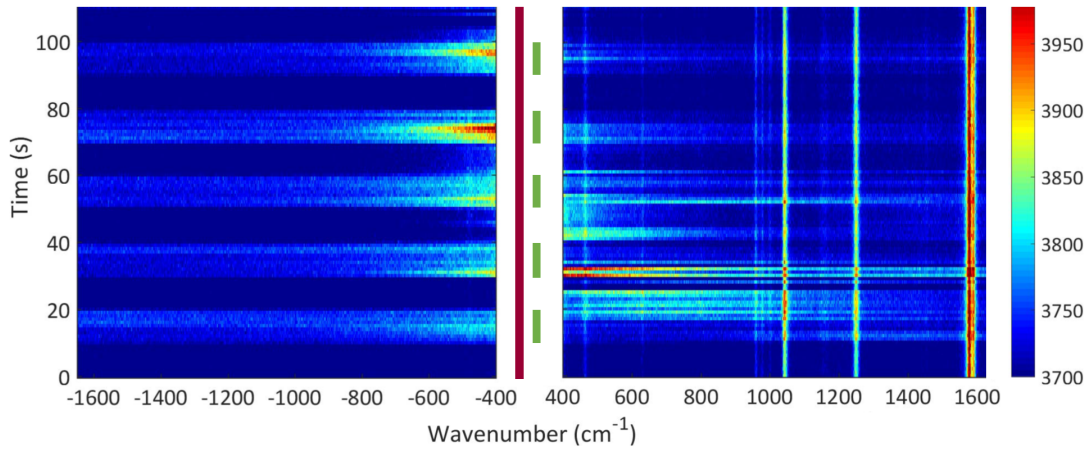
Figure 4.4 – Time series of the signals arising from a single nanojunction under continuous 750 nm and discontinuous 532 nm illuminations with respective powers of 32 μW and 30 μW. The vertical signals depict the different Raman lines whereas the lighter blue area (higher luminescence) coincide with the time intervals for which the 532 laser tone is activated. The spectral region between -400 and 400 cm^{-1} is blocked by tunable filters in order to reject the reflection of the incoming 750 nm laser tone on the sample.

4.3 Multi-mode analysis of the photoluminescence

To accommodate all our findings so far, we propose that new emission centers are being formed during laser irradiation, consisting of nanoscale metallic domains or few atom clusters, partially decoupled from the bulk metal, whose optical transitions are dominated by quantum confined electronic states within the $s - p$ band of gold (possibly hybridized with electronic states of the spacer material, in particular through their sulfur atoms). This model naturally explains why blinking is accompanied by negligible perturbation in the local field and plasmonic response (Fig. 4.3), since the nano-emitters are formed within the surface layer of the

metal – not inside the gap – and their impact on the electronic properties of the vastly larger nanoparticle and substrate is minute. The emission wavelength and linewidth of a randomly forming quantum confined emitter should be independent from the plasmonic spectrum, while the latter provides a large Purcell-enhancement which makes the blinking emission predominant in the region of plasmonic resonances, as observed.

Akin to the physics of fluorophores (molecules and quantum dots), PL of Au nanoclusters results from the radiative recombination of discrete electronic states formed by quantum confinement, with their PL wavelength, quantum yield and lifetime strongly dependent on their size and on metal-ligand interactions. The differently sized Au emitters with these varied optical properties are randomly or simultaneously created coupling to the plamsonic nanocavity, resulting in the fluctuation of the peak positions, intensity and Q-factor of the PL from the nanojunctions (Fig. 4.6). This localised emitter model also describes well the appearance of sharp emission out of the regime of plasmonic modes (peak 1-5 in Fig. 4.2).
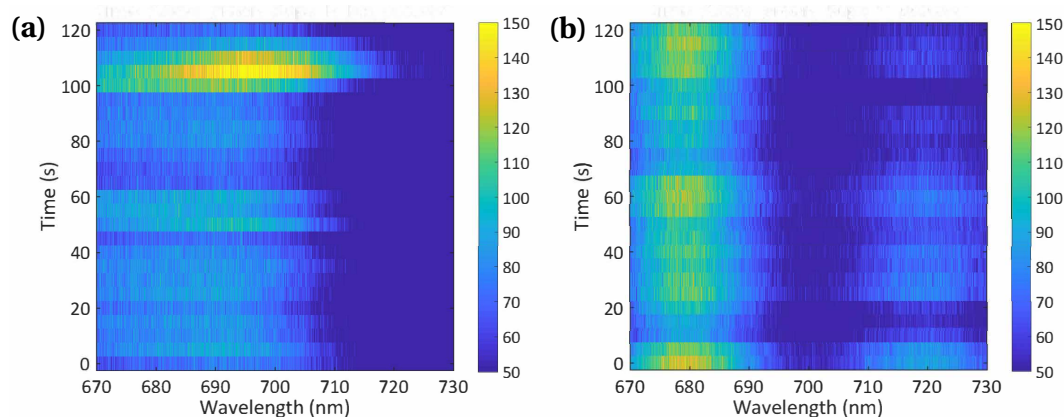
Figure 4.5 – Time series background subtracted photoluminescence for 5 s acquisitions under radial 532 nm illumination and with the addition of a polarizer in the detection path. The main axis of the polarizer is oriented so that it attenuates maximally **(a)**, minimally **(b)** the PL peak around 680 nm.

Additional measurements show that the blinking persists even at the lowest accessible excitation powers (on the order of $1\ \mathrm{W/cm^2}$) and the blinking duration can be shorter than 1 ms, meaning that PL blinking is a sensitive probe for localised effects and atomic dynamics at the metal surface with nanoscale sensitivity.

The visualization of these atomic dynamics in the photoluminescence signal can be retrieved from the blinking statistics of the different modes. For example the addition of a polarizer in the outgoing optical path enables to differentiate between the polarizations of the different nanogap modes light emission (Fig. 4.5) even when spectrally overlapping. The modifications of individual gap emission would thus provide information on the modifications of the metal surface inside the gap and according to the specific near-field distribution of the gap mode.

To provide additional support for this hypothesis, we implement full-wave simulation of a
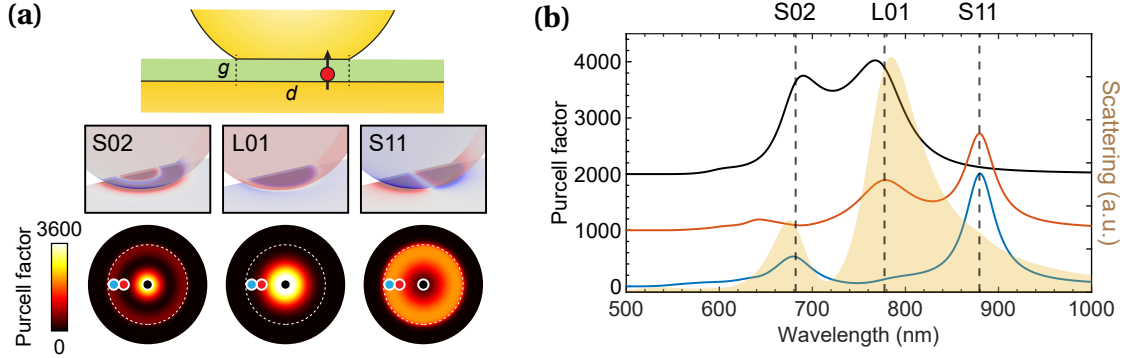
Figure 4.6 – **Simulation of the optical response of a faceted nanojunction.** **(a)** Based on the surface charge distributions taken at resonance, the modes are identified as the lowest frequency Fabry–Pérot-like transverse cavity mode S11, the dipolar bonding antenna mode L01 and the higher-order cavity mode S02, respectively. These modes feature distinct spatial distributions of the photonic density of states (PDOS) in the near-field, which results in different far-field emission spectra (solid lines in **(b)**, offset for clarity) when a radiating point dipole is placed at different locations marked by color-coded full circles in **(a)**. Simulations by our collaborator H. Hu in Wuhan University. Figure created by W. Chen and H. Hu.

nanojunction consisting of a 80 nm Au nanoparticle with facet size d = 40 nm on a Au mirror with spacer thickness g = 1.3 nm (Fig. 4.6a). To emulate a randomly generated PL emitter, we use an electric dipole placed on the metal surface at three different positions (blue, red and black dots in the bottom panel of Fig. 4.6a), which couples to the plasmonic nanocavity and radiates to the far-field. The three resulting emission spectra (Fig. 4.6b) are clearly distinct, even though they remain consistent with the three quasi-normal modes also visible in the scattering spectrum under plane-wave excitation (shaded yellow curve). This shows that a spatially localized increase in PL quantum yield is consistent with uncorrelated fluctuations from different regions of the spectrum. Such a process could be caused by the formation of new grain boundaries that relax wave-vector conservation, leading to a local increase in intraband radiative recombination rate. Our dual-tone measurements (Fig. 4.4) suggest that the modification of these grain boundaries or nano-domains is frequency dependent suggesting that optical forces alone could not explain the observed changes. It should be noted that other mechanisms involving charge transfer through the junction [140, 141] cannot be excluded. Additional measurements implying an electro-chemical cell are currently being performed to address this question.

Fig. 4.7a displays another representative time trace with a typical multi-peak emission (Fig. 4.7b). We carefully analyze the spectral wandering and lineshape narrowing that accompanies blinking, and study the correlations that may exist between fluctuation in emission wavelength, intensity and linewidth from different regions of the full spectrum. Each emission peak can be attributed to a plasmonic quasi-normal mode of the nanojunction (labelled as L01 and S02, which will be discussed later), and PL blinking occurs for both of them. For each mode,

we track the wavelength of maximum emission (Fig. 4.7a), the peak intensity and linewidth (expressed as Q-factor). In general our data indicate low level of correlation between the respective peak positions (Fig. 4.7c) or intensities (Fig. 4.7d) around the L01 vs. S02 modes, suggesting again that any model relying on the modification of the entire plasmonic response [139] would fail to explain our observations.
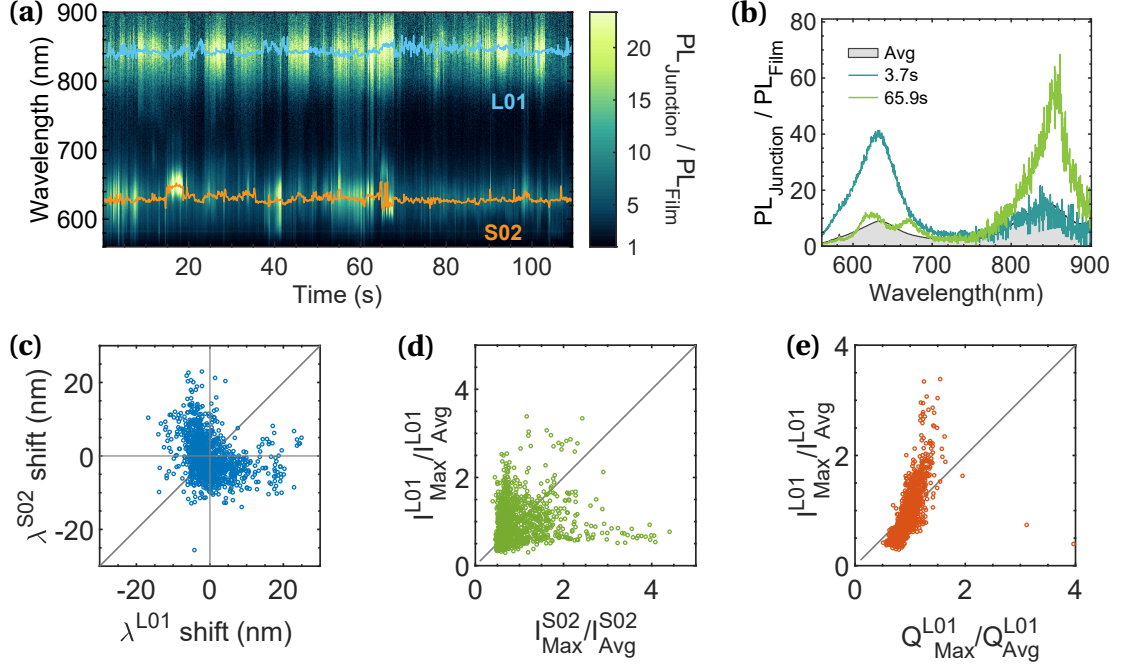
Figure 4.7 – **Multi-mode blinking: evidence for spatially localized fluctuating sources of emission.** **(a)** Example of fluctuating emission from a nanojunction exhibiting two active modes. The top panel shows representative spectra of strong emission in either mode. Excitation power density at 532 nm: $\sim 3.5 \times 10^4$ W/cm^2, numerical aperture 0.85, exposure time: 0.1s. **(b)** Distribution of the normalized emission intensities of one resonance vs. the other. **(c-e)** Blinking statistics of the different radiative modes. Figure created by W. Chen.

In conclusions, our results open a whole new area of studies in plasmonic nanojunctions, involving phenomena at the interface between the atomic and mesoscopic scale. Moreover, our findings raise new questions regarding the microscopic mechanisms governing light emission from plasmonic nanojunctions, impacting their applications as nanoscale emitters. It remains an open question whether the local changes in electronic properties revealed by PL blinking can have relevant implications for energy harvesting, photocatalysis and photodetection applications that rely on plasmonic hot carrier harnessing.

5 Molecular platform for single photon up-conversion

In this chapter we highlight an exciting new route for systems combining cavities and molecular systems that address some long-standing technological challenges for thermal imaging and spectroscopy [142]. Driven by applications in astronomy, novel cryogenic detectors in the THz range appeared in the last few years [143, 144]. However the ability to efficiently manipulate such electromagnetic signals at room temperature is still lacking [145, 146]. In particular, single photon detection, which is now routine in the VIS-NIR region (wavelength in vacuum from 400 nm to 2000 nm), remains impossible or unpractical at longer wavelengths. Development of new detection devices operating without complex cryogenic apparatus, and featuring improved sensitivity, lower noise and reduced footprint, would significantly impact sensing, imaging, spectroscopy and communication technologies.

The scheme presented here suggests a new route to achieve low-noise detection of non-coherent THz and MIR radiation by leveraging optomechanical transduction with molecules [147], whose natural oscillation frequencies are resonant with the incoming field. Our strategy consists in converting the incoming low-frequency signal onto the anti-Stokes sideband of a pump laser in the VIS-NIR domain, where detectors with single photon sensitivity are readily available [148, 149]. This approach is inspired by the recent realization of coherent frequency conversion using different types of optomechanical cavities [150–156] and is conceptually disctinct from a recently demonstrated detection scheme assisted by a microfabricated resonator [157]. As an outlook, we propose to leverage constructive interference between signals coming from an array of coherently pumped up-converters in order to increase further the strength of the converted signal over the incoherent thermal noise.

While coherent conversion from the MIR to the VIS-NIR domain has so far been achieved by sum-frequency generation in bulk non-linear crystals [158–161], these schemes operated under several Watts of pump power and required phase-matching between the different fields propagating in the crystal. Our scheme, on the contrary, relies solely on the spatial overlap of the two incoming fields. Indeed, we use a nanometer-scale dual antenna that confines both electromagnetic fields into similar sub-wavelength mode volumes. The optomechanical interaction with the vibrational system takes place in the near field, without need to fulfil a phase

matching condition. Moreover, thanks to the giant field enhancement provided by plasmonic nano-gaps, the required pump powers to achieve efficient conversion is dramatically reduced.

The protocol that we introduce leverages the intrinsic ability of specific molecular vibrations to interact both resonantly with MIR-THz fields and parametrically with VIS-NIR fields, as routinely observed in infrared absorption and Raman spectroscopy, respectively. The wealth of accessible vibrational modes and frequencies [2, 162] offers a convenient toolbox to realize efficient frequency up-conversion for several technological regions of interest (atmospheric window, thermal imaging and THz gap).

We first introduce the framework describing the interaction between a molecular vibration and two electromagnetic fields, one that is resonant with the vibrational frequency, the other one that is parametrically coupled to it through the molecular polarization. We compute the conversion efficiency and the noise figures-of-merit of our novel device as a function of the optical pump detuning and power. We find that internal conversion efficiencies on the order of a few percent and noise equivalent power below 10^{-12} W/$\sqrt{\text{Hz}}$ are achievable with our proposed design, and we demonstrate the potential of this approach to reach single-photon detection in the MIR and THz domain.

5.1   Absorption of incoming IR radiation by a vibrational mode

We describe in the following the coupling between a resonant field and a single vibrational mode inside a cavity (i.e. antenna). We also derive the expression given in the main text for the number of phonons created. Our treatment is inspired by the treatment adopted in Ref. [163].

The interaction between an external monochromatic field of frequency ω_{IR} and the molecular vibration in the dipole approximation inside a cavity is given by :

$$\hat{H}_{\text{int}} = -\vec{d} \cdot \vec{\mathcal{E}}_{\text{IR}}, \tag{5.1}$$

where $\vec{\mathcal{E}}_{\text{IR}} = i\sqrt{n_{\text{IR}}} \left[e^{-i\omega_{\text{IR}}t} e^{-i(\phi+\phi_0)t} \vec{\mathcal{E}}_0 - e^{i\omega_{\text{IR}}t} e^{i(\phi+\phi_0)t} \vec{\mathcal{E}}_0^* \right]$ with ϕ the phase offset between the field and the dipole, ϕ_0 an adjustable phase parameter of the driving field. $\vec{\mathcal{E}}_0 = \sqrt{\frac{\hbar\omega_{\text{IR}}}{2\varepsilon_0 V_{\text{IR}}}} \vec{e}_k$ is the vacuum field, with V_{IR} the mode volume and $\vec{e}_k$ the unit polarization vector of the IR mode.

This interaction can be written in terms of the bosonic ladder operators describing the IR mode inside the cavity $\hat{a}_{\text{IR}}^\dagger, \hat{a}_{\text{IR}}$ and the vibrational phononic operators $\hat{b}_\nu^\dagger, \hat{b}_\nu$ at frequency ν. For a weak IR drive the vibrational Hilbert space can be reduced to ground and first excited state $\{|0\rangle, |1\rangle\}$ and described like a two level system (TLS) with creation and annihilation operators $\hat{\sigma}_\nu^+, \hat{\sigma}_\nu^-$ [29]. We note that the validity of the TLS description for a collective vibrational mode of N oscillators would only break down for a number of excitations of order N [164].

The dipolar transition is purely nondiagonal in this basis and described as $\vec{d} = d_\nu \left(\hat{\sigma}_\nu^- \vec{e}_\nu + \hat{\sigma}_\nu^+ \vec{e}_\nu^* \right)$.

The field inside the cavity is in turn described by $\vec{\mathscr{E}}_{\text{IR}} = -i\sqrt{\bar{n}_{\text{IR}}}\mathscr{E}_0\left[e^{-i\phi_0}\hat{a}_{\text{IR}}\vec{e}_k - e^{i\phi_0}\hat{a}_{\text{IR}}^\dagger\vec{e}_k^*\right]$ [164]. In a frame rotating at the frequency of the IR driving field we only have to take into account the resonant processes ($\hat{a}_{\text{IR}}^\dagger\hat{\sigma}_v^-, \hat{a}_{\text{IR}}\hat{\sigma}_v^+$) and we obtain the interaction Hamiltonian :

$$\hat{H}_{\text{int}} = -i\hbar g_{\text{IR}}\left(e^{-i\phi_0}\hat{a}_{\text{IR}}^\dagger\hat{\sigma}_v^- + e^{i\phi_0}\hat{a}_{\text{IR}}\hat{\sigma}_v^+\right), \tag{5.2}$$

with $g_{\text{IR}} = \dfrac{d_v \cdot \mathscr{E}_0}{\hbar}\sqrt{\bar{n}_{\text{IR}}}\vec{e}_v^*\vec{e}_k e^{i\phi_0} = g_{\text{IR},0}\sqrt{\bar{n}_{\text{IR}}}$.

Here we choose the additional phase term of the driving field in order for the coupling to be real positive, without loss of generality.

We follow the dynamics of the TLS in this rotating frame. Introducing the rate Γ_{tot} which describes the total damping of the vibrational mode as described in the main text, we obtain :

$$\dot{\rho}_{11} = i\frac{g_{\text{IR}}}{2}\left(\rho_{10} - \rho_{01}\right) - \Gamma_{\text{tot}}\rho_{11} \tag{5.3a}$$

$$\dot{\rho}_{00} = -i\frac{g_{\text{IR}}}{2}\left(\rho_{10} - \rho_{01}\right) + \Gamma_{\text{tot}}\rho_{11} \tag{5.3b}$$

$$\dot{\rho}_{01} = -i\delta\rho_{01} - i\frac{g_{\text{IR}}}{2}\left(\rho_{11} - \rho_{00}\right) - \frac{\Gamma_{\text{tot}}}{2}\rho_{01} \tag{5.3c}$$

$$\dot{\rho}_{10} = i\delta\rho_{10} + i\frac{g_{\text{IR}}}{2}\left(\rho_{11} - \rho_{00}\right) - \frac{\Gamma_{\text{tot}}}{2}\rho_{10}, \tag{5.3d}$$

with $\delta = \omega_{\text{IR}} - \omega_v$ the detuning between the IR drive and the vibrational resonance.

These equations are often described with the help of the Bloch vector components:

$$u = \frac{1}{2}\left(\rho_{01} + \rho_{10}\right) \tag{5.4a}$$

$$v = \frac{1}{2i}\left(\rho_{01} - \rho_{10}\right) \tag{5.4b}$$

$$w = \frac{1}{2}\left(\rho_{11} - \rho_{00}\right). \tag{5.4c}$$

The components u, v of the Bloch vectors are related to the average dipole value [163]: $\langle\vec{d}\rangle = 2\vec{d}_v\left(u\cos\omega_{\text{IR}}t - v\sin\omega_{\text{IR}}t\right)$. We derive the master equations as a function of these components:

$$\dot{u} = \delta v - \frac{\Gamma_{\text{tot}}}{2}u \tag{5.5a}$$

$$\dot{v} = -\delta u - g_{\text{IR}}w - \frac{\Gamma_{\text{tot}}}{2}v \tag{5.5b}$$

$$\dot{w} = g_{\text{IR}}v - \Gamma_{\text{tot}}w - \frac{\Gamma_{\text{tot}}}{2}. \tag{5.5c}$$

The steady-state solutions of these equations are :

$$\bar{u} = \frac{g_{IR}}{2} \frac{\delta}{\delta^2 + \left(\Gamma_{tot}^2/4\right) + \left(g_{IR}^2/2\right)} \tag{5.6a}$$

$$\bar{v} = \frac{g_{IR}}{2} \frac{\Gamma/2}{\delta^2 + \left(\Gamma_{tot}^2/4\right) + \left(g_{IR}^2/2\right)} \tag{5.6b}$$

$$\bar{w} + \frac{1}{2} = \frac{g_{IR}^2}{4} \frac{1}{\delta^2 + \left(\Gamma_{tot}^2/4\right) + \left(g_{IR}^2/2\right)}. \tag{5.6c}$$

The average number of photons absorbed per unit time by the vibrational dipole is given by :

$$\frac{d\bar{n}_b^{IR}}{dt} = \frac{d\bar{W}^{IR}}{dt} \frac{1}{\hbar\omega_{IR}} = \frac{\vec{\mathcal{E}}_n \cos\omega_{IR} t \cdot \langle \dot{\vec{d}} \rangle}{\hbar\omega_{IR}}. \tag{5.7}$$

If the detuning and coupling are much smaller than the vibrational damping rate ($\delta, g_{IR} < \Gamma_{tot}$), the average number of absorptions over an IR period can be written as :

$$\frac{d\bar{n}_b^{IR}}{dt} = g_{IR}\bar{v} = \frac{g_{IR}^2}{2} \frac{\Gamma_{tot}/2}{\delta^2 + \left(\Gamma_{tot}^2/4\right) + \left(g_{IR}^2/2\right)} \simeq \frac{g_{IR}^2}{\Gamma_{tot}}. \tag{5.8}$$

In the steady state the rate of photons absorbed by the vibrational mode equals the phonon damping rate so that the average number of excited phonons is :

$$\bar{n}_b^{IR} = \frac{d\bar{n}_b^{IR}}{dt} \frac{1}{\Gamma_{tot}} = \frac{g_{IR}^2}{\Gamma_{tot}^2} = \frac{g_{IR,0}^2}{\Gamma_{tot}^2} \bar{n}_{IR} = \frac{g_{IR,0}^2}{\Gamma_{tot}^2} \frac{\kappa_{ex}^{IR}}{\delta^2 + (\kappa^{IR}/2)^2} \tilde{S}_{IR}^{in} \overset{\delta \ll \kappa^{IR}}{=} \frac{4g_{IR,0}^2}{\Gamma_{tot}^2} \frac{\eta_{IR}}{\kappa^{IR}} |\langle \hat{a}_{IR}^{in}\rangle|^2. \tag{5.9}$$

We note that the average number of excited phonons $\bar{n}_b^{IR}$ can also be simply derived from the steady-state population of the upper TLS state $\bar{n}_b^{IR} = \bar{w} + \frac{1}{2}$.

5.2 Optical conversion scheme

We start with the description of the two types of interactions leveraged in the conversion process and describe the relevant parameters. For simplicity, we now use the abbreviation IR to denote MIR or THz fields, depending on the vibrational frequency considered. First we model the resonant absorption process. We assume that the vibrational system is weakly driven, meaning that the average number of excited collective vibrational quanta is much smaller that the total number of molecular oscillators coupled to the incoming field. At the single molecule level this easily satisfied condition results in considering the single transition from the ground to the first excited vibrational state. The collective excitation of an ensemble of vibrational modes can thus be treated as an ensemble of two-level systems [165].

The interaction part of the Hamiltonian is correspondingly approximated by :

$$\hat{H}_{\text{int}} = -i\hbar g_{\text{IR},0}^{(N)} \sqrt{\bar{n}_{\text{IR}}} \left(\hat{a}_{\text{IR}}^\dagger \hat{\sigma}_v^- + \hat{a}_{\text{IR}} \hat{\sigma}_v^+ \right), \tag{5.10}$$

with $\hat{a}_{\text{IR}}^\dagger$, $\hat{a}_{\text{IR}}$ the IR field bosonic ladder operators and $\hat{\sigma}_v^+$, $\hat{\sigma}_v^-$ the raising and lowering operators of the collective two level system described by a transition frequency ω_v. $g_{\text{IR},0}^{(N)} = \sqrt{N_{\text{IR}}} g_{\text{IR},0}$ is the N-molecule resonant vacuum coupling rate of the vibrational mode v and $\bar{n}_{\text{IR}}$ the mean occupation of the IR antenna mode.

The incoming IR field at frequency ω_{IR} is enhanced by a frequency-matched antenna and performs work on the collective transition dipole $\vec{d}_v$ of the molecular vibration [163]. On resonance ($\omega_{\text{IR}} = \omega_v$) the averaged number of created phonons is

$$\bar{n}_b^{\text{IR}} = \left(\frac{2g_{\text{IR},0}^{(N)}}{\Gamma_{\text{tot}}} \right)^2 \frac{\eta_{\text{IR}}}{\kappa^{\text{IR}}} |\langle \hat{a}_{\text{IR}}^{\text{in}} \rangle|^2 \tag{5.11}$$

with $|\langle \hat{a}_{\text{IR}}^{\text{in}} \rangle|^2$ the incoming IR photon flux. In this expression $\kappa^{\text{IR}} = \kappa_{\text{ex}}^{\text{IR}} + \kappa_0^{\text{IR}}$ is the loss rate of the antenna at the incoming frequency, which is the sum of the external decay rate $\kappa_{\text{ex}}^{\text{IR}}$ (by coupling to the incoming far-field modes) and the internal decay rate κ_0^{IR} (by metallic absorption and scattering to other modes), $\eta_{\text{IR}} = \kappa_{\text{ex}}^{\text{IR}}/\kappa^{\text{IR}}$ the coupling ratio of the antenna and Γ_{tot} the total vibrational decay rate, where the intrinsic vibrational linewidth Γ_v is modified by its coupling to the IR antenna [166].

As pictured in Fig. 5.1, we employ a second antenna resonant at ω_c (a frequency in the VIS-NIR domain, which we call "optical" domain from here on for brevity), whose decay rates $\kappa_{\text{ex}}^{\text{opt}}$, κ_0^{opt} are defined in the same way as the IR antenna parameters. The optical antenna enhances the parametric optomechanical interaction of the molecular vibration with a pump laser in the optical domain, as described in [147]. Concisely the interaction between an optical field and N_{opt} molecular oscillators leads to a dispersive interaction described by the Hamiltonian $\hat{H}_{\text{int}} = -\hbar g_{\text{opt},0}^{(N)} \hat{a}_{\text{opt}}^\dagger \hat{a}_{\text{opt}} \left(\hat{b}_v + \hat{b}_v^\dagger \right)$ with $g_{\text{opt},0}^{(N)} = \sqrt{N_{\text{opt}}} g_{\text{opt},0}$ the collective optomechanical vacuum coupling rate and $\hat{a}_{\text{opt}}^\dagger$, $\hat{a}_{\text{opt}}$ $\left(\hat{b}_v^\dagger, \hat{b}_v \right)$ the optical pump field bosonic ladder operators (the vibrational phononic operators at frequency v).

The optical antenna field can be split into an average coherent amplitude α and a fluctuating term so that $\hat{a}_{\text{opt}} = \alpha + \delta \hat{a}_{\text{opt}}$. Expanding to first order in α the optomechanical interaction we obtain the linearized interaction

$$\hat{H}_{\text{lin}} = -\hbar g_{\text{opt},0}^{(N)} \sqrt{\bar{n}_{\text{opt}}} \left(\delta \hat{a}_{\text{opt}}^\dagger + \delta \hat{a}_{\text{opt}} \right) \left(\hat{b}_v + \hat{b}_v^\dagger \right), \tag{5.12}$$

with $\bar{n}_{\text{opt}} = |\alpha|^2$ the mean occupation of the optical antenna mode (see Chapter 2).

The spectral density of the output field on the optical port in [photons/(Hz·s)] can be evaluated through the calculation of the two-time correlations of the optical output field operators
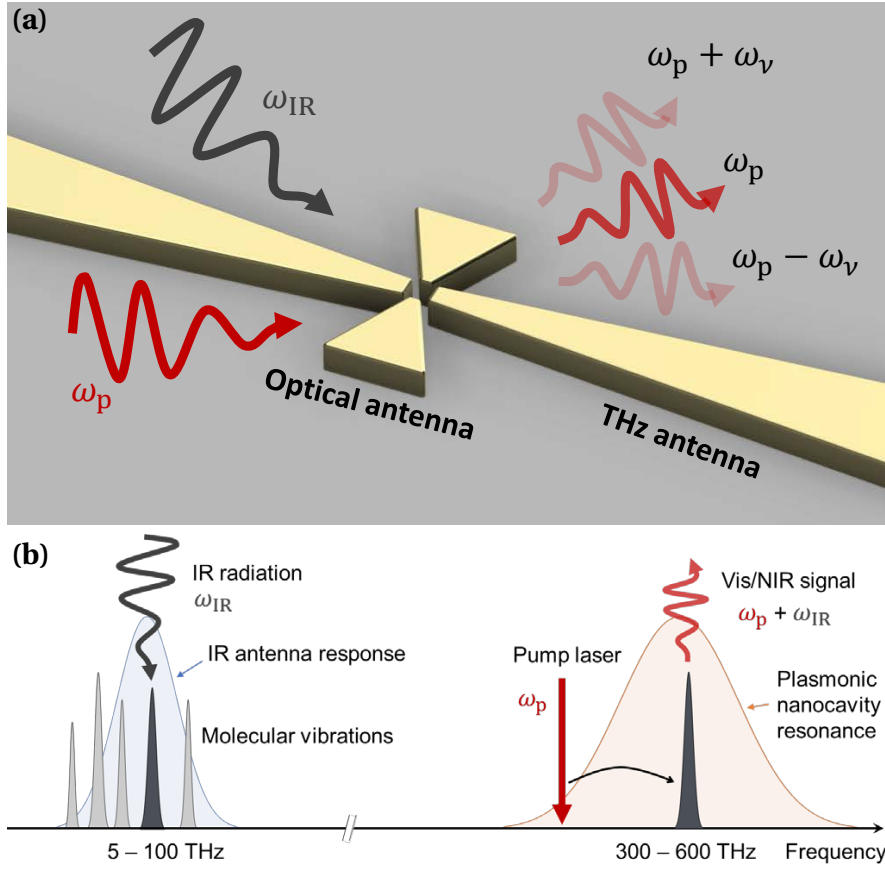
Figure 5.1 – **(a)** Illustration of the envisioned up-conversion device. Both electromagnetic modes are collected with the help of the dual-antenna and confined within a volume where molecules are located. **(b)** Frequency picture of the optomechanical conversion mechanism involving both IR absorption and Raman scattering by specific vibrational modes. Here the pump tone (ω_p) is red-detuned from the optical resonance ($\omega_c \simeq \omega_p + \omega_{IR}$) while the incoming IR signal is resonant with a specific vibrational mode ($\omega_{IR} = \omega_v$).

[29, 91]:

$$S^{\text{out}}(\omega) \propto \frac{\kappa_{\text{ex}}^{\text{opt}}}{2\pi} \left(\frac{\omega^3}{\omega_c^3}\right) \int_{-\infty}^{\infty} d\tau e^{i\omega\tau} \langle \delta\hat{a}_{\text{opt}}^{\dagger}(\tau)\delta\hat{a}_{\text{opt}}(0)\rangle, \tag{5.13}$$

where the prefactor in brackets takes into account the frequency dependence of the radiative coupling rate to the far-field of a dipolar emitter.

Following the complete derivation of the outgoing spectral density presented in Ref. [91] we derive the following expression for the anti-Stokes sideband noise spectral density

$$S_{\text{tot}}^{\text{out}}(\omega_{\text{aS}}) = \frac{2}{\pi} \frac{\omega_{\text{aS}}^3}{\omega_c^3} \frac{\eta_{\text{opt}} A^-}{\Gamma_v^* + \Gamma_{\text{opt}}} \bar{n}_f \tag{5.14}$$

with $\bar{n}_f$ the final phonon number in the vibrational mode given by the expression [91]

$$\bar{n}_f = \frac{\Gamma_\nu^*}{\Gamma_\nu^* + \Gamma_{\text{opt}}} \bar{n}_{\text{b}} + \frac{A^+}{\Gamma_\nu^* + \Gamma_{\text{opt}}}. \tag{5.15}$$

where $\bar{n}_{\text{b}} = \bar{n}_{\text{b}}^{\text{IR}} + \bar{n}_{\text{th}}$ is the total phonon number in the absence of optical drive. It is the incoherent sum of the IR-induced vibrational excitation (eq. 5.11) and the thermal noise, $\bar{n}_{\text{th}} = 1/\left(\exp\left[\hbar\omega_\nu/k_B T_{\text{bath}}\right] - 1\right)$ for a bath temperature T_{bath}. We assume here that the pump laser does not lead to significant Ohmic heating of the system. It is however straight-forward to model laser-induced heating by introducing a pump-power dependent bath temperature T_{bath}.

Due to the IR and optomechanical interactions the intrinsic vibrational damping rate is modified $\Gamma_{\text{tot}} = \Gamma_\nu^* + \Gamma_{\text{opt}}$ with Γ_ν^* the IR antenna-assisted damping rate and $\Gamma_{\text{opt}} = A^- - A^+$ the additional damping rate of electromagnetic origin characterized by the imbalance between the optical antenna-assisted transition rates to the ground A^- and excited vibrational states A^+ (see Chapter 2). We note that the optical interaction modifies the vibrational lifetime and thus the number of IR excited phonons in the steady state (eq. 5.11).

The resulting spectral density, $S_{\text{opt}}^{\text{out}}$, in the absence of incoming IR radiation ($\bar{n}_{\text{b}}^{\text{IR}} = 0$) should be integrated over the device's operational bandwidth (BW $\equiv \Gamma_{\text{tot}}$) to obtain its dark-count rate $\bar{S}_{\text{opt}}^{\text{out}} = \int_{\text{BW}} S_{\text{opt}}^{\text{out}} \, d\omega$. The dark-count rate arising from the thermal contribution to the first term in eq. 5.15 can be reduced by cooling the bath, whereas the second term describes a minimal noise level resulting from phonon creation by spontaneous Stokes scattering of the pump laser, a process equivalent to quantum backaction in cavity optomechanics. Therefore an optimal power that maximizes the signal-to-noise ratio (SNR) exists, akin to the standard quantum limit (SQL) in position measurements.

From these expressions we are also able to describe the conversion efficiency from an incoming rate of IR photons to an outgoing rate of optical photons : $\tilde{S}_{\text{IR}\rightarrow\text{opt}}^{\text{out}} = \eta_{\text{ext}}|\langle\hat{a}_{\text{IR}}^{\text{in}}\rangle|^2$ where $\eta_{\text{ext}} = \eta_{\text{rad}} \cdot \eta_{\text{int}} \cdot \eta_{\text{IR}}$ is the external conversion efficiency.

Starting again from the noise spectral density expression (eq. 5.14) and inserting the vibrational population expression (eq. 5.15) the different component appearing in the full noise spectral density can be identified

$$S_{\text{tot}}^{\text{out}}(\omega_{\text{aS}}) \propto \underbrace{\frac{A^-}{\Gamma_\nu^* + \Gamma_{\text{opt}}} \bar{n}_{\text{th}}}_{S_{\text{th}}^{\text{out}}} + \underbrace{\frac{A^- \Gamma_\nu^*}{\left(\Gamma_\nu^* + \Gamma_{\text{opt}}\right)^2} \eta_{\text{overlap}} \bar{n}_b^{\text{IR}}}_{S_{\text{IR}\rightarrow\text{opt}}^{\text{out}}} + \underbrace{\frac{A^-}{\left(\Gamma_\nu^* + \Gamma_{\text{opt}}\right)^2} \left[A^+ - \Gamma_{\text{opt}} \bar{n}_{\text{th}}\right]}_{S_{\text{ba}}^{\text{out}}}, \tag{5.16}$$

With this notation the total noise quanta in the outgoing optical field is defined as $S_{\text{opt}}^{\text{out}} = S_{\text{th}}^{\text{out}} + S_{\text{ba}}^{\text{out}}$.

Then, we obtain for the conversion efficiency :

$$\eta_{\text{ext}} = \underbrace{\frac{\omega^3}{\omega_c^3}\eta_{\text{opt}}}_{\eta_{\text{rad}}} \cdot \underbrace{\eta_{\text{overlap}} \cdot \frac{A^-\Gamma_v^*}{\Gamma_v^* + \Gamma_{\text{opt}}} \frac{1}{\kappa^{\text{IR}}} \left(\frac{2g_{\text{IR},0}^{(N)}}{\Gamma_v^* + \Gamma_{\text{opt}}}\right)^2}_{\eta_{\text{int}}} \cdot \eta_{\text{IR}}. \tag{5.17}$$

The radiative efficiency of the optical antenna mode into the far field is decomposed as $\eta_{\text{rad}} = (\omega/\omega_c)^3 \eta_{\text{opt}}$ with $\eta_{\text{opt}} = \kappa_{\text{ex}}^{\text{opt}}/\kappa^{\text{opt}}$ defined in the same way as η_{IR} introduced previously. These factors account for the coupling of free space radiation in and out of the nanostructure.

The internal conversion efficiency η_{int} can in turn be divided into a power dependent part $\eta_{\text{OM}}(\bar{n}_{\text{opt}})$ and a part describing the spatial overlap between the IR near field, the optical near field and the molecular ensemble, which we write η_{overlap}.

The first term can be further developed depending on the pump field detuning. For example, for a pump field red-detuned from the optical antenna resonance ($\Delta = \omega_p - \omega_c = -\omega_v$) it is possible to derive the explicit dependance of the internal conversion efficiency on both collective vacuum coupling rates

$$\eta_{\text{int}} = \eta_{\text{overlap}} \cdot \frac{\left(2g_{\text{opt},0}^{(N)}\right)^2 \bar{n}_{\text{opt}}}{\kappa^{\text{opt}}\left(\Gamma_v^* + \Gamma_{\text{opt}}\right)} \frac{\Gamma_v^*}{\left(\Gamma_v^* + \Gamma_{\text{opt}}\right)} \frac{\left(2g_{\text{IR},0}^{(N)}\right)^2}{\kappa^{\text{IR}}\left(\Gamma_v^* + \Gamma_{\text{opt}}\right)}. \tag{5.18}$$

To approximate the second term η_{overlap}, we factorize it into two contributions: the spatial overlap between the IR and optical near fields (η_{mode}) and the vectorial overlap between the near field polarization (typically normal to the antenna surface) and the molecular orientation, which we name η_{pol}; so that we can write

$$\eta_{\text{int}} \simeq \eta_{\text{pol}} \cdot \eta_{\text{mode}} \cdot \eta_{\text{OM}}(\bar{n}_{\text{opt}}). \tag{5.19}$$

The power and detuning dependences of the optomechanical efficiency term η_{OM} are depicted in Fig. 5.3 (b).

5.3 Molecular transducer

The electric dipole moment $\vec{\mu}_v$ and polarizability α_v of a vibrational mode can be directly extracted from experimental data of resonant light absorption and inelastic light scattering, respectively [2, 162]. In specific cases the symmetries of the vibrational mode lead to selection rules in its interaction with light [1]. For vibrational modes lacking centro-symmetry the derivatives of both quantities with respect to the displacement coordinate can be non-vanishing [1]. We show such a situation in Fig. 5.2 where we plot the projections of the derivatives of the electric moment and of the polarizability with respect to the molecular coordinate Q_v of the 1002 cm^{-1} mode of thiophenol, which we choose as an example in our calculations. We note

(a)

(b)
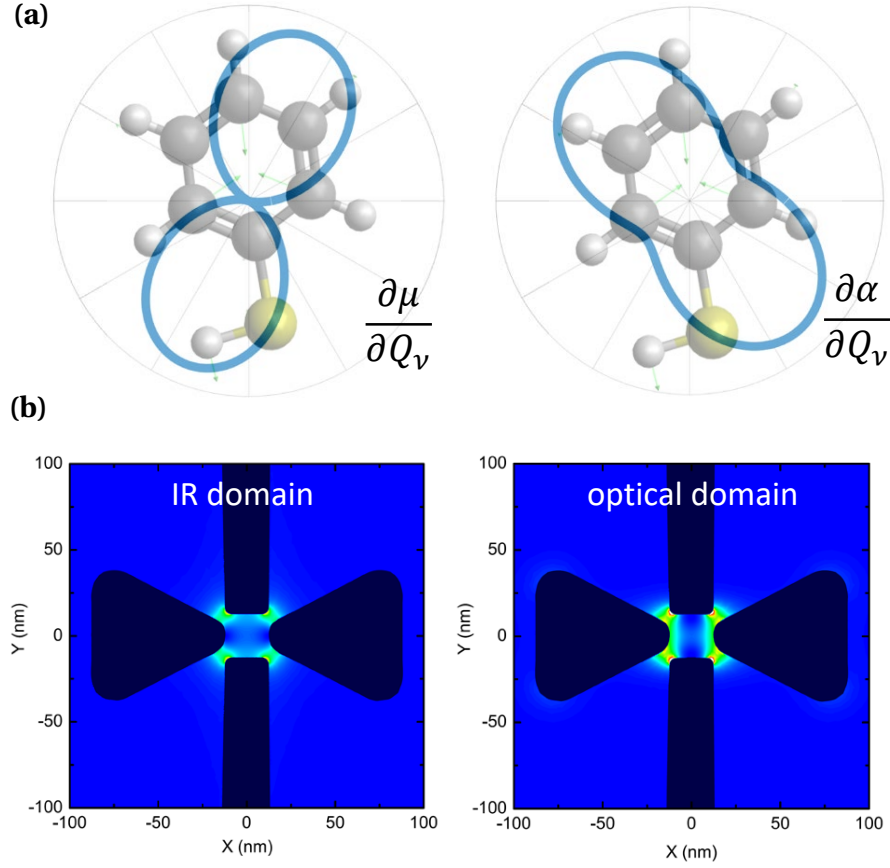
Figure 5.2 – **(a)** Polar plots of both the electric moment derivative (left) and the projection of the Raman tensor on the main plane of the molecule (right) for the vibrational mode $\tilde{\nu} = 1002$ cm^{-1} of the thiophenol molecule (background image). **(b)** Local density of states distribution inside the dual antenna for an IR mode at 32 THz (left) and a NIR mode at 374 THz (right).

that the projection of the tensor $\left(\frac{\partial \alpha_\nu}{\partial Q_\nu}\right)$ onto an axis perpendicular to the principal axis of the electronic moment derivative $\left(\frac{\partial \vec{\mu}_\nu}{\partial Q_\nu}\right)$ can be non-vanishing. Several polarizations for in- and outcoupling of resonant and up-converted fields are thus conceivable.

The calculations leading to the parametric optomechanical vacuum coupling rate $g_{\mathrm{opt},0}$ between the antenna field and the vibrational mode has been previously described [147] and its value is given by $g_{\mathrm{opt},0} = \omega_c \left(\vec{e}_{\mathrm{opt}} \cdot \frac{\partial \alpha_\nu}{\partial Q_\nu} \cdot \vec{e}_{\mathrm{opt}}\right) \left(\frac{1}{V_{\mathrm{opt}}\varepsilon_0}\right) \sqrt{\frac{\hbar}{2\omega_\nu}}$ with α_ν the polarizability tensor, Q_ν the reduced displacement coordinate of the vibrational mode labelled by ν, V_{opt} the optical mode volume and $\vec{e}_{\mathrm{opt}}$ the unit polarization vector of the optical antenna mode.

In analogy the coupling rate $g_{\mathrm{IR},0}$ associated with a vibrational mode ν is linked to an effective transition dipole vector $\vec{d}_\nu$ that can be computed through numerical calculations (cf. Section 1.1). Its value is given by $g_{\mathrm{IR},0} = \frac{1}{\hbar} \vec{d}_\nu \cdot \vec{\mathscr{E}}_0$ where the electric field per photon is given by

$\vec{\mathscr{E}}_0 = \sqrt{\frac{\hbar\omega_v}{2\varepsilon_0 V_{IR}}}\vec{e}_{IR}$ with V_{IR} the mode volume and $\vec{e}_{IR}$ the unit polarization vector of the IR mode [29, 164].

Since $g^{(N)}_{IR,0}$ scales with $\sqrt{N_{IR}/V_{IR}}$, it can be independent of the mode volume as long as this volume is filled with molecules. On the contrary the interaction of the vibration with the VIS-NIR optical field $g^{(N)}_{opt,0}$ scales as $\sqrt{N_{opt}}/V_{opt}$ advocating for a device confining strongly this field and reducing thus the required optical power to reach an efficient conversion process.

The factor η_{pol} describes the local overlap between the two fields involved in our conversion scheme, on the one hand, and the IR dipole and Raman tensor of the molecular vibration, on the other hand. It is defined in the following way:

$$\eta_{pol} = \frac{\vec{e}_L \cdot \frac{\partial\vec{\mu}_v}{\partial Q_v}}{\left\| \frac{\partial\vec{\mu}_v}{\partial Q_v} \right\|} \frac{R_v^{LL}}{\|R_v\|} \tag{5.20}$$

with the label L designating the direction of the near-field at the location of the molecule. To compute $\langle\eta_{pol}\rangle$ (see Table 5.1) we numerically average η_{pol} over all possible orientations of the molecule, while keeping the IR and optical local field collinear.

From our DFT calculations we compute the molecular parameters for several cases of interest and report their values in Table 5.1. Two orientations (main axis of the molecule parallel to both local fields and fully random) were considered. Two options were also considered for the coverage: one monolayer covering the planar parts of the metallic nanostructure, or a superposition of layers filling the entire volume where the fields are localized. We use the IR/optical mode volumes $V_{IR/opt}$ (given below), the molar mass ($M = 0.1102$ kg/mol), volume density ($\rho = 1077$ kg/m^3) or surface density ($\rho_S = 6.8 \cdot 10^{18}$ m^{-2}) of thiophenol to estimate the number N_{IR} (N_{opt}) of molecules participating in the IR (optical) process.

5.4 Cavity enhanced conversion

Nanoantennae have proven to be instrumental in enhancing the interaction of molecules with off-resonant VIS-NIR optical fields (e.g. for surface-enhanced Raman scattering, SERS) [20, 167] and resonant IR fields (e.g. for surface-enhanced infrared absorption, SEIRA) [38, 168]. We now present the design of a new dual-resonant antenna (see Figs. 5.1 and 5.2) and compute the interaction of both antenna local fields with one vibrational mode of molecules covering the nanostructure. We consider that molecules are attached with their main axis perpendicular to the metallic surfaces, and extract from our DFT calculations the relevant components of the derivatives of the electronic moment and polarizability. We note that calculations for specific self-assembled monolayer orientations [169, 170] or randomly oriented molecules could also be achieved from the full knowledge of $\left(\frac{\partial\alpha_v}{\partial Q_v}\right)$ and $\left(\frac{\partial\vec{\mu}_v}{\partial Q_v}\right)$.

In our design, the incoming field to be up-converted and the pump laser field are each

Mode [cm^{-1}]	$I_v^{\mathrm{IR}}\left(\langle I_v^{\mathrm{IR}}\rangle\right)$ [km·mol^{-1}]	$R_v^{LL}\left(\langle R_v^{LL}\rangle\right)$ [Å^4·amu^{-1}]	$\eta_{pol}\left(\langle\eta_{pol}\rangle\right)$	Coverage	$g_{\mathrm{IR,0}}^{(N)}/\kappa^{\mathrm{IR}}$
mode 1002	0.52 (0.51)	2.40 (0.96)	0.33 (0.14)	monolayer	0.01
				volume	0.06
mode 1093	86.95 (28.52)	0.85 (0.31)	0.97 (0.18)	monolayer	0.17
				volume	0.75

Table 5.1 – Molecular parameters of interest for our conversion scheme for two vibrational modes of the thiophenol molecule. Calculations are obtained for a molecule oriented vertically with respect two both IR and VIS/NIR local fields (values averaged over all molecular orientations are given in parenthesis for completeness). The resulting resonant coupling terms are calculated for two different coverages of the nanostructure by the molecules and given in units of κ^{IR}.

resonant with a different component of the antenna arranged in a crossed configuration. At their intersection, the near-field polarizations of the two fields are co-linear ($\vec{e}_{\mathrm{IR}} \simeq \vec{e}_{\mathrm{opt}}$), and we obtain $\eta_{\mathrm{pol}} = 33\,\%$ for the specific vibrational mode illustrated in Fig. 5.2. Electromagnetic simulations demonstrate that the two fields, despite being more than one order of magnitude away in frequency in that particular example, are confined within a very similar volume inside the nano-gaps separating the two structures. It results in a spatial overlap of the two main electromagnetic field components within the dual antenna of $\eta_{\mathrm{mode}} = 44\,\%$ (cf. Section 1.2.4 for additional information on the design and parameter values).

From our numerical calculations we find that the antenna-assisted IR coupling rate for the vibrational mode at wavenumber $\tilde{\nu} = 1002$ cm^{-1} reaches $g_{\mathrm{IR,0}}^{(N)}/(2\pi) \sim 186$ GHz as V_{IR} is decreased by several orders of magnitude below its diffraction limit (the calculation of V_{IR} and $\vec{d}_v$ are detailed in the Appendix). As the cavity damping rate remains strong in comparison to the vacuum IR coupling rate ($2g_{\mathrm{IR,0}}^{(N)} < \kappa^{\mathrm{IR}}/2$ — Purcell regime) the antenna-enhanced damping rate for this vibrational mode can be approximated by the expression [164] : $\Gamma_v^* \simeq \Gamma_v + \kappa^{\mathrm{IR}}/2\left(1 - \sqrt{1 - (2g_{\mathrm{IR,0}}^{(N)})^2/(\kappa^{\mathrm{IR}}/2)^2}\right)$.

We show in Section 1.1 the coupling rate of another vibrational mode with a larger IR dipole moment. Under optimal molecular orientation and filling conditions, that mode is at the onset of the collective strong coupling regime with the IR antenna mode [165]. While future work is needed to properly describe this regime in the context of wavelength conversion, we note that our design offers new perspectives to realize a source of IR photons. In the strong coupling regime and under optomechanical parametric amplification [147], the optically-pumped population is shared between the collective vibrational mode and the corresponding IR antenna mode, resulting in the fast emission of IR radiations.

5.5 Optical noise contributions

A useful figure-of-merit to compare the performance of detectors independently of their respective operational bandwidth is the noise equivalent power, $\text{NEP} = P_{\text{IR}}^{\text{min,in}}/\sqrt{\text{BW}}$ [W·Hz$^{-1/2}$] where $P_{\text{IR}}^{\text{min,in}}$ is the incoming power at which the detector reaches a unity optical signal-to-noise ratio defined as $\text{SNR}(\omega) = \tilde{S}_{\text{IR}\to\text{opt}}^{\text{out}}(\omega)/\tilde{S}_{\text{opt}}^{\text{out}}(\omega)$. Equivalently, we can also calculate the NEP directly from the dark-count rate and efficiency of the device as $\text{NEP} = \frac{\hbar\omega_v}{\eta_{\text{ext}}}\sqrt{\tilde{S}_{\text{opt}}^{\text{out}}}$ [149]. Assuming noise-less detection in the visible after the upconversion scheme suggested here, the NEP of our device can be evaluated. We show the results in Fig. 5.3 as a function of the optical pump power and laser detuning from the cavity resonance. Remarkably, the NEP reaches values that improve on state of the art for commercial devices (Table 5.2) and compares favourably with more recently demonstrated uncooled platforms [171, 172] operating at the higher end of the frequency range achievable with our molecular device.

Detector type	NEP $\mathcal{O}(...)$ [W·Hz$^{-1/2}$]
Golay Cell	$\mathcal{O}(10^{-9})$
Pyroelectric	$\mathcal{O}(10^{-10})$
MCT photodiode	$\mathcal{O}(10^{-10})$
Microbolometer	$\mathcal{O}(10^{-11})$
Molecular device	$\mathcal{O}(10^{-(11..12)})$

Table 5.2 – Noise equivalent power of commercially available uncooled devices in the 5-50 THz region [145, 146] and comparison with the device presented here (Molecular device).

When operating with a pump laser red-detuned from the optical resonance $(\Delta = \omega_p - \omega_c = -\omega_v)$ in the resolved sideband regime $\kappa^{\text{opt}}/2 < \omega_v$ we can simplify the interaction of eq. 5.12 and obtain

$$\hat{H}_{\text{eff}} = -\hbar g_{\text{opt},0}^{(N)}\sqrt{\bar{n}_{\text{opt}}}\left(\delta\hat{a}_{\text{opt}}^{\dagger}\hat{b}_v + \text{h. c.}\right), \qquad (5.21)$$

This regime provides maximal efficiency and optimal NEP, as seen in Fig. 5.3(a). We note that for low vibrational frequency modes the condition $\kappa^{\text{opt}}/2 < \omega_v$ could be achieved with the help of hybrid cavities that feature narrower linewidths [32, 92].

Keeping this optimal detuning, we investigate in Fig. 5.3(b) how the NEP depends on optical pump power. As the intracavity pump photon number is increased, the efficiency initially grows linearly, while the noise remains constant, limited by the thermally generated anti-Stokes signal. This yields a square-root decrease of NEP with pump power. Interestingly, at high intracavity photon number the contribution of optomechanical quantum back-action to the dark-count rate surpasses the thermal contribution, and the NEP degrades with increasing power. This behaviour is reminiscent of the standard quantum limit for displacement

detection in optomechanical cavities.
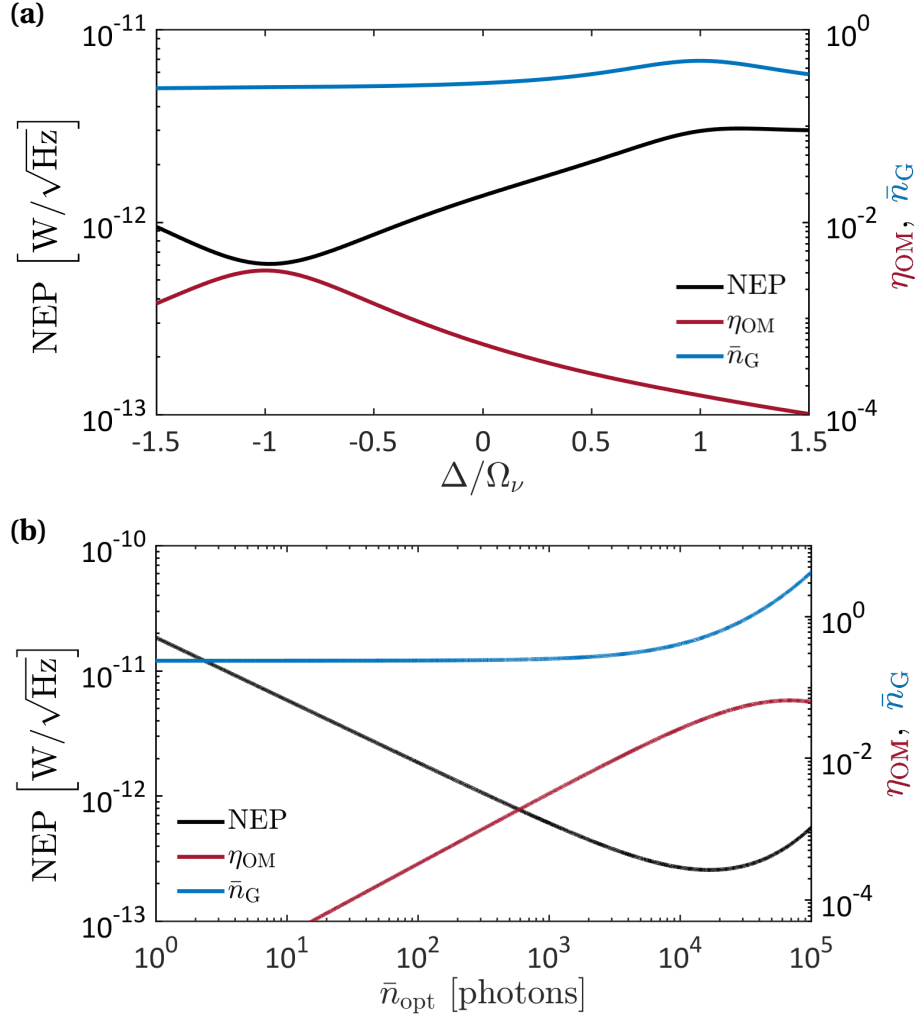
Figure 5.3 – Left axis: Noise equivalent power (NEP) (black solid line); right axis: Power dependent part of the internal conversion efficiency $\eta_{OM}(\bar{n}_{opt})$ (red solid line) and noise equivalent photon number per gate $\bar{n}_G$ (blue solid line) plotted on a logarithmic vertical scale as a function of the detuning of the optical pump laser with respect to the plasmonic resonance **(a)** for a fixed intracavity optical photon number $\bar{n}_{opt} = 1000$; and plotted as a function of intracavity optical photon number $\bar{n}_{opt}$ **(b)** for a fixed optimal red detuning $\Delta = -\Omega_\nu$. We use the parameters for the dual-antenna and molecular system described in the text.

5.5.1   Zero-temperature limit

The limit of vanishing thermal occupancy of the vibrational mode is relevant for specific applications, and it demonstrates how the backaction noise acting onto the vibration sets a fundamental lower bound on the achievable NEP of the converter. When ($\bar{n}_{th} \sim 0$) the outgoing

noise spectral density of eq. (5.16) can be simplified to

$$S_{0K}^{out}(\omega_{aS}) = \frac{2}{\pi}\eta_{opt}\frac{A^- A^+}{\left(\Gamma_v^* + \Gamma_{opt}\right)^2}. \tag{5.22}$$

Taking into account eq. (5.17) for the expression of the external conversion efficiency, the NEP and the $\bar{n}_G$ at 0 K can be calculated.

In the regime of weak optical pumping, $\Gamma_{opt} < \Gamma_v^*$, we obtain a linear scaling of $\bar{n}_G$ as a function of the intracavity photon number (appearing in the transition rates A^- and A^+) while the NEP remains constant (cf. Fig. 5.4). The value of the NEP at this plateau, which corresponds to an intrinsic quantum limit due to measurement backaction, is given by the following expression

$$NEP_{0K} = \frac{\hbar\omega_v \kappa^{IR}}{\eta_{overlap}\sqrt{\eta_{opt}}\eta_{IR}}\sqrt{\frac{A^+}{A^-}\frac{\left(\Gamma_v^* + \Gamma_{opt}\right)^{(5/2)}}{\Gamma_v^*\left(2g_{IR,0}^{(N_{IR})}\right)^2}}. \tag{5.23}$$
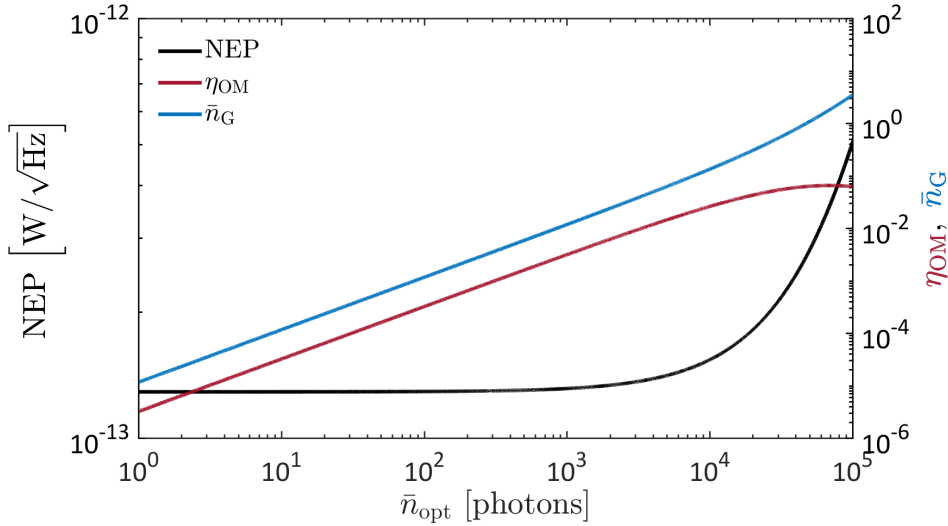
Figure 5.4 – Zero-temperature quantum limit on the NEP. Noise-equivalent power (NEP, black solid line, left axis), power-dependent part of the internal conversion efficiency (η_{OM}, red solid line, right axis) and noise-equivalent photon number per gate ($\bar{n}_G$, blue solid line, right axis) as a function of the intracavity optical photon number for $\Delta = -\omega_v$. We use the parameters for the dual-antenna and molecular system described in the text.

5.6 Advanced IR detectors

5.6.1 Single-photon detection

To assess more precisely the feasibility of operating our device in single-photon counting mode, we introduce the noise equivalent photon rate, i.e. $\tilde{S}_{opt}^{out}/\eta_{ext} \equiv |\langle\hat{a}_{IR}^{in}\rangle|^2/SNR$. This quantity corresponds to the incoming IR photon rate at the input of the device that would

generate an output rate of up-converted photons equal to the dark-count rate.

In practice, noisy single photon detectors are best operated in gated mode. In our approach this is easily realized using a pulsed optical pump laser, with a pulse duration Δt of a few ps that ideally matches the molecular vibrational linewidth; $\Delta t \simeq \left(\Gamma_v^*\right)^{-1}$. This mode of operation provides not only better noise rejection and higher intracavity photon numbers (therefore better efficiency), but also ultrafast timing resolution that is not otherwise achievable due to the intrinsic timing jitter of VIS-NIR single photon counters (typically several tens of ps) [149]. We therefore define the noise equivalent photon number per gate $\bar{n}_{\mathrm{G}} = \tilde{S}_{\mathrm{opt}}^{\mathrm{out}} / \left(\eta_{\mathrm{ext}}\Gamma_v^*\right)$ which translates the noise equivalent photon rate into an average incoming IR noise photons per time gate.
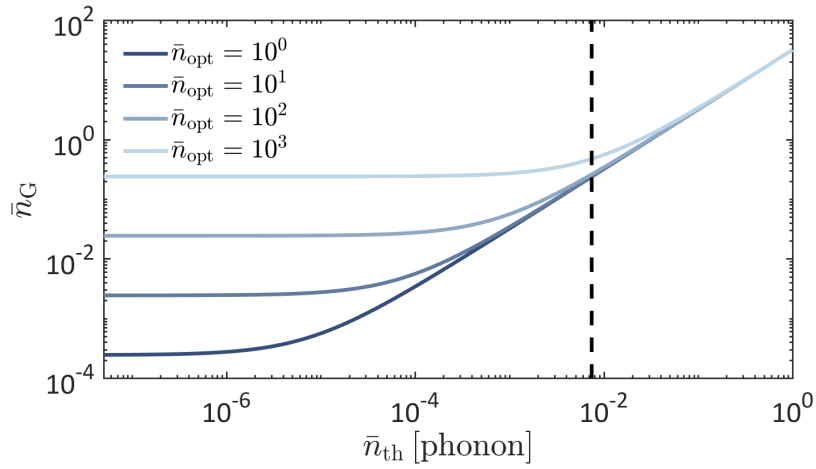
Figure 5.5 – $\bar{n}_{\mathrm{G}}$ as a function of thermal occupancy of the vibrational mode for several intracavity optical photon numbers. The dashed vertical line denotes the thermal occupancy of the mode considered in the text at room temperature.

To gain more insight on the limiting factors constraining single photon operation, we plot $\bar{n}_{\mathrm{G}}$ as a function of the thermal occupancy of the vibration and of the intracavity pump photon number in Fig. 5.5. This graph shows that even moderate cooling of the device by 100 K (easily achieved with thermo-electric cooling systems), which would bring the thermal occupancy of this vibrational mode down to $\bar{n}_{\mathrm{th}} = 5.6 \cdot 10^{-4}$, would enable to reach $\bar{n}_{\mathrm{G}} \simeq 2 \cdot 10^{-2}$, making single photon counting with ps time resolution a realistic prospect.

5.6.2 Conversion arrays

One intriguing way to additionally reduce the gated dark-count level consists in designing an array of molecular converters, sufficiently distant from each others so as not to interact by near-field coupling. We assume that the array is illuminated by spatially coherent IR signal and optical pump beam, which is easily doable due to the sub-wavelength dimensions of the antennae. The key advantage of this scheme is that the anti-Stokes signals of thermal

origin from different antennae will not exhibit any mutual phase coherence; they will add up incoherently in the far field. On the contrary, all sum-frequency anti-Stokes signals, will be phase coherent and will interfere constructively in specific directions, in analogy with a phased emitter array [173, 174].

Considering a simple linear array, this effect would jointly decrease the thermal contribution to the dark-count rate and dilute the intracavity photon number per device, enabling single photon operation with improved sensitivity.

We discuss the different contributions to the optical noise starting from the expression for $\bar{n}_f$, eq. (5.15) in the main text. When $\Gamma_{\text{opt}} \ll \Gamma_v^*$ the equation for the vibrational population splits into three different factors identified as thermal $\bar{n}_{\text{th}}$, dynamical back-action $\bar{n}_{\text{dba}}$ and quantum back-action noises $\bar{n}_{\text{qba}}$, respectively:

$$\bar{n}_f \simeq \bar{n}_{\text{th}} - \frac{\Gamma_{\text{opt}}}{\Gamma_v^*} \bar{n}_{\text{th}} + \frac{A^+}{\Gamma_v^*} \left(1 - \frac{\Gamma_{\text{opt}}}{\Gamma_v^*} \right). \tag{5.24}$$

For sensing applications it is enlightening to study how the contributions from the different noise terms are affected when considering an array of converters coherently illuminated by the IR field and the pump laser. We describe a linear array of N optomechanical converters. For simplicity we consider identical converters separated uniformly with a spacing $d < \lambda_{\text{opt}} < \lambda_{\text{IR}}$ in order to avoid multiple maxima in the radiation pattern of the array. If all converters are excited in phase, the described configuration is known as broadside configuration and the maximum radiation is directed normal to the array axis. We assume that the optical pump power is split among the antennae[1], so that the pump power per antenna is diluted according to $|\alpha^{(i)}|^2 = \frac{1}{N} |\alpha^{(0)}|^2$ so that the different cavity-assisted molecular rates scale as $\frac{1}{N}$, i.e. $A^{+/- \, (i)} = \frac{1}{N} A^{+/- \, (0)}$.

Thermal regime : If the back-action effects are weak at a single converter level $\Gamma_{\text{opt}}^{(0)} < \Gamma_v^{*,(0)}$, the power dilution leads to $\Gamma_{\text{opt}}^{(i)} \ll \Gamma_v^{*,(i)}$. The expression of the final population $\bar{n}_f$ (eq. 5.24) shows that in this case thermal noise is the main contribution to the total noise.

In the far-field, constructive interference among the fields emitted from individual antennae sharpens the pattern of coherent radiation [173] so that the total IR converted signal in this direction scales as [175] $S_{\text{IR}\to\text{opt}}^{\text{out},(N)} = (\text{array factor})^2 \cdot S_{\text{IR}\to\text{opt}}^{\text{out},(i)}$ which results in $S_{\text{IR}\to\text{opt}}^{\text{out},(N)} \simeq N^2 S_{\text{IR}\to\text{opt}}^{\text{out},(i)}$ along the direction of maximum radiation for a broadside array. On the contrary if the converters are sufficiently spaced to avoid any near field coupling the thermal emission would remain incoherent and quasi-isotropic.

We combine the factors related to the power dilution and to the directivity of the linear array

---

[1] The diffraction limit for both beams being largely different, we note that multiple converters fit under a focused IR spot. In that case the IR power per converter would not scale down.

to describe the SNR of the array in the regime dominated by thermal noise:

$$\text{SNR}^{(N)} \simeq N^2 \cdot \frac{S_{\text{IR}\to\text{opt}}^{\text{out},(i)}}{S_{\text{th}}^{\text{out},(i)}} = N^2 \cdot \frac{1}{N} \cdot \frac{S_{\text{IR}\to\text{opt}}^{\text{out},(0)}}{S_{\text{th}}^{\text{out},(0)}}. \tag{5.25}$$

Zero-temperature limit : In the case where the thermal population of the vibrational mode is negligible ($\bar{n}_{\text{th}} \sim 0$), corresponding to backaction noise dominating over thermal noise, the incoming power dilution lowers equivalently the converted signal and the output noise per antenna, so that the SNR of a sufficiently large array in this regime is given by :

$$\text{SNR}^{(N)} \simeq N^2 \cdot \frac{S_{\text{IR}\to\text{opt}}^{\text{out},(i)}}{S_{\text{ba}}^{\text{out},(i)}} = N^2 \cdot 1 \cdot \frac{S_{\text{IR}\to\text{opt}}^{\text{out},(0)}}{S_{\text{ba}}^{\text{out},(0)}}. \tag{5.26}$$

Our argument highlights the interest of this nanoscale converter to elaborate advanced architectures targeting specific applications. For example, a configuration with multiple converters within the IR spot could lead to on-chip IR multiplexing [176–179] with converters responding to multiple IR signals and bypassing the limited detection bandwidth of a single converter. This sub-wavelength platform offers novel opportunities benefiting from the coherent nature of the conversion process and opens the way for multi-spectral IR detection, IR imaging and recognition technologies.

5.6.3   Towards practical implementations of the molecular converter

In summary, we were able to treat the problem in a full quantum model, and thereby predict the internal quantum efficiency of our device, as well as its outgoing noise spectral density. The latter could be separated in two main origins: a thermal noise and a backaction noise (including quantum and dynamical backaction) that increases with pump power and eventually becomes dominant.

Extending on the room temperature measurements and on the achievable NEP values, Fig. 5.7 highlights both conversion efficiency and NEP for the case $\Delta = -\omega_v$. In this red-detuned case our model assumptions remain valid for a large range of optical intracavity photon number. At high optical power we observe that both the efficiency and NEP reach an extremal value when the back-action contribution to the outgoing noise becomes predominant as depicted in Fig. 5.6.

We would like to stress that our numerical estimates are based on a realistic nano-antenna design and a standard simple molecule (thiophenol). Although the intra-cavity photon numbers required to reach optimal performance appears to be large, they can be achieved under pulsed excitation [180]. Moreover requirements on the intra-cavity power would be lowered by further reducing the gap size (down to 1–2 nm) and, as demonstrated in Fig. 5.7, by chemical
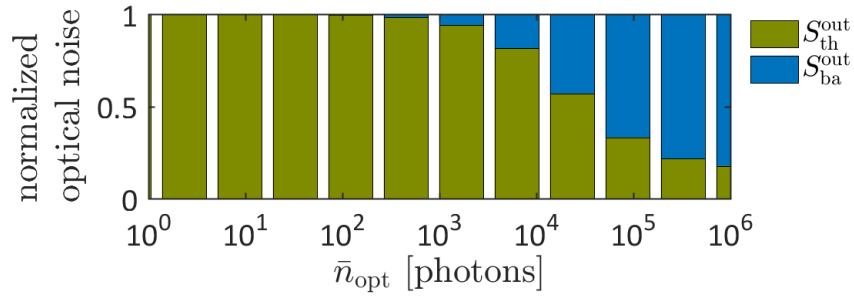
Figure 5.6 – Relative contributions to outgoing optical noise ($S_{\text{opt}}^{\text{out}}$) on the anti-Stokes sideband as a function of intracavity photon number for a pump tone red-detuned from the resonance of the optical antenna ($\Delta = -\omega_v$). The contribution from the thermal population of the vibrational mode to the dark-count rate is depicted in green and the back-action noise in blue.

engineering of the molecular converter toward higher Raman activity. All of this taken into account, this leads us to believe in possible experimental realizations of this novel kind of devices.
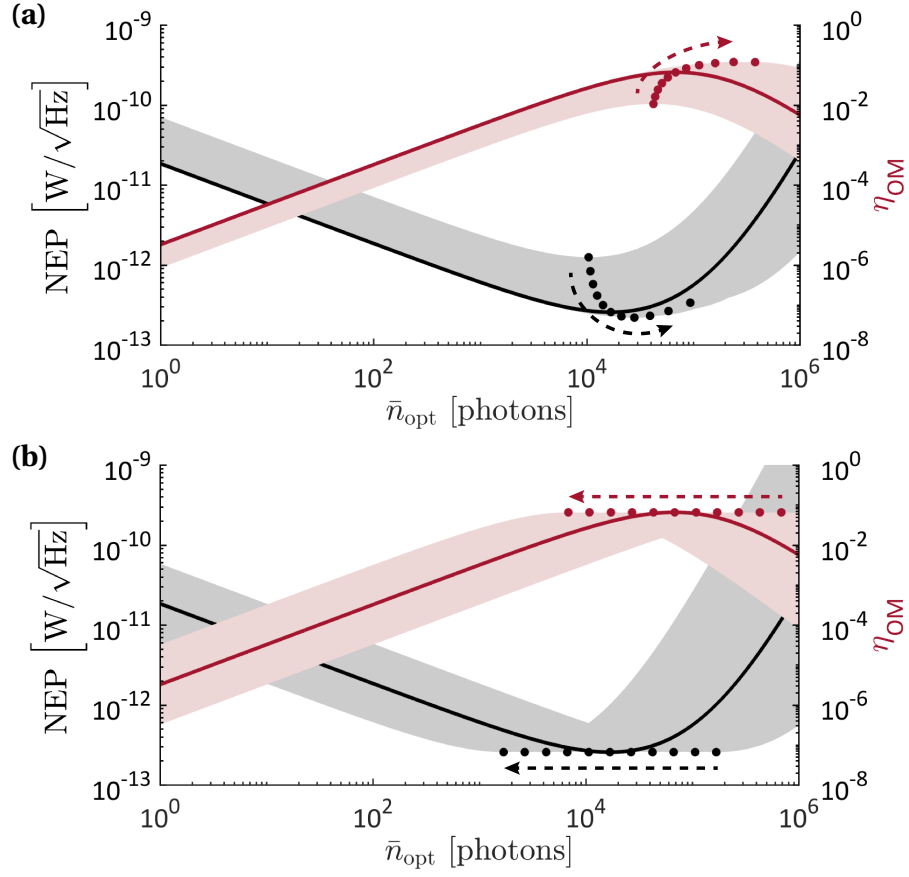
Figure 5.7 – Noise equivalent power (NEP, left axis, black solid line) and power dependent part of the internal conversion efficiency (η_{OM}, right axis, red solid line) as a function of intracavity optical photon number for $\Delta = -\omega_v$. The parameters described in the following sections of the Appendix are used to plot the lines. The dots indicate the extremal values in NEP and η_{OM} when varying the absorption intensity $[0.1{:}10] I_v^{IR}$ in **(a)** or the Raman activity $[0.1{:}10] R_v^{LL}$ in **(b)**. The colored areas denote the NEP and η_{OM} achievable when sweeping either parameters and the dashed arrows indicate the direction of evolution of the extremum when increasing the parameters value.

A List of symbols

Notation	Description
$\omega_p/2\pi$	Frequency of the optical pump tone
$\omega_{\mathrm{IR}}/2\pi$	Resonance frequency of the IR antenna mode
$\omega_c/2\pi$	Resonance frequency of the optical antenna
$\kappa_0/2\pi$	Rate of intrinsic losses, including absorption and uncoupled radiation
$\kappa_{\mathrm{ex}}/2\pi$	Coupling rate between the antenna field and an incoming/outgoing field
$\kappa = \kappa_0 + \kappa_{\mathrm{ex}}$	Total decay rate of a plasmonic antenna
$\eta_{(\mathrm{IR/opt})}$	Coupling ratio $\left(\kappa_{\mathrm{ex}}^{(\mathrm{IR/opt})} / \kappa^{(\mathrm{IR/opt})} \right)$
η_{overlap}	Overlap between the two electromagnetic and the vibrational modes
$\Gamma_{\mathrm{opt}}/2\pi$	Optomechanical damping rate with $\Gamma_{\mathrm{opt}} = A^- - A^+$
$\Gamma_\nu/2\pi$	Intrinsic damping rate of the vibrational mode ν
$\Gamma_\nu^*/2\pi$	Cavity/Antenna-assisted damping rate of the vibrational mode ν
$\omega_\nu/2\pi$	Mechanical frequency of the vibrational mode ν
V_{opt}	Volume of the optical resonant mode
V_{IR}	Volume of the IR resonant mode
x_ν	Displacement coordinate of the vibrational mode ν
m_ν	Effective mass of the vibrational mode ν

Appendix A. List of symbols

Notation	Description
$x_{\mathrm{zpm},\nu}$	Zero-point motion of the vibrational mode ν
$\bar{n}_{\mathrm{opt}}$	Average occupation of the optical cavity/antenna mode
$\bar{n}_{\mathrm{IR}}$	Average occupation of the IR cavity/antenna mode
$\bar{n}_f$	Final occupation of the vibrational mode
$\bar{n}_{\mathrm{th}}$	Average phonon number in thermal equilibrium $\bar{n}_{\mathrm{th}} = (e^{\hbar\omega_\nu/k_B T} - 1)^{-1}$
$\bar{n}_{\mathrm{b}}^{\mathrm{IR}}$	Average phonon population driven by the IR tone
$\Delta = \omega_p - \omega_c$	Laser detuning from the optical antenna resonance
$G_\nu/2\pi$	Coupling rate between the plasmon and the vibrational mode ν
$g_{\mathrm{opt},0}/2\pi$	Optomechanical vacuum coupling rate
$\tilde{S}^{\mathrm{out}}$	Outgoing photon flux [photon/s]
$\hat{a}^{\mathrm{in}}$	Input field normalized so that $|\langle\hat{a}^{\mathrm{in}}\rangle|^2$ is the incoming photon flux [photon/s].

90

B DFT analysis of vibrational modes

Many equivalent platforms exist in order to perform DFT calculations and retrieve information on the vibrational modes of complex molecules and their electronic properties. In our case we use the software named GAUSSIAN [1] to extract and analyze various parameters. The geometry is first constructed with the help of AVOGADRO [2]. From this first optimization of the geometry of the molecule of interest we then adapt the orientation of the molecule with a built-in script in order to align one characteristic axis of the molecule with the coordinate frame. The GAUSSIAN simulations are then performed using a functional B3LYP/6-311++G(d,p) base. The calculations are performed without enabling any rotation of the coordinate frame and with an increased number of output digits so that rotations and projections along specific axes of electronic properties of the molecule can be reliably calculated from a single DFT calculation. Usually,

Using the harmonic calculations of the frequencies only, we will usually have to use a scaling factor to make the results compatible with experimental ones. We used again AVOGADRO to visualize the active vibrational modes and their corresponding energy.

The procedure is well described in the context of Raman calculations in the book of Le Ru & Etchegoin [3]. For completeness we reproduce here several expressions enabling the reconstruction of the normal modes properties of the molecule from a GAUSSIAN output file and their use in the evaluation of the orientation dependent spectra of absorption and scattering experiments. We illustrate the richness of the DFT results with the example of another molecule of interest (GBT). Finally we comment shortly on an additional aspect that can be investigated with the help of DFT calculations and that could be instrumental in the development of optical schemes involving ensembles of molecules : anharmonicities of vibrational modes.

---

[1] http://www.gaussian.com/
[2] http://avogadro.openmolecules.net/wiki/Main_Page

B.1 Reconstruction and projection of normal modes electronic properties

In GAUSSIAN, all the gradient terms are given with respect to the usual cartesian coordinates and for each atom. We define as ξ_k^n the displacement of an atom along the n-th Cartesian coordinate (number of displacements = 3 x number of atoms) for the normal mode k. Each displacement inside a specific mode k can be weighted by a factor defined as :

$$(\phi_k^n)_{n=1,\dots,3N} = \frac{\xi_k^n}{\sqrt{\sum_{l=1}^{3N}(\xi_k^l)^2}} \tag{B.1}$$

Extracting these displacements and the mass of the different atoms, we can transform the gradient quantities obtained from the DFT calculations into the one described in Section 1.1. For example, in the case of the Raman tensor we obtain :

$$\frac{\partial \alpha_v}{\partial Q_v} = \frac{1}{\sqrt{\mu_k}} \sum_{n=1}^{3N} \phi_k^n \left(\frac{\partial \alpha_v}{\partial x^n} \right) \tag{B.2}$$

where the reduced mass μ_k of the normal mode k is described by the expression:

$$\mu_k = \sum_{n=1}^{3N} m^n (\phi_k^n)^2 \tag{B.3}$$

with m^n the mass of the $\frac{n}{3} + \left(1 - \frac{n \bmod d}{d}\right)$ atom weighted by the adimensional displacement factor ϕ_k^n.

Then the obtained tensor can be transformed by a simple rotation operation :

$$\left(\frac{\partial \alpha_v}{\partial Q_v} \right)' = T \left(\frac{\partial \alpha_v}{\partial Q_v} \right) T^{-1} \tag{B.4}$$

in order to evaluate the Raman activity of the molecule in any specific orientation. In the convenient case of SERS the incoming and outgoing fields can be assumed locally to be collinear. The resulting symmetry disminishes the number of possible outcomes when projecting the rotated tensor on the fields axis and reduces thus the dimensionality of the orientation space.

For the IR coupling case, the same treatment can be applied for the vector constituted from the electric dipole derivatives and can simply be rotated according to $\left(\frac{\partial \vec{\mu}_v}{\partial Q_v} \right)' = T \left(\frac{\partial \vec{\mu}_v}{\partial Q_v} \right)$ in order to orient the molecule in any possible direction with respect to the axis of projection.
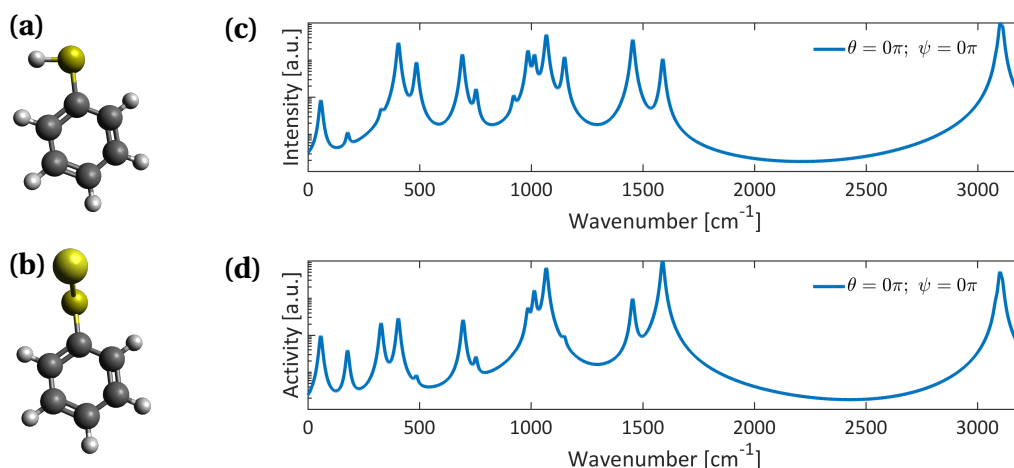
Figure B.1 – Illustrations of the thiophenol **(a)** and GBT **(b)** molecules. Calculated IR **(c)** and Raman **(d)** spectra. The intensities and activities of the different vibrational modes are represented on a logarithmic scale. The modes profiles are represented by Lorentzians with a fixed ad hoc linewidth of 15 cm^{-1}.

B.2   Extended DFT study of GBT

For completeness we add here the main DFT results for the other molecule discussed along this thesis, namely GBT. In the thesis, the name thiophenol can be used in order to describe the molecule before SAM assembly on the gold substrate (illustration in Fig. B.1a). When assembled in a SAM the initial molecule binds to the gold substrate by creation of a gold-sulfur bond and gives way to GBT (illustration in Fig. B.1b). The resulting electronic properties of this layer are thus better described by DFT simulations of this later molecule. The corresponding spectra are depicted in Fig. B.1c-d.

Fig. B.3 illustrates in two different spectral ranges the sensitivity of Raman active modes to the specific orientation of the molecule (a similar dependence can be observed for IR measurements, Fig. B.2). Without loss of generality we chose the coordinate frame so that the main axis of the GBT molecule is parallel to both the z-axis and the local field and so that θ describes a rotation of the molecule around the x-axis and ψ a rotation around the main axis of the molecule.

B.3   A note on anharmonicities of vibrational modes

The vibrational modes of a molecule can usually not be considered alone. First it should be noted that the molecule is subject rotational modes that are described by: $E(J)_n = \hbar B_n J(J+1)$, with J a rotational quantum number and B_n a factor depending through the moment of inertia on the vibrational quantum number. This expression already shows that such modes cannot be expressed as harmonic even for small displacements. In this work we neglected these contributions as Raman experiments did not observe any contribution due to these modes.

(a)

(b)

Figure B.2 – **(a-b)** Calculated IR intensities for two different ranges of vibrational frequencies and for a subset of possible molecule orientations. The modes profiles are represented by Lorentzians with a fixed ad hoc linewidth of 15 cm^{-1}. The configuration $\theta = 0.5\pi$, $\psi = 0\pi$ depicts a local electric field perpendicular to the main plane of the molecule.

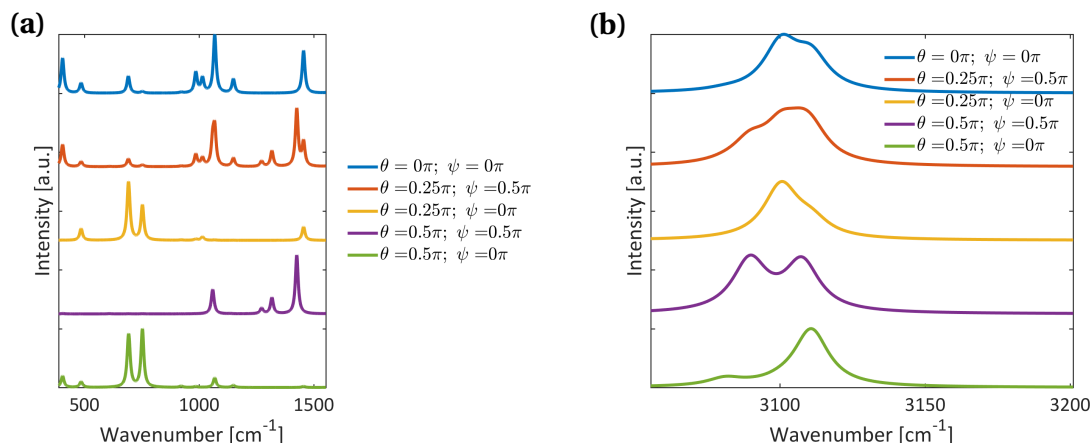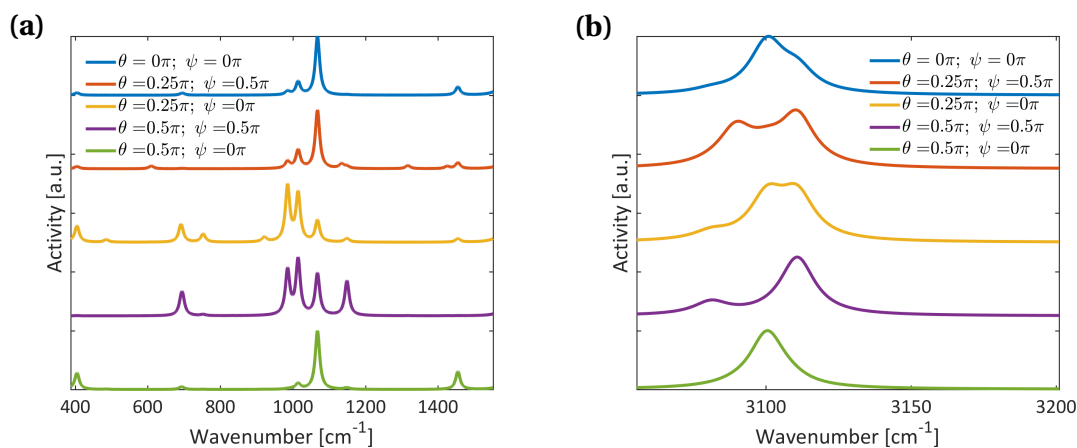**(a)**

(b)

Figure B.3 – **(a-b)** Calculated Raman activities for two different ranges of vibrational frequencies and for a subset of possible molecule orientations. The modes profiles are represented by Lorentzians with a fixed ad hoc linewidth of 15 cm^{-1}. The configuration $\theta = 0.5\pi$, $\psi = 0\pi$ depicts a local electric field perpendicular to the main plane of the molecule.

Moreover, we have considered molecules featuring no electronic transition in the optical range in order to avoid the expression of a possible enhancement of the optical coupling through a resonant coupling to the electronic mode of the molecule. This assumption made possible the development of the polarizability derivatives through what is known as the Plaszek model. todoword on resonant Raman case

So, we only consider here the role of possible non-linearities of the vibrational modes of a single molecule. Related anharmonicities could of course depend on the environment like for example on its linkage to the metallic substrate akin other quantities discussed in this thesis. These questions should be adressed by follow-up studies where the environment can be modeled in the calculations. Nevertheless,even considering only these modes, the harmonic approximation is not a priori valid for all the modes and the validity of this approximation could be tested numerically.

Some experimentally observable effects would indeed not be describable with a simple harmonic potential. For example, the finite energy needed to break a bond cannot be explained by a harmonic description. The importance of the anharmonicity can already be appreciated with a simple and naive case of study : breaking of an OH bond of a water molecule. The well depth (D_e) can be computed from the difference between the dissociation energy (D_0) and the zero point energy of the molecule (E_0) (experimental values : $D_0 \sim 5$ eV and $E_0 \sim 0.2$ eV). The vibrational energy level associated within the harmonic approximation to the ~ 3500 cm^{-1}vibrational mode of water is around 0.4 eV. So, the occupation of this mode would be limited to ~ 12 phonons. This first intuitive limit on the number of phonons that can be introduced in the molecule without breaking it is usually modified by introducing anharmonic terms in the molecular potential and would benefit from a numerical estimate for the case where experimental data cannot easily be obtained.

In fact, the vibrational potential can in a better approximation be described by a Morse potential and will have non null contributions from anharmonic terms. The shape of this potential is skectched in Fig. B.4 (a). The potential is thus well approximated by a harmonic potential for small displacements or for small occupation numbers but, as the amplitude increases, anharmonicities will become predominant. For example, the term related to the Coulomb interaction between atoms can no more will no more be negligible. DFT calculations could thus be instrumental to evaluate the factor describing this anharmonicity and to estimate the range over which the harmonic assumption is acceptable.

Solving the Schrödinger equation for the Morse potential, we are able to write the vibrational energy levels as [181]:

$$E(n) = \hbar \left[\omega_v \left(n + \frac{1}{2} \right) - \frac{\hbar \omega_v}{4 D_e} \omega_v \left(n + \frac{1}{2} \right)^2 \right] \tag{B.5}$$

We thus introduce the quantity $\chi_v \equiv \frac{\hbar \omega_v}{4 D_e}$, a dimensionless factor describing the anharmonicity
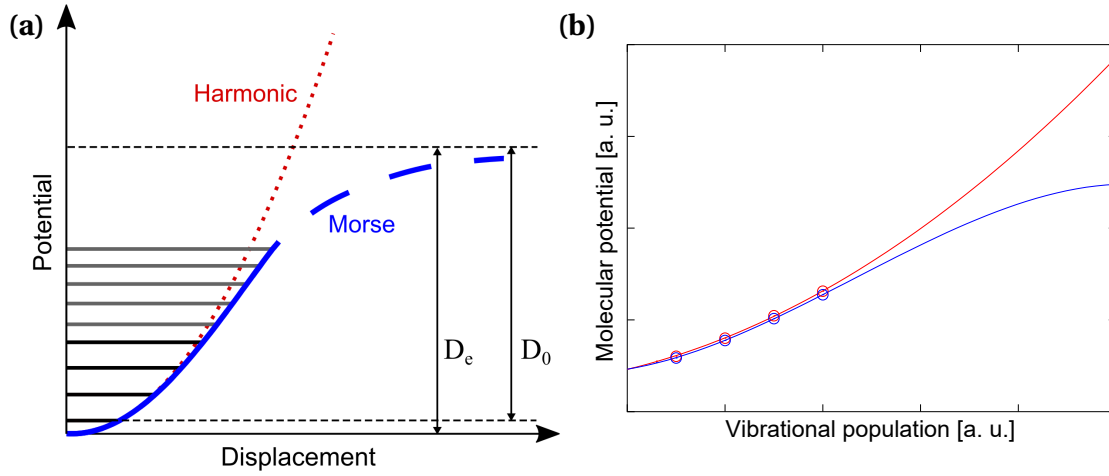
Figure B.4 – **(a)** Morse potential illustration **(b)** DFT calculation of the molecular potential of a thiophenol vibrational mode in the harmonic approximation (red) and with an additional anharmonic contribution (blue) depending on the population of the mode. The dots indicate the energy levels of the vibration for the different approximations of its potential.

included in the Drude model. The description induced by the Morse potential can be seen to be valid up to an occupation number n_m where the difference in energy between two adjacent vibration levels become negative:

$$E_v(n+1) - E_v(n) = \hbar[\omega_v - (n+1)\frac{\chi_v \omega_v}{2} \leq 0] \quad \Rightarrow n_m = \frac{2-\chi_v}{\chi_v}$$

The DFT simulation software GAUSSIAN is able to go beyond the harmonic calculations and estimate this anharmonicity factor. In order to compute the correction terms, the software derives numerically the Hessian matrix of the molecular potential by computing its value for small displacements around its minimum. This method called second-order perturbative approach is able to get third order and some fourth order derivatives of the potential with respect to the normal modes [182]. The Morse potential can be well approximated taking into account some of these additional terms (B.4) (b) and the relative weight of the anharmonic contributions to the molecular potential can be evaluated more precisely.

In this model the modes are considered as independant si that the anharmonicities appear in a single mode fashion. It should however not be forgotten that the different modes are in fact slightly coupled to the others through these anharmonic terms; a phenomenon known as intramolecular vibrational relaxation (IVR). Follow-up studies may consider adding these anharmonic terms in an extended description of the vibration-plasmon interaction.

C Focal fields of patterned beams

In this appendix we propose to summarize the calculations needed to represent the focal fields of various patterned beams. A detailed treatment of the question can be found in textbooks [183]. Here we simply introduce the framework necessary to handle these patterned beams and highlight two experimentally interesting cases.

C.1 Angular spectrum representation of the focal field

The angular spectrum representation enables to derive how a field propagate knowing its distribution on a specific plane. Starting from the Fourier transform of the optical field on a specific plane it is possible to demonstrate that the field near the focus of an ideal spherical lens can be calculated from the field distribution after the lens (far-field) :

$$\vec{E}(\rho, \varphi, z) = \frac{ikf e^{-ikf}}{2\pi} \int_0^{\theta_{\max}} \int_0^{2\pi} \vec{E}_{\mathrm{f-f}}(\theta, \phi) e^{ikz\cos\theta} e^{ik\rho\sin\theta\cos(\phi-\varphi)} \sin\theta \mathrm{d}\phi \mathrm{d}\theta \tag{C.1}$$

where f is the focal length and where the integration over θ is limited by the numerical aperture of the lens $\theta_{\max} = \mathrm{NA}\sin\theta_{\max}$. The field in the focus can thus be calculated from a double integral of different rays each represented by a specific plane wave. In place of the more familiar Cartesian coordinates where the role of the spatial frequencies $(k_x,\ k_y,\ k_z)$ clearly appear, the spectrum representation is here given in spherical coordinates due to the symmetry of the imaging system. Mapping the two coordinate frames immediatly after the lens enables to express the far-field in terms of the incoming field distribution :

$$\vec{E}_{\mathrm{f-f}}(\theta, \phi) = \frac{1}{2} E_{\mathrm{inc}}(\theta, \phi) \begin{bmatrix} (1+\cos\theta) - (1-\cos\theta)\cos(2\phi) \\ -(1-\cos\theta)\sin(2\phi) \\ -2\cos\phi\sin\theta \end{bmatrix} \sqrt{\frac{n_1}{n_2}\cos\theta} \tag{C.2}$$

with n_1, n_2 the indices of refraction of the medium before and after the lens. The expression after the bracket insures that the energy flux carried by each plane wave is conserved. The

(a)

(b)

(c)

(d)

Figure C.1 – Electric field intensity distribution in the focal plane of an incoming x-polarized Gaussian beam (air-immersed objective, NA=0.95, 50x). Total electric field intensity $|\vec{E}|^2$ in **(a)**, and its individual components: $|E_z|^2$ in **(b)**, $|E_x|^2$ in **(c)** and $|E_y|^2$ in **(d)**. We assumed a unity filling factor and a beam wavelength of 750 nm. The intensity is normalized by the intensity of the incident beam.

incoming field distribution of the familiar Gaussian field is given by :

$$E_{\text{inc},(0,0)}(\theta,\phi) = E_0 e^{-\frac{f^2 \sin^2\theta}{w_0^2}} = E_0 f_w \tag{C.3}$$

with w_0 the beam waist of the Gaussian beam. The factor f_w can be rexpressed in terms of the relevant parameter known as filling factor that describes how the incoming beam fills the back-aperture of the lens $f_0 = w_0 / \left(f \sin\theta_{\text{max}} \right)$:

$$f_w = e^{-\frac{\sin^2\theta}{f_0^2 \sin^2\theta_{\text{max}}}} \tag{C.4}$$

Interestingly this mode constitutes only the fundamental (zeroth order) solution of several families of modes that are solutions of the Helmoltz equation. The two additional modes we are interested in (radially polarized (RP) and azimuthally polarized (AP) modes) are simple
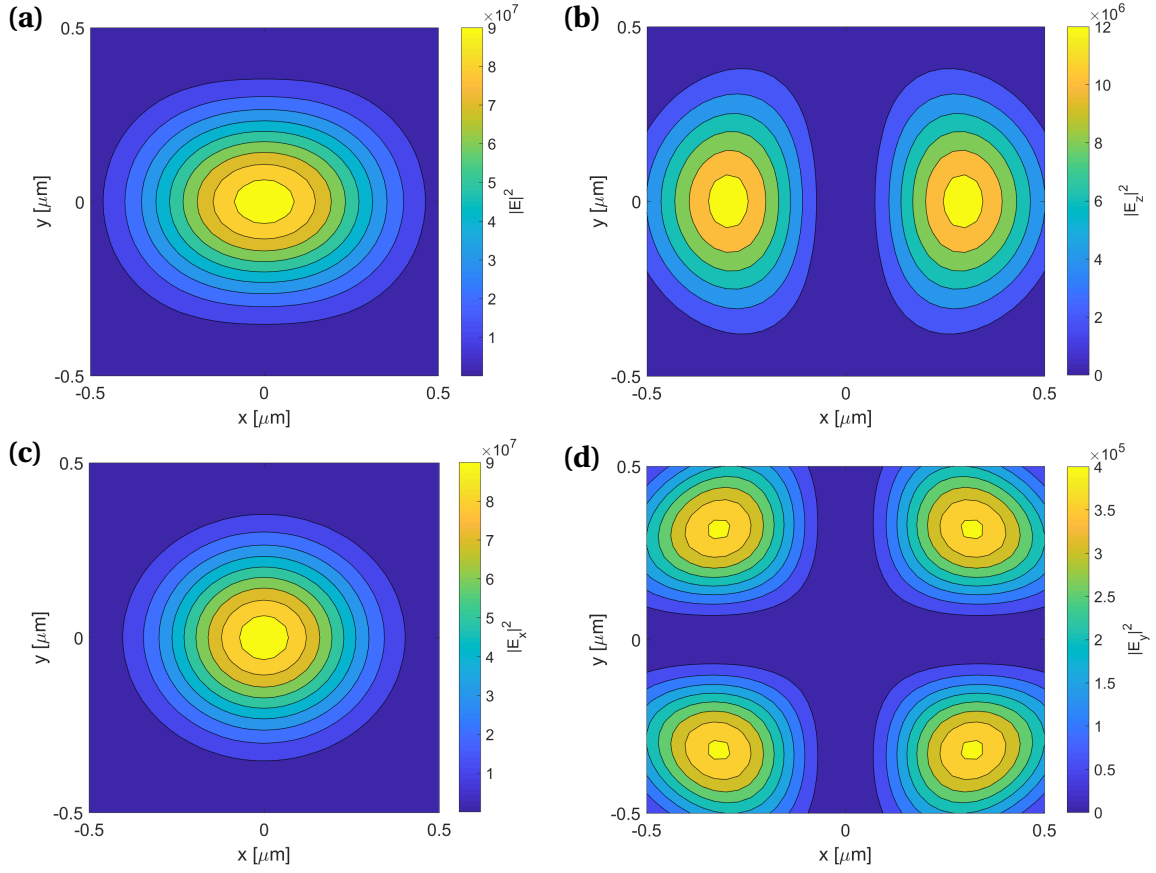
Figure C.2 – Electric field intensity distribution in the focal plane of an incoming radially polarized beam (air-immersed objective, NA=0.95, 50x). Total electric field intensity $|\vec{E}|^2$ in **(a)**, and its individual components: $|E_z|^2$ in **(b)**, $|E_x|^2$ in **(c)** and $|E_y|^2$ in **(d)**. We assumed a unity filling factor, a beam wavelength of 750 nm and an imbalance ratio of 1.5. The intensity is normalized by the intensity of the incident beam.

superpositions of first order modes of the Hermite-Gaussian set of solutions. For example the incoming field distribution of one of the mode HG$_{10}$ is given by :

$$E_{\text{inc},(1,0)}(\theta,\phi) = \frac{2E_0 f}{w_0} \sin\theta \cos\phi f_w \tag{C.5}$$

One of the integration can be calculated analytically with the help of the Bessel functions J_n. So the evaluation of each field point necessitates the calculation of some of the following

integrals :

$$I_{00} = \int_0^{\theta_{\max}} f_w \left(\cos\theta\right)^{1/2} \sin\theta \left(1 + \cos\theta\right) J_0\left(k\rho\sin\theta\right) e^{ikz\cos\theta} d\theta \tag{C.6}$$

$$I_{10} = \int_0^{\theta_{\max}} f_w \left(\cos\theta\right)^{1/2} \sin^3\theta \, J_0\left(k\rho\sin\theta\right) e^{ikz\cos\theta} d\theta \tag{C.7}$$

$$I_{01} = \int_0^{\theta_{\max}} f_w \left(\cos\theta\right)^{1/2} \sin^2\theta \, J_1\left(k\rho\sin\theta\right) e^{ikz\cos\theta} d\theta \tag{C.8}$$

$$I_{11} = \int_0^{\theta_{\max}} f_w \left(\cos\theta\right)^{1/2} \sin\theta \left(1 + 3\cos\theta\right) J_1\left(k\rho\sin\theta\right) e^{ikz\cos\theta} d\theta \tag{C.9}$$

$$I_{02} = \int_0^{\theta_{\max}} f_w \left(\cos\theta\right)^{1/2} \sin\theta \left(1 - \cos\theta\right) J_2\left(k\rho\sin\theta\right) e^{ikz\cos\theta} d\theta \tag{C.10}$$

$$I_{12} = \int_0^{\theta_{\max}} f_w \left(\cos\theta\right)^{1/2} \sin^2\theta \left(1 - \cos\theta\right) J_1\left(k\rho\sin\theta\right) e^{ikz\cos\theta} d\theta \tag{C.11}$$

$$I_{13} = \int_0^{\theta_{\max}} f_w \left(\cos\theta\right)^{1/2} \sin^3\theta \, J_2\left(k\rho\sin\theta\right) e^{ikz\cos\theta} d\theta \tag{C.12}$$

$$I_{14} = \int_0^{\theta_{\max}} f_w \left(\cos\theta\right)^{1/2} \sin^2\theta \left(1 - \cos\theta\right) J_3\left(k\rho\sin\theta\right) e^{ikz\cos\theta} d\theta \tag{C.13}$$

With the help of these abbreviations the focal field of an incoming fundamental Gaussian beam linearly polarized along x can finally be expressed as

$$\vec{E}_{(0,0,x)} = \frac{ikf}{2}\sqrt{\frac{n_1}{n_2}} E_0 e^{-ikf} \begin{bmatrix} I_{00} + I_{02}\cos\left(2\phi\right) \\ I_{02}\sin\left(2\phi\right) \\ -2iI_{01}\cos\phi \end{bmatrix} \tag{C.14}$$

The intensity distributions of the different field components in the focal plane are shown in Fig. C.1. The total field intensity is dominated by its in-plane component parallel to the incoming polarization while its out-of-plane component is zero along the whole optical axis and shows two side lobes with opposite phases.

C.2 Unbalanced contributions of higher order modes

Experimentally several optical elements will transmit differently two fields with different polarizations. Additionally the higher order mode might be difficult to identify and could benefit from an extra polarizer in order to remove lower order contributions. It is thus desirable to take into acount the resulting polarization imbalance in the modellisation of the focal fields.
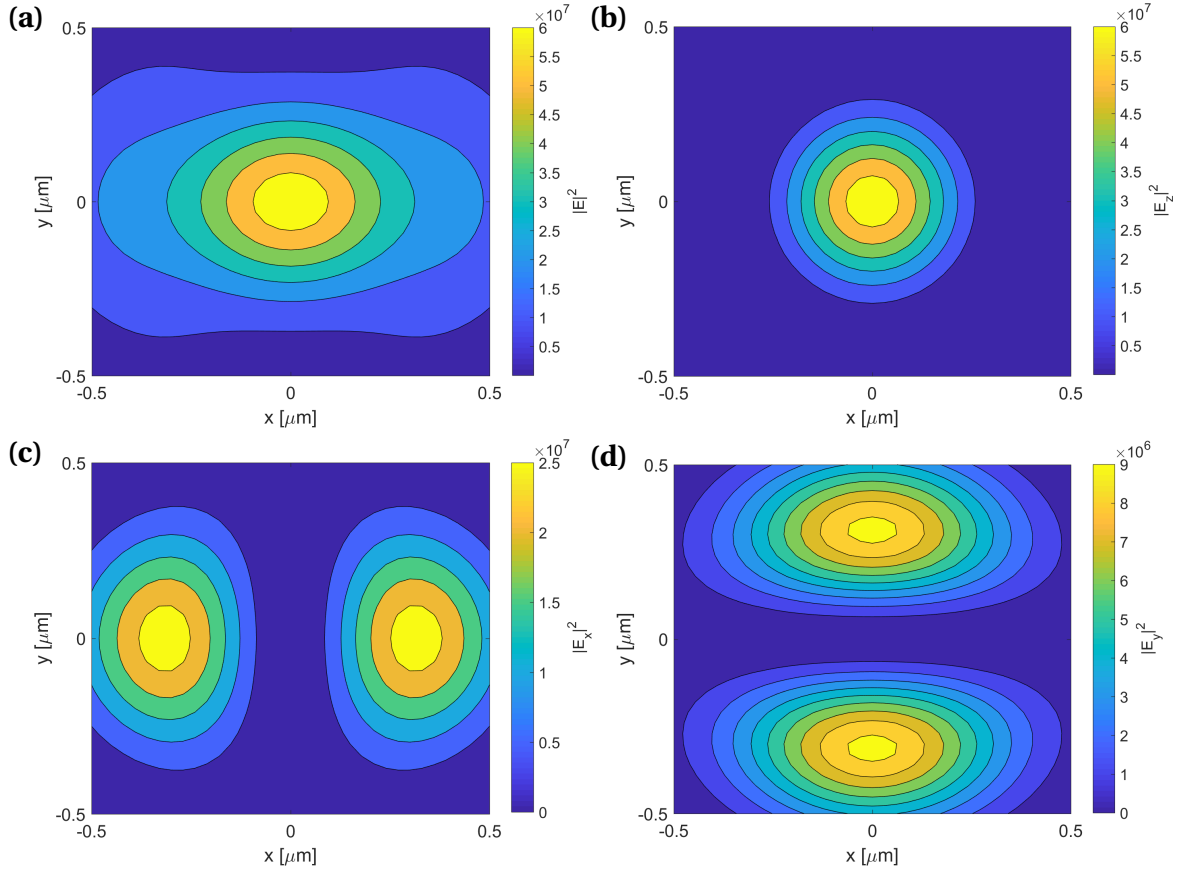
Figure C.3 – Electric field intensity distribution in the focal plane of an incoming radially polarized beam (air-immersed objective, NA=0.95, 50x). Total electric field intensity $|\vec{E}|^2$ in **(a)**, and its individual components: $|E_z|^2$ in **(b)**, $|E_x|^2$ in **(c)** and $|E_y|^2$ in **(d)**. We assumed a unity filling factor, a beam wavelength of 532 nm and a imbalance ratio of 100. The intensity is normalized by the intensity of the incident beam.

This imbalance can be introduced in a simple modification of the higher order mode. For example, in the case of a radially polarized beam, we could write :

$$\mathrm{RP}_{(\eta)} = \mathrm{HG}_{10}\,\vec{n}_x + \frac{1}{\eta}\mathrm{HG}_{10}\,\vec{n}_y, \tag{C.15}$$

with η the imbalance ratio between two orthogonal polarization components and the Hermite-Gaussian first-order beams HG_{10} polarized along two different axes.

The electric focal field of $\mathrm{HG}_{10}\,\vec{n}_x$ is given by :

$$\vec{E}_{(1,0,\mathrm{x})} = \frac{ikf^2}{2w_0}\sqrt{\frac{n_1}{n_2}}E_0 e^{-ikf} \begin{bmatrix} i\mathrm{I}_{11}\cos(\phi) + i\mathrm{I}_{14}\cos(3\phi) \\ -i\mathrm{I}_{12}\sin(\phi) + i\mathrm{I}_{14}\sin(3\phi) \\ 2\left(-\mathrm{I}_{10} + \mathrm{I}_{13}\cos(2\phi)\right) \end{bmatrix} \tag{C.16}$$

101

The electric focal field of $HG_{10}\,\vec{n}_y$ is given by :

$$\vec{E}_{(1,0,y)} = \frac{ikf^2}{2w_0}\sqrt{\frac{n_1}{n_2}}E_0 e^{-ikf}\begin{bmatrix} -i\mathrm{I}_{12}\cos\left(\phi\right) - i\mathrm{I}_{14}\cos\left(3\phi\right) \\ i\mathrm{I}_{11}\sin\left(\phi\right) - i\mathrm{I}_{14}\sin\left(3\phi\right) \\ 2\left(-\mathrm{I}_{10} - \mathrm{I}_{13}\cos\left(2\phi\right)\right) \end{bmatrix} \qquad (\text{C.17})$$

The intensity distributions of the different field components in the focal plane and for different imbalance ratios are shown in Fig. C.2 ($\eta = 1.5$) and Fig. C.3 ($\eta = 100$). The longitudinal component in focus is significantly stronger than the one obtained with an incoming Gaussian beam. The transverse component on its side shows the characrteristic zero value along the optical axis and 180° out of phase lobes of a doughnut mode.

An increase of the imbalance ratio reduces the strength of the longitudinal and the in-plane perpendicular to the incoming polarization components so that the contribution to the total intensity of the electric field of the component parallel to the incoming polarization is increased.

C.3   Additional tailoring of the out-of-plane component

One interesting option to modify further the out-of-plane to in-plane ratio of the electric field in the focal plane can be reached by adding a beam stop in the optical path [106]. When centered on the optical path and located in the Fourier plane the obscuring element is well described by a slightly modified angular representation :

$$\vec{E}(\rho,\varphi,z) = \frac{ikf e^{-ikf}}{2\pi}\int_{\theta_{\min}}^{\theta_{\max}}\int_0^{2\pi}\vec{E}_{\mathrm{f-f}}(\theta,\phi)e^{ikz\cos\theta}e^{ik\rho\sin\theta\cos(\phi-\varphi)}\sin\theta\,\mathrm{d}\phi\mathrm{d}\theta \qquad (\text{C.18})$$

with $\theta_{\min} = \arcsin\left(D_{\mathrm{bs}}/D_{\mathrm{obj}}\mathrm{NA}\right)$ where D_{bs} and D_{obj} are the diameters of the beam stop and objective respectively.

Fig. C.4 shows that in situations where a larger longitudinal contribution is needed (coupling of other components to the structure parasiting the signal, heating) the simple addition of a beam stop can be beneficial. At the price of reducing the amount of power reaching the nanostructure, the contribution of the longitudinal component to the field intensity in the focal plane can be enhanced by one order of magnitude.
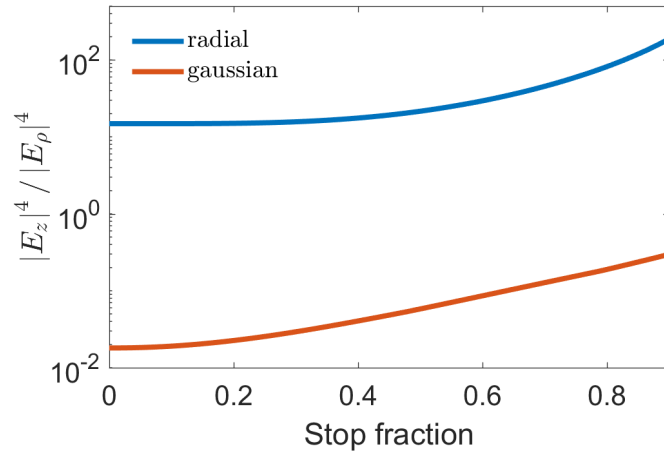
Figure C.4 – Maximum of $|E_z|^4 / |E_\rho|^4$ in the focal plane for a gaussian and a radial laser beams in logarithmic scale as a function of the fraction of the back-aperture of the objective obscurated by the beam stop.

D Experimental setup
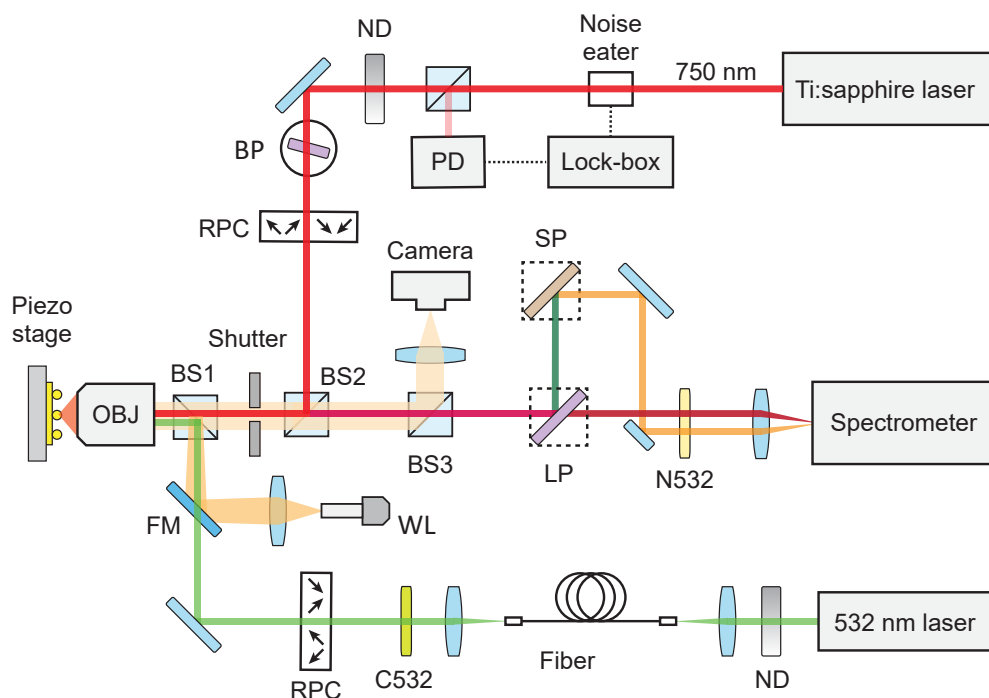
Figure D.1 – Schematic of experimental setup. **ND:** neutral density filter, **FM:** flip mirror, **BP:** tunable band pass filter, **RPC:** radial polarization converters, **PD:** photodetector, **WL:** white light source, **BS1:** beamsplitter with reflection:transmission in % (R:T) = 10:90, **BS2:** beamsplitter with R:T = 20:80, **BS3:** flip pellicle beamsplitter with R:T = 8:92, **LP:** AHF tunable longpass filter module, **SP:** AHF tunable shortpass filter module, **N532:** notch filter centered at 532 nm, **C532:** clean up filter centered at 532 nm, **OBJ:** Nikon objective, numerical aperture = 0.95, working distance = 0.21 mm, **Spectrometer:** Andor Shamrock, grating: 300 l/mm, ccd: Andor iDus 416, **Tunable Ti:Sa laser:** Coherent MBR.

Stabilization of laser power : We use different tools in order to stabilize, adjust and keep track of the Ti:sa laser power during acquisition times and over the full spectral range of the

device (700-800 nm without optical changes of the laser cavity). The power entering the confocal inverted microscope is stabilized through a feedback loop based on a commercial variable attenuator (Noise eater, Thorlabs) constituted of a liquid crystal wave plate and a polarizer. For improved performance we control the feedback loop externally with an amplified photodetector and a servo-controller (Newport). The power is then adjusted over a dynamic range of 40 dB with the help of a motorized neutral density wheel and recorded continuously during the measurements for minor post-measurements adjustments.

Polarization control : We use one liquid crystal device (ARCoptix) to control the polarization of each of our laser tones. The higher order mode is obtained after careful suppression of lower order contributions through a spatial filter. A beam profiler (Thorlabs) is then used to analyze the profile of the mode. The green laser path is duplicated in order to switch easily between linearly, radially and azimuthally polarized beams.

Sample scanning and auto-focusing : We use a combination of a motorized micro- and nanos-tage (Mad City Labs) to identify a region of interest on the sample and automatically scan 50x50 μm area to identify and store the hot-spots locations. A script also enables the automatized readjustment of the sample position to optimize the level of signal and compensate for possible temporal drifts of the sample.

Dual sideband measurements : In order to extract the effective temperatures of the nanojunction our setup is able to read both sidebands simultaneously. The sidebands are separated by successive tunable edge filters (Semrock). The wavelength tuning is motorized (Tunecube, AHF) and enables the control of both reflected and transmitted paths with a certain flexibilty on the spectral range : This range is mostly limited by the mechanical displacements restrictions of the cube and by the angle-dependent quality of the reflected component of the beam on the edge filter. The two resulting optical paths are finally vertically superimposed before the spectrometer slit before being focused on different lines of the CCD.

D.1   Characterization of setup noise

In order to characterize the photoluminescence fluctuations, a comparison with the intrinsic noise fluctuations of our setup is required. These noise fluctuations were acquired with measurements of the attenuated laser beam on the setup CCD camera. We adapted the incoming laser power in order to obtain count rates matching the range of PL and/or Raman count rates typically observed in our experiments. For a given mean signal intensity I the standard deviation of the intrinsic measurement noise $\sigma(I)$ has contributions from classical laser intensity fluctuations $\sigma_\mathrm{L} = \sigma_\mathrm{L}^\mathrm{r} I$, scaling linearly with I, from photon shot noise $\sigma_\mathrm{S} = \sigma_\mathrm{sn}^\mathrm{r} \sqrt{I}$, and from detector noise σ_D (mainly readout noise of the CCD; for the short acquisition times used here dark current is negligible), according to $\sigma(I) = \sqrt{(\sigma_\mathrm{L}^\mathrm{r} I)^2 + (\sigma_\mathrm{sn}^\mathrm{r} \sqrt{I})^2 + \sigma_\mathrm{D}^2}$
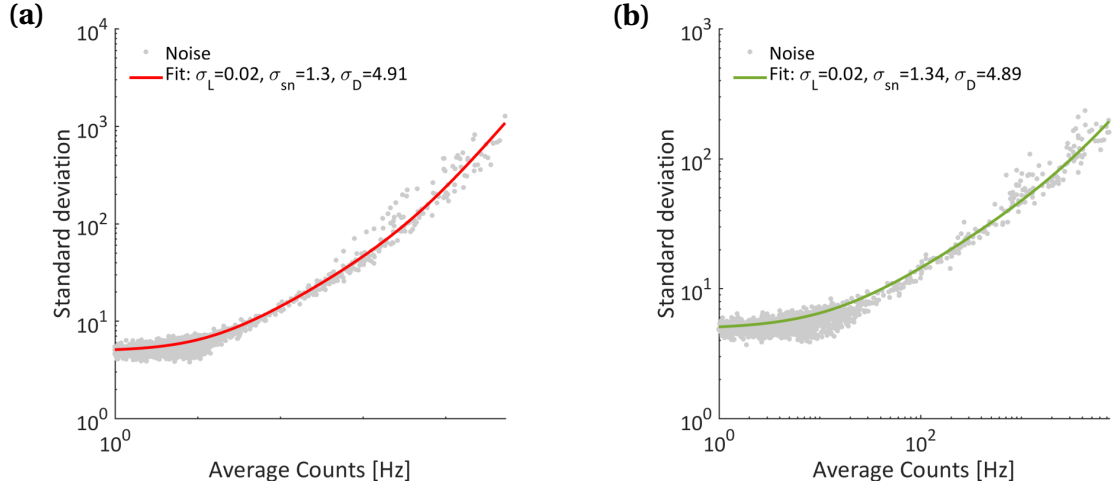
Figure D.2 – Measurement noise of the setup under 750 nm (**a**) and 532 nm (**b**) illumination. The fit parameters are defined in the section and used to evaluate the blinking traces reported in the text. Each point corresponds to the average of 100 acquisitions on a single pixel.

[184]. This formula is used to fit the noise characterization data, with the parameters shown in Fig. D.2. The shaded blue areas in the probability density function (PDF) in the text and follow a Gaussian distribution given by $f_{\text{PDF}}(I) = \exp\left[-(I - I_{\text{PDF}})^2/2[\sigma(I_{\text{PDF}})]^2\right]$, where I_{PDF} is the maximum of the PDF of the intensity trace to be calculated. In the time traces the blue areas are defined as $I_{\text{PDF}} - 3\sigma(I_{\text{PDF}}) \leq I \leq I_{\text{PDF}} + 3\sigma(I_{\text{PDF}})$, where I_{PDF} is used to present the average value of the baseline PL.
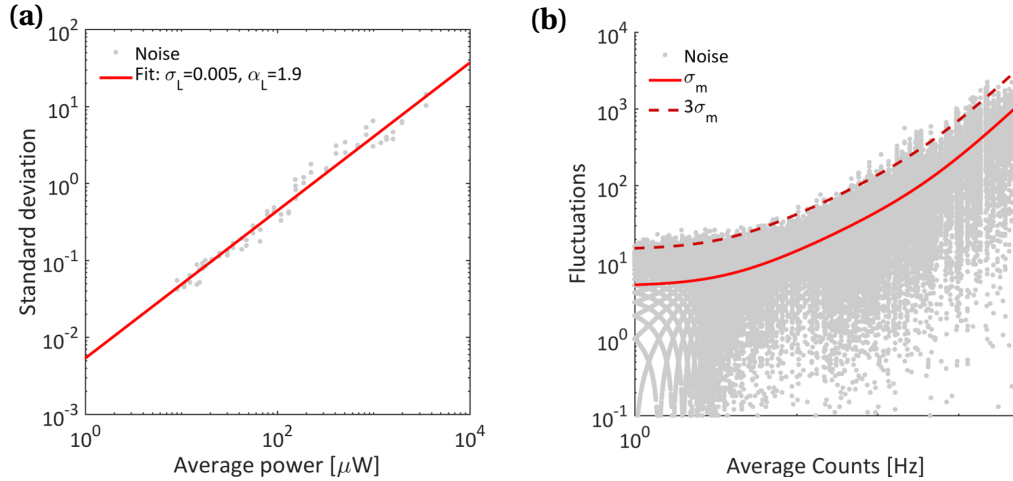
Figure D.3 – (**a**) Measurement noise of the 750 nm source before the microscope and as characterized by a powermeter. The fit parameters are modeled by the expression : $\sigma_{\text{PM}}^2 \simeq \left(\sigma_{\text{L}}^{\text{r}}\right)^2 I^{\alpha_L}$. (**b**) Measurement noise at the ccd camera of the setup. Each point corresponds to a single acquisition on a single pixel. The $3\sigma_m$ dashed line represents the simple threshold used in the text to evaluate our blinking observations.

Fig. D.3(a) shows the complementary characterization of the laser intensity fluctuations, also called relative intensity noise (RIN), recorded simultaneously on a powermeter. Fig. D.3(b) evidences for single acquisitions the fluctuations of noise and the level of fluctuations used as an indicator in our blinking experiments.

E Anomalous Raman scattering events
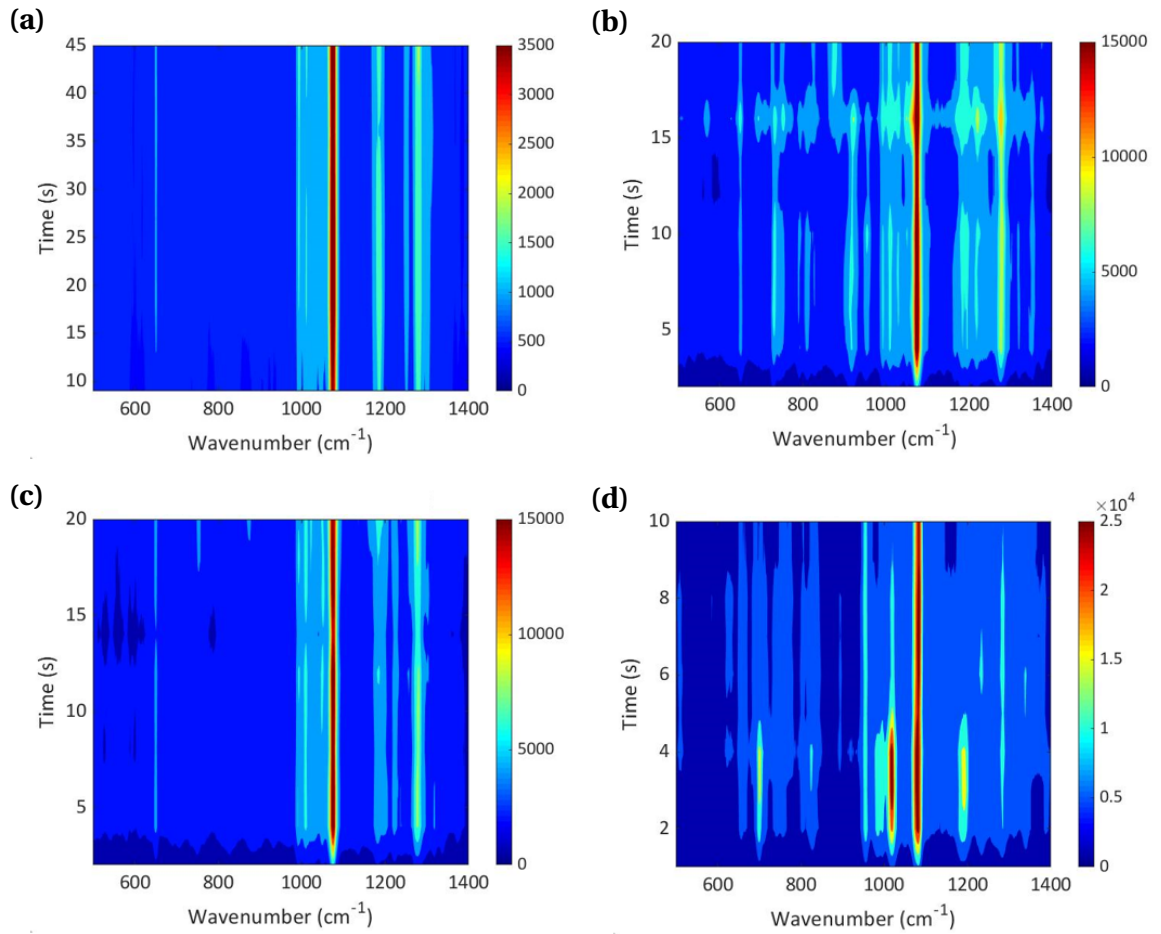
Figure E.1 – Time series of the laboratory noise substracted level of counts per second generated on the Stokes sideband by a single (BPT-TS) nanojunction excited with a radially polarized beam at 750 nm for successive incoming powers of 40 μW **(a)**, 160 μW **(b)** 160 μW **(c)** and 200 μW **(d)** at the sample.

Appendix E. Anomalous Raman scattering events

Many of the investigated structures evidenced anomalous Raman scattering events at room temperature alike events previously observed in the literature [20, 64, 113]. These events, described as 'picocavity events' in part of this literature, are characterized by the emergence of other Raman lines and possible modifications of preexisting lines in the spectra without important modifications of the background. As evidenced in Fig. E.1 such events start to appear for a certain threshold power (sensitive to the specific nanojunction fabricated) and last for period as long as tens of seconds.
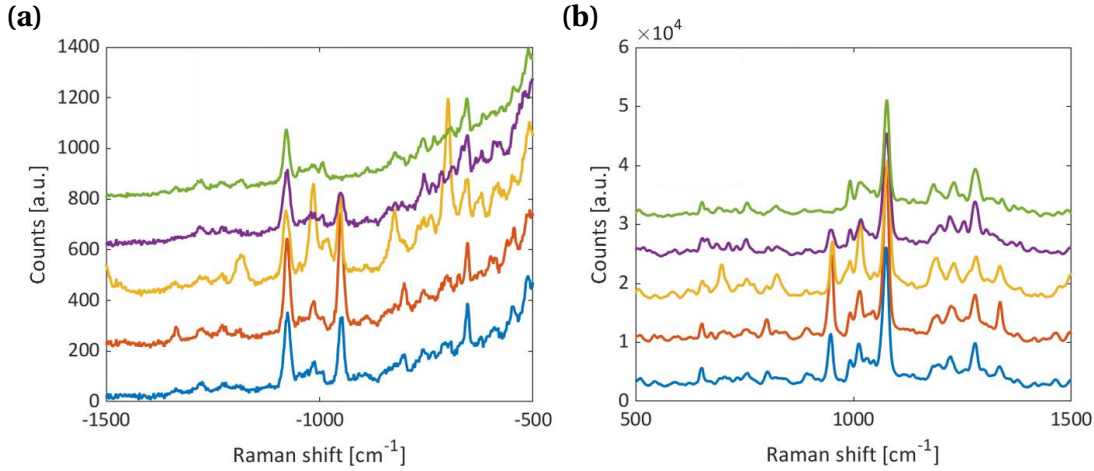
Figure E.2 – Laboratory noise substracted level of counts per second generated on the anti-Stokes **(a)** and Stokes **(b)** sidebands by a single (BPT-TS) nanojunction excited with a radially polarized beam at 750 nm and 200 μW at the sample. The different colors represent single 1 s acquisition spectra simultaneously recorded on both sidebands. The successive spectra are separated by a vertical offset to improve readability.

The nature of such events is debated but the appearence in this regime of largely non thermal ratio between the two vibrational sidebands (cf. yellow spectra in Fig.E.2) seems to indicate an additional exchange mechanism between an out-of-equilibrium plasmonic population and some vibrational modes [185–187].

Bibliography

[1] Edgar Bright Wilson, J. C. Decius, and Paul C. Cross. *Molecular Vibrations: The Theory of Infrared and Raman Vibrational Spectra.* Courier Corporation, March 1980.

[2] Gerhard Herzberg. *Molecular Spectra and Molecular Structure II. Infrared and Raman Spectra of Polyatomic Molecules.* D. Van Nostrand Company, Inc., 1960.

[3] Eric Le Ru and Pablo Etchegoin. *Principles of Surface-Enhanced Raman Spectroscopy: and Related Plasmonic Effects.* Elsevier, November 2008.

[4] William De Wiveleslie Abney and Lieut.-colonel Festing. XX, On the influence of the atomic grouping in the molecules of organic bodies on their absorption in the infrared region of the spectrum. *Philosophical Transactions of the Royal Society of London,* 172:887–918, January 1881. Publisher: Royal Society.

[5] Max Planck. Zur electromagnetischen Theorie der selectiven Absorption in Isotropen Nichtleitern. page 21.

[6] C. V. Raman. A Change of Wave-length in Light Scattering. *Nature,* 121(3051):619–619, April 1928. Number: 3051 Publisher: Nature Publishing Group.

[7] H. A. Kramers and W. Heisenberg. Über die Streuung von Strahlung durch Atome. *Zeitschrift für Physik,* 31(1):681–708, February 1925.

[8] H. A. Kramers. The Law of Dispersion and Bohr's Theory of Spectra. *Nature,* 113(2845):673–674, May 1924. Number: 2845 Publisher: Nature Publishing Group.

[9] W. Heisenberg. Über quantentheoretische Umdeutung kinematischer und mechanischer Beziehungen. *Zeitschrift für Physik,* 33(1):879–893, December 1925.

[10] Philip M. Morse. Diatomic Molecules According to the Wave Mechanics. II. Vibrational Levels. *Physical Review,* 34(1):57–64, July 1929.

[11] Byron T. Darling and David M. Dennison. The Water Vapor Molecule. *Physical Review,* 57(2):128–139, January 1940.

[12] R. Zhang, Y. Zhang, Z. C. Dong, S. Jiang, C. Zhang, L. G. Chen, L. Zhang, Y. Liao, J. Aizpurua, Y. Luo, J. L. Yang, and J. G. Hou. Chemical mapping of a single molecule by plasmon-enhanced raman scattering. *Nature,* 498(7452):82–6, 2013.

Bibliography

[13] Jin-Hui Zhong, Xi Jin, Lingyan Meng, Xiang Wang, Hai-Sheng Su, Zhi-Lin Yang, Christopher T. Williams, and Bin Ren. Probing the electronic and catalytic properties of a bimetallic surface with 3 nm resolution. *Nature Nanotechnology*, 12(2):132–136, February 2017.

[14] Joonhee Lee, Kevin T. Crampton, Nicholas Tallarida, and V. Ara Apkarian. Visualizing vibrational normal modes of a single molecule with atomically confined light. *Nature*, 568(7750):78, April 2019.

[15] Conrard Giresse Tetsassi Feugmo and Vincent Liégeois. Analyzing the Vibrational Signatures of Thiophenol Adsorbed on Small Gold Clusters by DFT Calculations. *ChemPhysChem*, 14(8):1633–1645, June 2013.

[16] John David Jackson. *Classical Electrodynamics, third edition.* John Wiley & Sons, Inc., New York, 3rd edition edition, 1998.

[17] E.B. Wilson, J.C. Decius, and P.C. Cross. *Molecular Vibrations: The Theory of Infrared and Raman Vibrational Spectra.* Dover Publications, 1955.

[18] C. Vericat, M. E. Vela, G. Corthey, E. Pensa, E. Cortés, M. H. Fonticelli, F. Ibañez, G. E. Benitez, P. Carro, and R. C. Salvarezza. Self-assembled monolayers of thiolates on metals: a review article on sulfur-metal chemistry and surface structures. *RSC Adv.*, 4(53):27730–27754, 2014.

[19] R. Zhang, Y. Zhang, Z. C. Dong, S. Jiang, C. Zhang, L. G. Chen, L. Zhang, Y. Liao, J. Aizpurua, Y. Luo, J. L. Yang, and J. G. Hou. Chemical mapping of a single molecule by plasmon-enhanced Raman scattering. *Nature*, 498(7452):82–86, June 2013.

[20] Felix Benz, Mikolaj K. Schmidt, Alexander Dreismann, Rohit Chikkaraddy, Yao Zhang, Angela Demetriadou, Cloudy Carnegie, Hamid Ohadi, Bart de Nijs, Ruben Esteban, Javier Aizpurua, and Jeremy J. Baumberg. Single-molecule optomechanics in "picocavities". *Science*, 354(6313):726–729, 2016.

[21] Kai-Qiang Lin, Jun Yi, Jin-Hui Zhong, Shu Hu, Bi-Ju Liu, Jun-Yang Liu, Cheng Zong, Zhi-Chao Lei, Xiang Wang, Javier Aizpurua, Rubén Esteban, and Bin Ren. Plasmonic photoluminescence for recovering native chemical information from surface-enhanced Raman scattering. *Nat Commun*, 8(1):14891, April 2017.

[22] L. D. Landau, L. P. Pitaevskii, and E. M. Lifshitz. *Electrodynamics of Continuous Media, Second Edition: Volume 8 (Course of Theoretical Physics).* Butterworth-Heinemann, January 1984.

[23] R. Loudon. The propagation of electromagnetic energy through an absorbing dielectric. *Journal of Physics A: General Physics*, 3(3):233, 1970.

[24] Feng Wang and Y. Ron Shen. General properties of local plasmons in metal nanostructures. *Physical Review Letters*, 97(20), 2006.

[25] P. B. Johnson and R. W. Christy. Optical Constants of the Noble Metals. *Phys. Rev. B*, 6(12):4370–4379, December 1972.

[26] Jacob B. Khurgin. How to deal with the loss in plasmonics and metamaterials. *Nature Nanotechnology*, 10(1):2–6, January 2015.

[27] Philippe Lalanne, Wei Yan, Kevin Vynck, Christophe Sauvan, and Jean-Paul Hugonin. Light Interaction with Photonic and Plasmonic Resonances. *Laser & Photonics Reviews*, 12(5):1700113, 2018.

[28] Rohit Chikkaraddy, Bart de Nijs, Felix Benz, Steven J. Barrow, Oren A. Scherman, Edina Rosta, Angela Demetriadou, Peter Fox, Ortwin Hess, and Jeremy J. Baumberg. Single-molecule strong coupling at room temperature in plasmonic nanocavities. *Nature*, 535(7610):127–130, July 2016.

[29] Marlan O. Scully, Scully, and M. Suhail Zubairy. *Quantum Optics*. Cambridge University Press, September 1997.

[30] C. Sauvan, J. P. Hugonin, I. S. Maksymov, and P. Lalanne. Theory of the Spontaneous Optical Emission of Nanosize Photonic and Plasmon Resonators. *Physical Review Letters*, 110(23), June 2013.

[31] Mohsen Kamandar Dezfouli, Reuven Gordon, and Stephen Hughes. Modal theory of modified spontaneous emission of a quantum emitter in a hybrid plasmonic photonic-crystal cavity system. *Physical Review A*, 95(1):013846, January 2017.

[32] Burak Gurlek, Vahid Sandoghdar, and Diego Martin-Cano. Manipulation of quenching in nanoantenna–emitter systems enabled by external detuned cavities: A path to enhance strong-coupling. *ACS Photonics*, 5(2):456–461, 2018.

[33] Mohsen Kamandar Dezfouli, Reuven Gordon, and Stephen Hughes. Molecular Optomechanics in the Anharmonic Cavity-QED Regime Using Hybrid Metal–Dielectric Cavity Modes. *ACS Photonics*, 6(6):1400–1408, June 2019.

[34] Jeremy J. Baumberg, Javier Aizpurua, Maiken H. Mikkelsen, and David R. Smith. Extreme nanophotonics from ultrathin metallic gaps. *Nat. Mater.*, 18(7):668–678, July 2019.

[35] Wen Chen, Shunping Zhang, Meng Kang, Weikang Liu, Zhenwei Ou, Yang Li, Yexin Zhang, Zhiqiang Guan, and Hongxing Xu. Probing the limits of plasmonic enhancement using a two-dimensional atomic crystal probe. *Light: Science & Applications*, 7(1):56, August 2018.

[36] Cheng Zhang, Jean-Paul Hugonin, Jean-Jacques Greffet, and Christophe Sauvan. Surface Plasmon Polaritons Emission with Nanopatch Antennas: Enhancement by Means of Mode Hybridization. *ACS Photonics*, October 2019.

[37] Rohit Chikkaraddy, Xuezhi Zheng, Felix Benz, Laura J. Brooks, Bart de Nijs, Cloudy Carnegie, Marie-Elena Kleemann, Jan Mertens, Richard W. Bowman, Guy A. E. Vandenbosch, Victor V. Moshchalkov, and Jeremy J. Baumberg. How Ultranarrow Gap Symmetries Control Plasmonic Nanocavity Modes: From Cubes to Spheres in the Nanoparticle-on-Mirror. *ACS Photonics*, 4(3):469–475, March 2017.

[38] Lisa V. Brown, Xiao Yang, Ke Zhao, Bob Y. Zheng, Peter Nordlander, and Naomi J. Halas. Fan-Shaped Gold Nanoantennas above Reflective Substrates for Surface-Enhanced Infrared Absorption (SEIRA). *Nano Letters*, 15(2):1272–1280, February 2015.

[39] D. R. Lide, editor. *CRC Handbook of Chemistry and Physics*. CRC Press, Boca Raton, FL, 87 edition, 2006.

[40] Arvind Sundaramurthy, K. B. Crozier, G. S. Kino, D. P. Fromm, P. J. Schuck, and W. E. Moerner. Field enhancement and gap-dependent resonance in a system of two opposing tip-to-tip Au nanotriangles. *Phys. Rev. B: Condens. Matter Mater. Phys.*, 72(16):165409, October 2005.

[41] Mikolaj K. Schmidt, Ruben Esteban, Felix Benz, Jeremy J. Baumberg, and Javier Aizpurua. Linking classical and molecular optomechanics descriptions of SERS. *Faraday Discussions*, 205(0):31–65, November 2017.

[42] M. Fleischmann, P.J. Hendra, and A.J. McQuillan. Raman spectra of pyridine adsorbed at a silver electrode. *Chemical Physics Letters*, 26(2):163 – 166, 1974.

[43] David L. Jeanmaire and Richard P. Van Duyne. Surface raman spectroelectrochemistry: Part i. heterocyclic, aromatic, and aliphatic amines adsorbed on the anodized silver electrode. *Journal of Electroanalytical Chemistry and Interfacial Electrochemistry*, 84(1):1 – 20, 1977.

[44] Katrin Kneipp, Yang Wang, Harald Kneipp, Lev T. Perelman, Irving Itzkan, Ramachandra R. Dasari, and Michael S. Feld. Single molecule detection using surface-enhanced raman scattering (sers). *Phys. Rev. Lett.*, 78:1667–1670, Mar 1997.

[45] S. Nie. Probing single molecules and single nanoparticles by surface-enhanced raman scattering. *Science*, 275(5303):1102–1106, 1997.

[46] .V.M. Shalaev and A.K. Sarychev. Nonlinear optics of random metal-dielectric films. *Phys. Rev. B*, 57(13265-88), 1998.

[47] B. Pettinger, P. Schambach, C. J. Villagomez, and N. Scott. Tip-enhanced raman spectroscopy: near-fields acting on a few molecules. *Annual Reviews of Physical Chemistry*, 63:379–99, 2012.

[48] Bhavya Sharma, M. Fernanda Cardinal, Samuel L. Kleinman, Nathan G. Greeneltch, Renee R. Frontiera, Martin G. Blaber, George C. Schatz, and Richard P. Van Duyne. High-performance sers substrates: Advances and challenges. *MRS Bulletin*, 38(08):615–624, 2013.

[49] X. M. Qian and S. M. Nie. Single-molecule and single-nanoparticle sers: from fundamental mechanisms to biomedical applications. *Chem Soc Rev*, 37(5):912–20, 2008.

[50] Yu Luo, Alexandre Aubry, and J. B. Pendry. Electromagnetic contribution to surface-enhanced raman scattering from rough metal surfaces: A transformation optics approach. *Phys. Rev. B*, 83:155422, Apr 2011.

[51] Katrin Kneipp, Yang Wang, Harald Kneipp, Irving Itzkan, Ramachandra R. Dasari, and Michael S. Feld. Population pumping of excited vibrational states by spontaneous surface-enhanced raman scattering. *Phys. Rev. Lett.*, 76:2444–2447, Apr 1996.

[52] R. C. Maher, L. F. Cohen, P. Etchegoin, H. J. N. Hartigan, R. J. C. Brown, and M. J. T. Milton. Stokes/anti-stokes anomalies under surface enhanced raman scattering conditions. *The Journal of Chemical Physics*, 120(24):11746, 2004.

[53] R. C. Maher, C. M. Galloway, E. C. Le Ru, L. F. Cohen, and P. G. Etchegoin. Vibrational pumping in surface enhanced raman scattering (sers). *Chem. Soc. Rev.*, 37:965–979, 2008.

[54] Wenqi Zhu and Kenneth B. Crozier. Quantum mechanical limit to plasmonic enhancement as observed by surface-enhanced raman scattering. *Nat Commun*, 5, 10 2014.

[55] Song Jiang, Yao Zhang, Rui Zhang, Chunrui Hu, Menghan Liao, Yi Luo, Jinlong Yang, Zhenchao Dong, and JG Hou. Distinguishing adjacent molecules on a surface using plasmon-enhanced raman scattering. *Nat Nano*, advance online publication, 2015.

[56] Joanna M Atkin and Markus B Raschke. Techniques: Optical spectroscopy goes intramolecular. *Nature*, 498(7452):44–45, 2013.

[57] T. J. Kippenberg and K. J. Vahala. Cavity Optomechanics: Back-Action at the Mesoscale. *Science*, 321:1172–1176, 2008.

[58] V.B. Braginsky and A.B. Manukin. Ponderomotive effects of electromagnetic radiation. *Soviet Physics JETP*, 25:653, 1967.

[59] T.J. Kippenberg, H. Rokhsari, T. Carmon, A. Scherer, and K.J. Vahala. Analysis of radiation-pressure induced mechanical oscillation of an optical microcavity. *Phys. Rev. Lett.*, 95:033901, 07 2005.

[60] Markus Aspelmeyer, Tobias J Kippenberg, and Florian Marquardt. Cavity optomechanics. *Reviews of Modern Physics*, 86(4):1391, 2014.

[61] M. L. Gorodetsky, A. Schliesser, G. Anetsberger, S. Deleglise, and T. J. Kippenberg. Determination of the vacuum optomechanical coupling rate using frequency noise calibration. *Opt. Express*, 18(22):23236–23246, Oct 2010.

[62] John D. Jackson. *Classical Electrodynamics Third Edition*. Wiley, August 1998.

[63] A. F. Koenderink. On the use of purcell factors for plasmon antennas. *Opt. Lett.*, 35(24):4208–4210, Dec 2010.

[64] Mayukh Banik, Patrick Z. El-Khoury, Amit Nag, Alejandro Rodriguez-Perez, Nekane Guarrottxena, Guillermo C. Bazan, and Vartkess A. Apkarian. Surface-Enhanced Raman Trajectories on a Nano-Dumbbell: Transition from Field to Charge Transfer Plasmons as the Spheres Fuse. *ACS Nano*, 6(11):10343–10354, November 2012. Publisher: American Chemical Society.

[65] Jianji Yang, Harald Giessen, and Philippe Lalanne. Simple Analytical Expression for the Peak-Frequency Shifts of Plasmonic Resonances for Sensing. *Nano Letters*, 15(5):3439–3444, May 2015. Publisher: American Chemical Society.

[66] Talitha Weiss and Andreas Nunnenkamp. Quantum limit of laser cooling in dispersively and dissipatively coupled optomechanical systems. *Physical Review A*, 88(2):023850, August 2013. Publisher: American Physical Society.

[67] Kevin J. Savage, Matthew M. Hawkeye, Ruben Esteban, Javier Borisov, Andrei G.and Aizpurua, and Jeremy J. Baumberg. Revealing the quantum regime in tunnelling plasmonics. *Nature*, 491, 2012.

[68] Hiroyuki Watanabe, Norihiko Hayazawa, Yasushi Inouye, and Satoshi Kawata. Dft vibrational calculations of rhodamine 6g adsorbed on silver analysis of tip-enhanced raman spectroscopy. *The Journal of Physical Chemistry B*, 109(11):5012–5020, 2005.

[69] C. Humbert, O. Pluchery, E. Lacaze, A. Tadjeddine, and B. Busson. A multiscale description of molecular adsorption on gold nanoparticles by nonlinear optical spectroscopy. *Phys. Chem. Chem. Phys.*, 14:280–289, 2012.

[70] Rohit Narula, Robert Panknin, and Stephanie Reich. Absolute raman matrix elements of graphene and graphite. *Phys. Rev. B*, 82:045418, Jul 2010.

[71] Raphaël Van Laer, Bart Kuyken, Roel Baets, and Dries Van Thourhout. Unifying brillouin scattering and cavity optomechanics. *arXiv preprint arXiv:1503.03044*, 2015.

[72] Atef Shalabney, Jino George, J Hutchison, Guido Pupillo, Cyriaque Genet, and Thomas W Ebbesen. Coherent coupling of molecular resonators with a microcavity mode. *Nature communications*, 6, 2015.

[73] J. P. Long and B. S. Simpkins. Coherent coupling between a molecular vibration and fabry–perot optical cavity to give hybridized states in the strong coupling limit. *ACS Photonics*, 2(1):130–136, 2015.

[74] Albert Schliesser and Tobias J. Kippenberg. Chapter 5 - cavity optomechanics with whispering-gallery mode optical micro-resonators. In Ennio Arimondo Paul Berman and Chun Lin, editors, *Advances In Atomic, Molecular, and Optical Physics*, volume 58 of *Advances In Atomic, Molecular, and Optical Physics*, pages 207 – 323. Academic Press, 2010.

[75] R.W. Boyd. *Nonlinear Optics*. Elsevier Science, 2003.

[76] Thierry Botter, Daniel W. C. Brooks, Nathan Brahms, Sydney Schreppler, and Dan M. Stamper-Kurn. Linear amplifier model for optomechanical systems. *Phys. Rev. A*, 85:013812, Jan 2012.

[77] I. Wilson-Rae, N. Nooshi, W. Zwerger, and T. J. Kippenberg. Theory of ground state cooling of a mechanical oscillator using dynamical backaction. *Phys. Rev. Lett.*, 99:093901, Aug 2007.

[78] Christophe Galland, Nicolas Sangouard, Nicolas Piro, Nicolas Gisin, and Tobias J. Kippenberg. Heralded single-phonon preparation, storage, and readout in cavity optomechanics. *Phys. Rev. Lett.*, 112:143602, Apr 2014.

[79] Jasper Chan, Amir H. Safavi-Naeini, Jeff T. Hill, Seán Meenehan, and Oskar Painter. Optimized optomechanical crystal cavity with acoustic radiation shield. *Applied Physics Letters*, 101(8):–, 2012.

[80] Tobias J. Kippenberg and Kerry J. Vahala. Cavity opto-mechanics. *Opt. Express*, 15(25):17172–17205, Dec 2007.

[81] C. K. Law. Interaction between a moving mirror and radiation pressure: A hamiltonian formulation. *Phys. Rev. A*, 51:2537–2541, Mar 1995.

[82] C. W. Gardiner and M. J. Collett. Input and output in damped quantum systems: Quantum stochastic differential equations and the master equation. *Phys. Rev. A*, 31:3761–3774, Jun 1985.

[83] Florian Marquardt, J. G. E. Harris, and S. M. Girvin. Dynamical multistability induced by radiation pressure in high-finesse micromechanical optical cavities. *Phys. Rev. Lett.*, 96:103901, Mar 2006.

[84] A. Schliesser, P. Del'Haye, N. Nooshi, K. J. Vahala, and T. J. Kippenberg. Radiation pressure cooling of a micromechanical oscillator using dynamical backaction. *Phys. Rev. Lett.*, 97:243905, Dec 2006.

[85] A. Schliesser, R. Riviere, G. Anetsberger, O. Arcizet, and T. J. Kippenberg. Resolved-sideband cooling of a micromechanical oscillator. *Nature Physics*, 4(5):415–419, 2008.

[86] Behnood G. Ghamsari, Anthony Olivieri, Fabio Variola, and Pierre Berini. Frequency pulling and line-shape broadening in graphene raman spectra by resonant stokes surface plasmon polaritons. *Phys. Rev. B*, 91:201408, May 2015.

[87] G. S. Agarwal and Sudhanshu S. Jha. Multimode phonon cooling via three-wave parametric interactions with optical fields. *Phys. Rev. A*, 88:013815, Jul 2013.

[88] T. Kipf and G. S. Agarwal. Superradiance and collective gain in multimode optomechanics. *Phys. Rev. A*, 90:053808, Nov 2014.

[89] Jon P. Camden, Jon A. Dieringer, Yingmin Wang, David J. Masiello, Lawrence D. Marks, George C. Schatz, and Richard P. Van Duyne. Probing the structure of single-molecule surface-enhanced raman scattering hot spots. *Journal of the American Chemical Society*, 130(38):12616–12617, 2008.

[90] I Wilson-Rae, N Nooshi, J Dobrindt, T J Kippenberg, and W Zwerger. Cavity-assisted backaction cooling of mechanical resonators. *New Journal of Physics*, 10(9):095007, 2008.

[91] I. Wilson-Rae, N. Nooshi, J. Dobrindt, T. J. Kippenberg, and W. Zwerger. Cavity-assisted backaction cooling of mechanical resonators. *New Journal of Physics*, 10(9):095007, September 2008.

[92] Hugo M. Doeleman, Ewold Verhagen, and A. Femius Koenderink. Antenna–cavity hybrids: Matching polar opposites for purcell enhancements at any linewidth. *ACS Photonics*, 3(10):1943–1951, 2016.

[93] L. Mandel and E. Wolf. *Optical Coherence and Quantum Optics*. Cambridge University Press, 1995.

[94] V.M. Kenkre, A. Tokmakoff, and M.D. Fayer. Theory of vibrational relaxation of polyatomic molecules in liquids. *Journal of Physical Chemistry*, 101:10618–10629, 1994.

[95] Wen Chen, Shunping Zhang, Qian Deng, and Hongxing Xu. Probing of sub-picometer vertical differential resolutions using cavity plasmons. *Nat Commun*, 9(1):801, December 2018.

[96] Caixia Kan, Xiaoguang Zhu, and Guanghou Wang. Single-Crystalline Gold Microplates: Synthesis, Characterization, and Thermal Stability. *J. Phys. Chem. B*, 110(10):4651–4656, March 2006.

[97] James T. Hugall and Jeremy J. Baumberg. Demonstrating Photoluminescence from Au is Electronic Inelastic Light Scattering of a Plasmonic Metal: The Origin of SERS Backgrounds. *Nano Lett.*, 15(4):2600–2604, April 2015.

[98] Sebastian K. H. Andersen, Anders Pors, and Sergey I. Bozhevolnyi. Gold Photoluminescence Wavelength and Polarization Engineering. *ACS Photonics*, 2(3):432–438, March 2015.

[99] Dmitry Sivun, Cynthia Vidal, Battulga Munkhbat, Nikita Arnold, Thomas A. Klar, and Calin Hrelescu. Anticorrelation of Photoluminescence from Gold Nanoparticle Dimers with Hot-Spot Intensity. *Nano Lett.*, 16(11):7203–7209, November 2016.

[100] Jun G. Liu, Hui Zhang, Stephan Link, and Peter Nordlander. Relaxation of Plasmon-Induced Hot Carriers. *ACS Photonics*, 5(7):2584–2595, July 2018.

[101] Michael R. Beversluis, Alexandre Bouhelier, and Lukas Novotny. Continuum generation from single gold nanostructures through near-field mediated intraband transitions. *Phys. Rev. B*, 68(11):115433, September 2003.

[102] Chatdanai Lumdee, Binfeng Yun, and Pieter G. Kik. Gap-Plasmon Enhanced Gold Nanoparticle Photoluminescence. *ACS Photonics*, 1(11):1224–1230, November 2014.

[103] Jan Mertens, Marie-Elena Kleemann, Rohit Chikkaraddy, Prineha Narang, and Jeremy J. Baumberg. How Light Is Emitted by Plasmonic Metals. *Nano Lett.*, 17(4):2568–2574, April 2017.

[104] Aquiles Carattino, Martín Caldarola, and Michel Orrit. Gold Nanoparticles as Absolute Nanothermometers. *Nano Letters*, 18(2):874–880, February 2018.

[105] Yi-Yu Cai, Jun G. Liu, Lawrence J. Tauzin, Da Huang, Eric Sung, Hui Zhang, Anneli Joplin, Wei-Shun Chang, Peter Nordlander, and Stephan Link. Photoluminescence of Gold Nanorods: Purcell Effect Enhanced Emission from Hot Carriers. *ACS Nano*, 12(2):976–985, February 2018.

[106] R. Dorn, S. Quabis, and G. Leuchs. Sharper Focus for a Radially Polarized Light Beam. *Physical Review Letters*, 91(23):233901, December 2003.

[107] Bing Hao and James Leger. Experimental measurement of longitudinal component in the vicinity of focused radially polarized beam. *Optics Express*, 15(6):3550–3556, March 2007.

[108] S. Roy, K. Ushakova, Q. van den Berg, S.F. Pereira, and H.P. Urbach. Radially Polarized Light for Detection and Nanolocalization of Dielectric Particles on a Planar Substrate. *Physical Review Letters*, 114(10):103903, March 2015.

[109] Simon Grosche, Simon Grosche, Simon Grosche, Simon Grosche, Richard Hünermann, Richard Hünermann, Richard Hünermann, George Sarau, George Sarau, Silke Christiansen, Silke Christiansen, Silke Christiansen, Robert W. Boyd, Robert W. Boyd, Gerd Leuchs, Gerd Leuchs, Gerd Leuchs, Peter Banzer, Peter Banzer, and Peter Banzer. Towards polarization-based excitation tailoring for extended Raman spectroscopy. *Optics Express*, 28(7):10239–10252, March 2020.

[110] Jing Long, Hui Yi, Hongquan Li, Zeyu Lei, and Tian Yang. Reproducible Ultrahigh SERS Enhancement in Single Deterministic Hotspots Using Nanosphere-Plane Antennas Under Radially Polarized Excitation. *Scientific Reports*, 6:33218, September 2016.

[111] Daniel O. Sigle, Jan Mertens, Lars O. Herrmann, Richard W. Bowman, Sandrine Ithurria, Benoit Dubertret, Yumeng Shi, Hui Ying Yang, Christos Tserkezis, Javier Aizpurua, and Jeremy J. Baumberg. Monitoring Morphological Changes in 2D Monolayer Semiconductors Using Atom-Thick Plasmonic Nanocavities. *ACS Nano*, 9(1):825–830, January 2015.

Bibliography

[112] J. Mertens, A. Demetriadou, R. W. Bowman, F. Benz, M.-E. Kleemann, C. Tserkezis, Y. Shi, H. Y. Yang, O. Hess, J. Aizpurua, and J. J. Baumberg. Tracking Optical Welding through Groove Modes in Plasmonic Nanocavities. *Nano Letters*, 16(9):5605–5611, September 2016.

[113] Cloudy Carnegie, Jack Griffiths, Bart de Nijs, Charlie Readman, Rohit Chikkaraddy, William M. Deacon, Yao Zhang, István Szabó, Edina Rosta, Javier Aizpurua, and Jeremy J. Baumberg. Room-Temperature Optical Picocavities below 1 nm3 Accessing Single-Atom Geometries. *The Journal of Physical Chemistry Letters*, 9(24):7146–7151, December 2018.

[114] Anna Lombardi, Mikołaj K. Schmidt, Lee Weller, William M. Deacon, Felix Benz, Bart de Nijs, Javier Aizpurua, and Jeremy J. Baumberg. Pulsed Molecular Optomechanics in Plasmonic Nanocavities: From Nonlinear Vibrational Instabilities to Bond-Breaking. *Physical Review X*, 8(1):011016, February 2018.

[115] M. Sivis, M. Duwe, B. Abel, and C. Ropers. Extreme-ultraviolet light generation in plasmonic nanostructures. *Nature Physics*, 9(5):304–309, May 2013.

[116] Jiha Sung, Kathryn M. Kosuda, Jing Zhao, Jeffrey W. Elam, Kenneth G. Spears, and Richard P. Van Duyne. Stability of Silver Nanoparticles Fabricated by Nanosphere Lithography and Atomic Layer Deposition to Femtosecond Laser Excitation. *The Journal of Physical Chemistry C*, 112(15):5707–5714, April 2008.

[117] Wen Chen, Shunping Zhang, Meng Kang, Weikang Liu, Zhenwei Ou, Yang Li, Yexin Zhang, Zhiqiang Guan, and Hongxing Xu. Probing the limits of plasmonic enhancement using a two-dimensional atomic crystal probe. *Light: Science & Applications*, 7(1):56, August 2018.

[118] Daehan Yoo, Kargal L. Gurunatha, Han-Kyu Choi, Daniel A. Mohr, Christopher T. Ertsgaard, Reuven Gordon, and Sang-Hyun Oh. Low-Power Optical Trapping of Nanoparticles and Proteins with Resonant Coaxial Nanoaperture Using 10 nm Gap. *Nano Letters*, 18(6):3637–3642, June 2018.

[119] Ying Fang, Wei-Shun Chang, Britain Willingham, Pattanawit Swanglap, Sergio Dominguez-Medina, and Stephan Link. Plasmon Emission Quantum Yield of Single Gold Nanorods as a Function of Aspect Ratio. *ACS Nano*, 6(8):7177–7184, August 2012.

[120] Da Huang, Chad P. Byers, Lin-Yung Wang, Anneli Hoggard, Ben Hoener, Sergio Dominguez-Medina, Sishan Chen, Wei-Shun Chang, Christy F. Landes, and Stephan Link. Photoluminescence of a Plasmonic Molecule. *ACS Nano*, 9(7):7072–7079, July 2015.

[121] Markus Parzefall, Áron Szabó, Takashi Taniguchi, Kenji Watanabe, Mathieu Luisier, and Lukas Novotny. Light from van der Waals quantum tunneling devices. *Nat Commun*, 10(1):1–9, January 2019.

[122] Meindert A. van Dijk, Markus Lippitz, and Michel Orrit. Far-Field Optical Microscopy of Single Metal Nanoparticles. *Acc. Chem. Res.*, 38(7):594–601, July 2005.

[123] Jie Zheng, Chen Zhou, Mengxiao Yu, and Jinbin Liu. Different sized luminescent gold nanoparticles. *Nanoscale*, 4(14):4073, 2012.

[124] Weidong Zhang, Te Wen, Yuqing Cheng, Jingyi Zhao, Qihuang Gong, and Guowei Lü. Intrinsic luminescence from metal nanostructures and its applications. *Chinese Phys. B*, 27(9):097302, September 2018.

[125] Joanna Olesiak-Banska, Magdalena Waszkielewicz, Patryk Obstarczyk, and Marek Samoc. Two-photon absorption and photoluminescence of colloidal gold nanoparticles and nanoclusters. *Chem. Soc. Rev.*, 48(15):4087–4117, July 2019.

[126] G. T. Boyd, Z. H. Yu, and Y. R. Shen. Photoinduced luminescence from the noble metals and its enhancement on roughened surfaces. *Phys. Rev. B*, 33(12):7923–7936, June 1986.

[127] Ravishankar Sundararaman, Prineha Narang, Adam S. Jermyn, William A. Goddard Iii, and Harry A. Atwater. Theoretical predictions for hot-carrier generation from surface plasmon decay. *Nat Commun*, 5(1):1–8, December 2014.

[128] Ana M. Brown, Ravishankar Sundararaman, Prineha Narang, William A. Goddard, and Harry A. Atwater. Nonradiative Plasmon Decay and Hot Carrier Dynamics: Effects of Phonons, Surfaces, and Geometry. *ACS Nano*, 10(1):957–966, January 2016.

[129] Jie Zheng, Caiwei Zhang, and Robert M. Dickson. Highly Fluorescent, Water-Soluble, Size-Tunable Gold Quantum Dots. *Phys. Rev. Lett.*, 93(7):077402, August 2004.

[130] Li Shang, Shaojun Dong, and G. Ulrich Nienhaus. Ultra-small fluorescent metal nanoclusters: Synthesis and biological applications. *Nano Today*, 6(4):401–418, August 2011.

[131] Chen Zhou, Jing Yu, Yanping Qin, and Jie Zheng. Grain size effects in polycrystalline gold nanoparticles. *Nanoscale*, 4(14):4228, 2012.

[132] Hongxing Xu, Javier Aizpurua, Mikael Käll, and Peter Apell. Electromagnetic contributions to single-molecule sensitivity in surface-enhanced Raman scattering. *Phys. Rev. E*, 62(3):4318–4324, September 2000.

[133] Felix Benz, Mikolaj K. Schmidt, Alexander Dreismann, Rohit Chikkaraddy, Yao Zhang, Angela Demetriadou, Cloudy Carnegie, Hamid Ohadi, Bart de Nijs, Ruben Esteban, Javier Aizpurua, and Jeremy J. Baumberg. Single-molecule optomechanics in "picocavities". *Science*, 354(6313):726–729, November 2016.

[134] Hyun-Hang Shin, Gyu Jin Yeon, Han-Kyu Choi, Sang-Min Park, Kang Sup Lee, and Zee Hwan Kim. Frequency-Domain Proof of the Existence of Atomic-Scale SERS Hot-Spots. *Nano Lett.*, 18(1):262–271, January 2018.

[135] Yexin Zhang, Wen Chen, Tong Fu, Jiawei Sun, Daxiao Zhang, Yang Li, Shunping Zhang, and Hongxing Xu. Simultaneous Surface-Enhanced Resonant Raman and Fluorescence Spectroscopy of Monolayer MoSe $_2$: Determination of Ultrafast Decay Rates in Nanometer Dimension. *Nano Lett.*, 19(9):6284–6291, September 2019.

[136] Hongxing Xu, Erik J. Bjerneld, Mikael Käll, and Lars Börjesson. Spectroscopy of Single Hemoglobin Molecules by Surface Enhanced Raman Scattering. *Phys. Rev. Lett.*, 83(21):4357–4360, November 1999.

[137] Jiang, Ken Bosnick, Mathieu Maillard, and Louis Brus. Single Molecule Raman Spectroscopy at the Junctions of Large Ag Nanocrystals. *J. Phys. Chem. B*, 107(37):9964–9972, September 2003.

[138] Nathan C. Lindquist, Carlos Diego L. de Albuquerque, Regivaldo G. Sobral-Filho, Irina Paci, and Alexandre G. Brolo. High-speed imaging of surface-enhanced Raman scattering fluctuations from individual nanoparticles. *Nat. Nanotechnol.*, 14(10):981–987, October 2019.

[139] Cloudy Carnegie, Mattin Urbieta, Rohit Chikkaraddy, Bart de Nijs, Jack Griffiths, William M. Deacon, Marlous Kamp, Nerea Zabala, Javier Aizpurua, and Jeremy J. Baumberg. Flickering nanometre-scale disorder in a crystal lattice tracked by plasmonic flare light emission. *Nat Commun*, 11(1):1–9, February 2020.

[140] Patrick Z. El-Khoury, Dehong Hu, V. Ara Apkarian, and Wayne P. Hess. Raman Scattering at Plasmonic Junctions Shorted by Conductive Molecular Bridges. *Nano Letters*, 13(4):1858–1861, April 2013. Publisher: American Chemical Society.

[141] Emily A. Sprague-Klein, Michael O. McAnally, Dmitry V. Zhdanov, Alyssa B. Zrimsek, Vartkess A. Apkarian, Tamar Seideman, George C. Schatz, and Richard P. Van Duyne. Observation of Single Molecule Plasmon-Driven Electron Transfer in Isotopically Edited 4,4'-Bipyridine Gold Nanosphere Oligomers. *Journal of the American Chemical Society*, 139(42):15212–15221, October 2017. Publisher: American Chemical Society.

[142] Masayoshi Tonouchi. Cutting-edge terahertz technology. *Nature Photonics*, 1(2):97–105, February 2007.

[143] S. Ariyoshi, K. Nakajima, A. Saito, T. Taino, C. Otani, H. Yamada, S. Ohshima, J. Bae, and S. Tanaka. Terahertz response of NbN-based microwave kinetic inductance detectors with rewound spiral resonator. *Superconductor Science and Technology*, 29(3):035012, February 2016.

[144] J. Bueno, O. Yurduseven, S. J. C. Yates, N. Llombart, V. Murugesan, D. J. Thoen, A. M. Baryshev, A. Neto, and J. J. A. Baselmans. Full characterisation of a background limited antenna coupled KID over an octave of bandwidth for THz radiation. *Applied Physics Letters*, 110(23):233503, June 2017.

[145] F. Sizov. Terahertz radiation detectors: the state-of-the-art. *Semiconductor Science and Technology*, 33(12):123001, October 2018.

[146] A. Rogalski, M. Kopytko, and P. Martyniuk. Two-dimensional infrared and terahertz detectors: Outlook and status. *Applied Physics Reviews*, 6(2):021316, June 2019.

[147] Philippe Roelli, Christophe Galland, Nicolas Piro, and Tobias J. Kippenberg. Molecular cavity optomechanics as a theory of plasmon-enhanced Raman scattering. *Nature Nanotechnology*, 11(2):164–169, February 2016.

[148] G. N. Gol'tsman, O. Okunev, G. Chulkova, A. Lipatov, A. Semenov, K. Smirnov, B. Voronov, A. Dzardanov, C. Williams, and Roman Sobolewski. Picosecond superconducting single-photon optical detector. *Applied Physics Letters*, 79(6):705–707, August 2001.

[149] Robert H. Hadfield. Single-photon detectors for optical quantum information applications. *Nature Photonics*, 3(12):696–705, December 2009.

[150] L. Tian and Hailin Wang. Optical wavelength conversion of quantum states with optomechanics. *Physical Review A*, 82(5):053806, November 2010.

[151] Chunhua Dong, Victor Fiore, Mark C. Kuzyk, and Hailin Wang. Optomechanical Dark Mode. *Science*, 338(6114):1609–1613, December 2012.

[152] Jeff T. Hill, Amir H. Safavi-Naeini, Jasper Chan, and Oskar Painter. Coherent optical wavelength conversion via cavity optomechanics. *Nature Communications*, 3:1196, November 2012.

[153] T. A. Palomaki, J. W. Harlow, J. D. Teufel, R. W. Simmonds, and K. W. Lehnert. Coherent state transfer between itinerant microwave fields and a mechanical oscillator. *Nature*, 495(7440):210–214, March 2013.

[154] Joerg Bochmann, Amit Vainsencher, David D. Awschalom, and Andrew N. Cleland. Nanomechanical coupling between microwave and optical photons. *Nature Physics*, 9(11):712–716, November 2013.

[155] R. W. Andrews, R. W. Peterson, T. P. Purdy, K. Cicak, R. W. Simmonds, C. A. Regal, and K. W. Lehnert. Bidirectional and efficient conversion between microwave and optical light. *Nature Physics*, 10(4):321–326, April 2014.

[156] Moritz Forsch, Robert Stockill, Andreas Wallucks, Igor Marinkovic, Claus Gärtner, Richard A. Norte, Frank van Otten, Andrea Fiore, Kartik Srinivasan, and Simon Gröblacher. Microwave-to-optics conversion using a mechanical oscillator in its quantum ground state. *Nature Physics*, 16(1):69–74, January 2020.

[157] Cherif Belacel, Yanko Todorov, Stefano Barbieri, Djamal Gacemi, Ivan Favero, and Carlo Sirtori. Optomechanical terahertz detection with single meta-atom resonator. *Nature Communications*, 8(1):1578, 2017.

Bibliography

[158] R.W. Boyd and D. Prato. *Nonlinear Optics*. Elsevier Science, 2008.

[159] Ketil Karstad, André Stefanov, Mark Wegmuller, Hugo Zbinden, Nicolas Gisin, Thierry Aellen, Mattias Beck, and Jérôme Faist. Detection of mid-IR radiation by sum frequency generation for free space optical communication. *Optics and Lasers in Engineering*, 43(3):537–544, March 2005.

[160] P. Tidemand-Lichtenberg, J. S. Dam, H. V. Andersen, L. Høgstedt, and C. Pedersen. Mid-infrared upconversion spectroscopy. *JOSA B*, 33(11):D28–D35, November 2016.

[161] Yu-Pei Tseng, Christian Pedersen, and Peter Tidemand-Lichtenberg. Upconversion detection of long-wave infrared radiation from a quantum cascade laser. *Optical Materials Express*, 8(5):1313–1321, May 2018.

[162] Lawrence H. Daly Colthup, Stephen E. Wiberley Norman B. *Introduction to Infrared and Raman Spectroscopy: 3rd (Third) edition*. Elsevier Science, September 1990.

[163] Claude Cohen-Tannoudji, Jacques Dupont-Roc, and Gilbert Grynberg. *Atom-photon interactions: basic processes and applications*. J. Wiley, March 1992.

[164] Serge Haroche and Jean-Michel Raimond. *Exploring the Quantum: Atoms, Cavities, and Photons*. Oxford University Press, 1997.

[165] A. Shalabney, J. George, J. Hutchison, G. Pupillo, C. Genet, and T. W. Ebbesen. Coherent coupling of molecular resonators with a microcavity mode. *Nature Communications*, 6:5981, January 2015.

[166] Bernd Metzger, Eric Muller, Jun Nishida, Benjamin Pollard, Mario Hentschel, and Markus B. Raschke. Purcell-enhanced spontaneous emission of molecular vibrations. *Physical Review Letters*, 123(15), October 2019.

[167] Wenqi Zhu and Kenneth B. Crozier. Quantum mechanical limit to plasmonic enhancement as observed by surface-enhanced raman scattering. *Nature Communications*, 5:5228, 2014.

[168] Frank Neubrech, Christian Huck, Ksenia Weber, Annemarie Pucci, and Harald Giessen. Surface-Enhanced Infrared Spectroscopy Using Resonant Nanoantennas. *Chemical Reviews*, 117(7):5110–5145, April 2017.

[169] Frank Schreiber. Structure and growth of self-assembling monolayers. *Progress in Surface Science*, 65(5):151–257, November 2000.

[170] J. Christopher Love, Lara A. Estroff, Jennah K. Kriebel, Ralph G. Nuzzo, and George M. Whitesides. Self-Assembled Monolayers of Thiolates on Metals as a Form of Nanotechnology. *Chemical Reviews*, 105(4):1103–1170, April 2005.

[171] Mingsheng Long, Anyuan Gao, Peng Wang, Hui Xia, Claudia Ott, Chen Pan, Yajun Fu, Erfu Liu, Xiaoshuang Chen, Wei Lu, Tom Nilges, Jianbin Xu, Xiaomu Wang, Weida Hu, and Feng Miao. Room temperature high-detectivity mid-infrared photodetectors based on black arsenic phosphorus. *Science Advances*, 3(6):e1700589, June 2017.

[172] Xiaolong Chen, Xiaobo Lu, Bingchen Deng, Ofer Sinai, Yuchuan Shao, Cheng Li, Shaofan Yuan, Vy Tran, Kenji Watanabe, Takashi Taniguchi, Doron Naveh, Li Yang, and Fengnian Xia. Widely tunable black phosphorus mid-infrared photodetector. *Nature Communications*, 8(1):1–7, November 2017.

[173] Daniel Dregely, Richard Taubert, Jens Dorfmuller, Ralf Vogelgesang, Klaus Kern, and Harald Giessen. 3d optical Yagi–Uda nanoantenna array. *Nature Communications*, 2:267, April 2011.

[174] Sebastian Busschaert, Nikolaus Flöry, Sotirios Papadopoulos, Markus Parzefall, Sebastian Heeg, and Lukas Novotny. Beam Steering with a Nonlinear Optical Phased Array Antenna. *Nano Letters*, 19(9):6097–6103, September 2019.

[175] Constantine A. Balanis. *Antenna Theory: Analysis and Design.* Wiley-Interscience, 2005.

[176] Benedikt Schwarz, Peter Reininger, Daniela Ristanic, Hermann Detz, Aaron Maxwell Andrews, Werner Schrenk, and Gottfried Strasser. Monolithically integrated mid-infrared lab-on-a-chip using plasmonics and quantum cascade structures. *Nature Communications*, 5:4085, 2014.

[177] Hongtao Lin, Zhengqian Luo, Tian Gu, Lionel C. Kimerling, Kazumi Wada, Anu Agarwal, and Juejun Hu. Mid-infrared integrated photonics on silicon: a perspective. *Nanophotonics*, 7(2):393–420, 2018.

[178] Andreas Tittl, Aleksandrs Leitis, Mingkai Liu, Filiz Yesilkoy, Duk-Yong Choi, Dragomir N. Neshev, Yuri S. Kivshar, and Hatice Altug. Imaging-based molecular barcoding with pixelated dielectric metasurfaces. *Science*, 360(6393):1105–1109, 2018.

[179] Filiz Yesilkoy, Eduardo R. Arvelo, Yasaman Jahani, Mingkai Liu, Andreas Tittl, Volkan Cevher, Yuri Kivshar, and Hatice Altug. Ultrasensitive hyperspectral imaging and biodetection enabled by dielectric metasurfaces. *Nature Photonics*, page 1, 2019.

[180] Gelon Albrecht, Stefan Kaiser, Harald Giessen, and Mario Hentschel. Refractory plasmonics without refractory materials. *Nano Letters*, 17(10):6402–6408, 2017. PMID: 28853899.

[181] Philip M. Morse. Diatomic molecules according to the wave mechanics. ii. vibrational levels. *Phys. Rev.*, 34:57–64, Jul 1929.

[182] Vincenzo Barone. Anharmonic vibrational properties by a fully automated second-order perturbative approach. *The Journal of Chemical Physics*, 122(1), 2005.

Bibliography

[183] Lukas Novotny and Bert Hecht. *Principles of Nano-Optics.* Cambridge University Press, September 2012.

[184] Jiří Homola and Marek Piliarik. Surface Plasmon Resonance (SPR) Sensors. In Jiří Homola, editor, *Surface Plasmon Resonance Based Sensors*, volume 4, pages 45–67. Springer Berlin Heidelberg, Berlin, Heidelberg, 2006.

[185] Kevin T. Crampton, Alexander Fast, Eric O. Potma, and V. Ara Apkarian. Junction Plasmon Driven Population Inversion of Molecular Vibrations: A Picosecond Surface-Enhanced Raman Spectroscopy Study. *Nano Letters*, 18(9):5791–5796, September 2018.

[186] Jacek Szczerbiński, Luzia Gyr, Jérôme Kaeslin, and Renato Zenobi. Plasmon-Driven Photocatalysis Leads to Products Known from E-beam and X-ray-Induced Surface Chemistry. *Nano Letters*, October 2018.

[187] Nicki Hogan, Shengxiang Wu, and Matthew Sheldon. Hot Electron Dynamics in Plasmonic Thermionic Emitters. *arXiv:1905.01580 [cond-mat, physics:physics]*, May 2019. arXiv: 1905.01580.

CONTACT INFORMATION	Master of Science in Physics EPFL SB IPHYS LPQM1 PH D3 305 (Bâtiment PH) CH-1015 Lausanne

Mobile : +41795047010
E-mail : philippe.roelli@epfl.ch

<small>EDUCATION</small>

Swiss Federal Institute of Technology Lausanne (EPFL) & Max-Planck-EPFL Center for Molecular Nanoscience and Technology (CMNT)

Ph.D., Physics,   **2014 to present**
- Laboratory of Photonics and Quantum Measurements
- Adviser : Professor Tobias Kippenberg
- Co-adviser : Professor Christophe Galland
- Area of Study : Photonics, Nanotechnology

Swiss Federal Institute of Technology Lausanne (EPFL)

M.S., Physics,   **2011-2014**
- Master project : An optomechanical approach to the surface enhanced Raman scattering processes
- Adviser : Professor Tobias Kippenberg
- Area of Study : Condensed matter, Photonics

- Theoretical second semester project : Quantum Phase Transition
- Adviser : Professor Frédéric Mila
- Area of Study : Condensed matter theory

- Third semester at the ETHZ Department of Physics
- Fourth semester : Military service in the nuclear protection laboratory in Spiez

B.S., Physics,   **2008-2011**
- Third year exchange at the UGR Department of Physics (Spain)

Juelich Forschungszentrum

Guest Student Programme, Biophysics,   **Summer 2012**
- Project : Collective behaviour of active bodies
- Adviser : Professor Gerhard Gompper
- Area of Study : Theoretical Soft Matter

<small>TEACHING EXPERIENCE</small>

Swiss Federal Institute of Technology Lausanne (EPFL)

Teaching Assistant   **2011-2012**
- Physics I for microengineers
 (Professor Grandjean)
- Physics II for microengineers
 (Professor Grandjean)
- Biothermodynamics for life scientists
 (Professor De Los Rios)

Head Assistant   **2015 to 2019**
- General Physics II - Electromagnetism
 (Professor Kippenberg)

<small>JOURNAL PUBLICATIONS</small>

1. P. Roelli, C. Galland, N. Piro & T. J. Kippenberg, "Molecular cavity optomechanics as a theory of plasmon-enhanced Raman scattering", Nature Nanotechnology **11**, 164-169 (2016). (**With accompanying News & Views**)

2. P. Roelli, D. Martin-Cano, T. J. Kippenberg & C. Galland, "Molecular platform for frequency upconversion at the single-photon level", *manuscript in review at PRX*

3. W. Chen, P. Roelli, A. Ahmed, S. Verlekar, H. Hu, G. Tagliabue, T. J. Kippenberg & C. Galland, "Intrinsic Luminescence Blinking from Plasmonic Nanojunctions", *manuscript in preparation*

TALKS AT CONFERENCES

Contributed Talks
- NANOMETA, Seefeld 2015.
- ITN workshop, Diavolezza 2015.
- Congrs gnral de la SFP, Strasbourg 2015.
- CLEO/Europe, Munich 2015.
- META conference, New York 2015.
- MRS Fall Meeting, Boston 2015.
- MPG-EPFL Science Day, EPFL 2015.
- Journes de la Matire Condense, Bordeaux 2016.
- GRS Plasmonics & Nanophotonics, Sunday River 2016.
- MPG-EPFL Science Day, Stuttgart 2016.
- ICMAT Nano-Optics and Photonics Symposium, Singapore 2017.
- ICORS, Jeju 2018.
- THOR meeting, San Sebastian 2019.
- S3IC conference *accepted*, Barcelona 2020.

Poster Presentations
- Frontiers in Nanophotonics, Monte Verita 2015. (**Young scientist award**)
- Symposium "20 Years Nano-Optics", Erlangen 2017.
- OMT conference, Saanen 2018.
- OMT conference, Saanen 2019.
- Quantum Nanophotonics, Benasque 2019. (**Poster award**)
- OMT conference, Saanen 2020.

PROFESSIONAL EXPERIENCE

Lloyds Bank, Geneva, Switzerland
- Trainee at the Account Opening office   **Summer 2008**
- Trainee in the Alternative Investments unit   **Summer 2009**

OTHER ACTIVITIES

Work in Musical Event   **2013 to 2019**
Manager of the financial management office during the Montreux Jazz Festival

ESS Ski Instructor   **2008 to present**
Trainer of the ski club Nyon competition team

Activity in EPFL associations   **2016 to present**
Founder of the EPS Young Minds section
Founder of the Polyphys Association
Organizer of the Physics Day at EPFL

LANGUAGES

French (Native), English (Fluent), German (Basic), Spanish (Basic)

REFERENCES AVAILABLE TO CONTACT

Professor De Los Rios
- Associate Professor, Laboratory of Statistical Biophysics, EPFL

Professor Tobias Kippenberg
- Full Professor, Laboratory of Photonics and Quantum Measurements, EPFL

Professor Christophe Galland
- SNSF-funded Professor, Laboratory of Quantum Nano-optics, EPFL